



Title	Development of a Sustainable Process Based on Carrier-microencapsulation to Suppress the Formation of Arsenic-containing Acid Mine Drainage from Arsenopyrite
Author(s)	Park, Ilhwan
Citation	北海道大学. 博士(工学) 甲第13660号
Issue Date	2019-03-25
DOI	10.14943/doctoral.k13660
Doc URL	http://hdl.handle.net/2115/77003
Type	theses (doctoral)
File Information	Ilhwan_Park.pdf



[Instructions for use](#)

**Development of a Sustainable Process Based on
Carrier-microencapsulation to Suppress the Formation
of Arsenic-containing Acid Mine Drainage from
Arsenopyrite**

A dissertation submitted in partial fulfillment of the requirements
for the degree of Doctorate in Engineering

by

ILHWAN PARK



Division of Sustainable Resources Engineering,
Graduate School of Engineering,
Hokkaido University, Japan
March 2019

Abstract

Acid mine drainage (AMD), an acidic leachate contaminated with toxic and hazardous heavy metals, is formed by the oxidation of sulfide minerals in tailing dams of metal and coal mines when exposed to air and water, and it is one of the most serious environmental problems associated with the mining industries. When arsenopyrite (FeAsS), the primary arsenic (As)-bearing sulfide mineral in mineralized zones, is contained in the tailings, its oxidation together with pyrite (FeS₂) generates As-containing AMD. Arsenic is a highly toxic and strictly regulated element known to increase the risks of developing numerous diseases like hyperpigmentation, keratosis, anemia, neuropathy, and several types of cancers even at minute amounts. Because of this, the development of methods to suppress arsenopyrite oxidation is important. Carrier-microencapsulation (CME) has been proposed as a new technique to suppress AMD formation by forming a protective coating on sulfide minerals using metal-catecholate complexes. In this study, the applicability of CME to arsenopyrite was investigated to suppress the formation of As-containing AMD.

Chapter 1 describes the statement of the problem, objectives of this study, background and a literature review of the formation of AMD and its control.

In Chapter 2, the effects of CME using Ti-catecholate complex (Ti-based CME) on arsenopyrite oxidation were investigated by leaching and electrochemical experiments. The results of leaching experiments showed that the release of As from arsenopyrite was substantially suppressed by Ti-based CME, and SEM-EDX and DRIFT analyses of CME-treated residue indicated that arsenopyrite was covered with a Ti-oxyhydroxide coating. The results of cyclic voltammetry and SEM-EDX analysis of a platinum electrode in Ti-catecholate complex solution showed that [Ti(cat)₃]²⁻ was oxidized to form an intermediate phase at 680 mV vs. SHE via partial oxidation of either one or two of the catechol molecules with distorted Ti–O bonds. This was then followed by the chemical decomposition of the intermediate finally releasing Ti⁴⁺ that is precipitated as Ti-oxyhydroxide coating. Chronoamperometric measurements using an arsenopyrite electrode treated with Ti-catecholate complex confirmed that the coating formed by Ti-catecholate complex suppressed both anodic and cathodic half-cell reactions of arsenopyrite oxidation.

In Chapter 3, the kinetic aspects of Ti-based CME for suppressing arsenopyrite oxidation were investigated. Ti-based CME could successfully suppress arsenopyrite oxidation by forming a surface protective coating, but it required at least 14 days of treatment to generate a coating thick enough to be effective under ambient conditions. To improve the kinetics of Ti-based CME, elevated temperature and the addition of chemical promoters like Cu²⁺ or Cu²⁺-NH₃ complex were examined. As temperature increased, the decomposition rate of Ti-catecholate complex became faster, resulting

in the suppression of arsenopyrite oxidation achieved early. The results of Ti-catecholate complex decomposition fitted well with a pseudo first-order kinetic model. The rate constants of complex decompositions at 30, 50, and 70 °C were estimated at around 0.009, 0.021, and 0.051 h⁻¹, respectively, and its activation energy was calculated to be 37.4 kJ/mol. As another option to accelerate the decomposition of Ti-catecholate complex under ambient conditions, the effects of Cu²⁺ addition on Ti-based CME treatment for arsenopyrite were investigated. Instead of dissolved oxygen, Cu²⁺ and Cu²⁺-NH₃ complex acted as an oxidant and enhanced the decomposition of Ti-catechol complex, causing faster precipitation of Ti⁴⁺ and stronger suppressive effects on arsenopyrite oxidation.

In Chapter 4, Al³⁺-catechol complex was evaluated as a candidate of the metal-organic complex used for CME to suppress arsenopyrite oxidation. Al³⁺ and catechol formed three complex species depending on the pH: (1) [Al(cat)]⁺ between 4.7 and 5.5, (2) [Al(cat)₂]⁻ between 5.5 and 8.5, and (3) [Al(cat)₃]³⁻ between 8.5 and 14.0. Electrochemical study confirmed that the decomposition of Al-catecholate complexes occurs sequentially: [Al(cat)₃]³⁻ → [Al(cat)₂]⁻ → [Al(cat)]⁺ → Al³⁺. Leaching experiments and surface characterizations of the residue by SEM-EDX, DRIFT, and XPS showed that in the presence of Al-catecholate complexes, arsenopyrite was covered with an Al-oxyhydroxide coating and As release from arsenopyrite was suppressed. The decomposition rate of Al-catecholate complex was faster than that of Ti-catecholate complex, and the suppression of As release from arsenopyrite was substantial with Al-based CME. The electrical charge of Al³⁺ is smaller than that of Ti⁴⁺, and thus this may cause the weaker bond and faster decomposition rate with Al-catecholate complex than Ti-catecholate complex. Among the three Al-catecholate complexes, [Al(cat)]⁺ suppressed As release most effectively because it had the fastest complex decomposition/coating formation rate. Chronoamperometric measurements of arsenopyrite electrode treated with [Al(cat)]⁺ indicated that both anodic and cathodic half-cell reactions of arsenopyrite oxidation were suppressed by the surface protective coating formed on it. Long-term stability of CME-treated arsenopyrite was evaluated using weathering cell tests for ca. two months and the results showed that arsenopyrite oxidation was successfully suppressed by treating it with Al-based CME.

Chapter 5 summarized the most important findings of this dissertation and proposed a possible application of CME to simultaneously suppress the release of arsenic from arsenopyrite and the formation of AMD.

Table of Contents

List of Figures.....	vi
List of Tables	xi
CHAPTER 1 – GENERAL INTRODUCTION	1
1.1 Statement of the problem and objectives of this study	1
1.2 Literature review on acid mine drainage.....	2
<i>1.2.1 Acid mine drainage formation and its nature of the problem.....</i>	<i>2</i>
<i>1.2.2 Remediation techniques</i>	<i>3</i>
<i>1.2.3 Prevention techniques.....</i>	<i>12</i>
1.3 Outline of the dissertation.....	24
References.....	24
CHAPTER 2 – SUPPRESSION OF THE RELEASE OF ARSENIC FROM ARSENOPYRITE BY CARRIER-MICROENCAPSULATION USING TITANIUM-CATECHOLATE COMPLEX.....	37
2.1 Introduction	37
2.2 Materials and methods	38
<i>2.2.1 Synthesis of Ti-catecholate complex.....</i>	<i>38</i>
<i>2.2.2 Ti-catecholate complex formation with various stoichiometric molar ratios of Ti⁴⁺ to catechol.....</i>	<i>38</i>
<i>2.2.3 Identification of Ti-catecholate complex stability</i>	<i>38</i>
<i>2.2.4 Ultraviolet-visible light spectrophotometric measurements</i>	<i>39</i>
<i>2.2.5 Electrochemical studies for the insights into Ti-catecholate complex decomposition</i>	<i>39</i>
<i>2.2.6 Characterization of arsenopyrite sample</i>	<i>40</i>
<i>2.2.7 Batch leaching experiments.....</i>	<i>41</i>

2.2.8 Chronoamperometry to identify the suppressive effects of coatings on arsenopyrite oxidation	42
2.3 Results and discussion	42
2.3.1 Evaluation and characterization of Ti-catecholate complex	42
2.3.2 Mechanism of Ti-catecholate complex decomposition and coating formation.....	44
2.3.3 Ti-based CME to suppress the release of As from arsenopyrite.....	49
2.3.4 Anodic and cathodic half-cell reactions of arsenopyrite oxidation.....	54
2.3.5 The proposed mechanism of Ti-based CME.....	55
2.4 Conclusions.....	56
References.....	57

CHAPTER 3 – IMPROVEMENTS IN THE KINETICS OF TITANIUM-BASED CARRIER-MICROENCAPSULATION.....	61
3.1 Introduction	61
3.2 Materials and methods.....	62
3.2.1 Materials.....	62
3.2.2 Effects of temperature and Cu^{2+} - NH_3 complex on Ti-based CME	62
3.2.3 Interaction of Cu^{2+} with Ti-catechol complex and/or arsenopyrite.....	63
3.3 Results and discussion	64
3.3.1 Effects of temperature.....	64
3.3.2 Effects of Cu^{2+} - NH_3 complex.....	68
3.3.3 Effects of Cu^{2+}	69
3.4 Conclusions.....	73
References.....	73

CHAPTER 4 – A NEW COMPLEX-BASED CARRIER-MICROENCAPSULATION: THE DECOMPOSITION MECHANISM OF ALUMINUM-CATECHOLATE COMPLEX, AND ITS APPLICATION TO SUPPRESS ARSENOPYRITE OXIDATION	75
--	-----------

4.1 Introduction	75
4.2 Materials and methods	76
4.2.1 <i>Characterization of arsenopyrite</i>	76
4.2.2 <i>Synthesis of Al-catecholate complexes</i>	76
4.2.3 <i>Ultraviolet-visible light spectrophotometric measurements</i>	76
4.2.4 <i>Electrochemical studies</i>	77
4.2.5 <i>Batch leaching experiments</i>	77
4.2.6 <i>Acidic oxalate extraction</i>	78
4.2.7 <i>Chronoamperometry</i>	78
4.2.8 <i>Weathering cell test</i>	78
4.2.9 <i>Regeneration of used organic carrier</i>	79
4.3 Results and discussion	80
4.3.1 <i>Speciation of Al-catecholate complexes with pH</i>	80
4.3.2 <i>Electrochemical properties of Al-catecholate complexes</i>	83
4.3.3 <i>Al-based CME to suppress the oxidations of pyrite and arsenopyrite</i>	85
4.3.4 <i>Anodic and cathodic half-cell reactions of arsenopyrite oxidation</i>	93
4.3.5 <i>The proposed mechanism of Al-based CME</i>	94
4.3.6 <i>Long-term stability of CME-treated arsenopyrite</i>	95
4.3.7 <i>Regeneration of used organic carrier by electrolysis</i>	97
4.4 Conclusions	98
References	99
CHAPTER 5 – GENERAL CONCLUSION	103
ACKNOWLEDGEMENT	106

List of Figures

Figure 1-1	The schematic diagrams of anoxic and oxic limestone drains (ALD/OLD).	7
Figure 1-2	The solubility diagram of metal hydroxides as a function of pH.	8
Figure 1-3	The schematic diagram of anaerobic wetland.	8
Figure 1-4	The solubility diagram of metal sulfides as a function of pH ($[H_2S] = 1 \text{ M}$).	9
Figure 1-5	Eh-pH predominance diagram of Mn^{2+} - H_2O system at 25 °C, 1.013 bar, and activity of $Mn^{2+} = 10^{-3}$ (Bethke, 1992; Gustafsson, 2010).	10
Figure 1-6	The schematic diagram of high density sludge (HDS) process.	11
Figure 1-7	The schematic diagrams of (a) cover with capillary barrier effect and (b) impoundment.	13
Figure 1-8	The schematic diagram of sub-aqueous disposal.	14
Figure 1-9	The schematic diagram of blending of mine wastes with neutralizing materials.	17
Figure 1-10	The schematic diagram of the formation of ferric phosphate coating on pyrite, and Log activity–pH predominance diagram of Fe^{3+} at 25 °C and 1.013 bar in the presence of PO_4^{3-} ($a = 1.0$) created using the Geochemist’s Workbench®.	20
Figure 1-11	The schematic diagram of carrier-microencapsulation using Ti-catecholate complex.	23
Figure 2-1.	The schematic diagram of the setup for electrochemical studies.	40
Figure 2-2.	Mineralogical composition of the arsenopyrite sample.	41
Figure 2-3.	Properties of synthesized Ti-catecholate complex: (a) Ti^{4+} ion stability with pH in the presence and absence of catechol, (b) Log a – pH predominance diagram of $Ti(OH)_4$ at 25 °C and 1.013 bar created using the Geochemist’s Workbench® with MINTEQ database (Bethke, 1992; Gustafsson, 2010), (c) Ti^{4+} ion stability as a function of molar ratio of catechol to Ti^{4+} , (d) UV-vis spectra of “free” catechol and Ti-catechol solutions at pH 1, 3, 6 and 9.	44
Figure 2-4.	Cyclic voltammograms of (a) catechol only and Ti-catechol solution at a scan rate of 5 mV/s, (a-1) catechol at pH 5, (a-2) catechol at pH 9, (a-3) Ti-catechol at pH 9, and (b) Ti-catechol solution at pH 9 with various scan rates (1 mV/s (b-1), 5 mV/s (b-2), and 30 mV/s (b-3)). Note that arrows	46

	denote the sweep direction.	
Figure 2-5.	SEM-EDX analysis of Pt electrode after chronoamperometry at 1.0 V vs. SHE for 3h: (a-1) SEM photomicrograph and (a-2) energy dispersive X-ray spectra of several points, (b-1) SEM photomicrograph and the corresponding elemental maps of Pt (b-2), C (b-3), Ti (b-4), and O (b-5).	47
Figure 2-6.	SEM-EDX analysis of Pt electrode after immersion in Ti-catechol solution for 3h: (a) SEM photomicrograph and (b) energy dispersive X-ray spectra of several points.	47
Figure 2-7.	Molecular structure of Ti(IV) tris-catecholate complex.	48
Figure 2-8.	The schematic diagram of the anodic decomposition of Ti-catecholate complex.	49
Figure 2-9.	Leaching of arsenopyrite in DI water (control), catechol only, Ti-catecholate complex (CME): evolution of (a) pH and (b) Eh, and changes in the concentrations of (c) As and (d) Ti with time.	52
Figure 2-10.	SEM-EDX analysis of arsenopyrite after Ti-based CME treatment: (a) SEM photomicrograph, elemental maps of (b) Fe, (c) As, (d) S, (e) Ti and (f) O, and (g) energy dispersive X-ray spectrum of scanned area.	53
Figure 2-11.	DRIFT spectra of arsenopyrite before and after 25 days of leaching experiments: (a) spectra of washed arsenopyrite and residues leached in DI water (control), catechol only and Ti-catechol solution (CME), and (b) deconvoluted spectrum of CME-treated arsenopyrite. Note that the scale of (a) and (b) are 0.05 and 0.005, respectively.	54
Figure 2-12.	Chronoamperometric response of arsenopyrite pretreated with DI water (control) and Ti-catecholate complex (CME): (a) anodic polarization at +0.8 V vs. SHE, and (b) cathodic polarization at 0.0 V vs. SHE. Note that y-axes of Figures 3-5a and b are “Current density” and “-Current density,” respectively.	55
Figure 2-13.	The schematic diagram of a proposed mechanism of Ti-based CME.	56
Figure 3-1.	The schematic diagram of the catalytic effect of $\text{Cu}^{2+}\text{-NH}_3$ complex in Ti-based CME and Eh-pH diagram of $\text{Cu}^{2+}\text{-NH}_3\text{-H}_2\text{O}$ system at 25 °C calculated by assuming that the activity of Cu is 0.5 and the total concentration of ammonia is $7.0 \text{ kmol}\cdot\text{m}^{-3}$ (Koyama et al., 2006).	61

Figure 3-2.	The schematic diagram of the reactor-type leaching apparatus.	63
Figure 3-3.	Leaching of arsenopyrite in Ti-catechol solution under various temperature: changes in the concentrations of (a) As and (b) Ti with time.	64
Figure 3-4.	Linear pseudo-first-order kinetic model for Ti^{4+} precipitation at various temperatures.	66
Figure 3-5.	The parity plots comparing experimental and calculated data of Ti^{4+} concentration at (a) 30 °C, (b) 50 °C, and (c) 70 °C.	67
Figure 3-6.	Arrhenius plot between $\ln k$ and T^{-1} .	67
Figure 3-7.	Leaching of arsenopyrite in Ti-catechol solution with and without Cu^{2+} - NH_3 complex: changes in the concentrations of (a) As, (b) Ti, and (c) Cu with time.	68
Figure 3-8.	Stability of Ti-catecholate complex in the absence and presence of Cu^{2+} - NH_3 complex: changes in the concentrations of (a) Ti and (b) Cu with time.	69
Figure 3-9.	Leaching of arsenopyrite in Ti-catechol solution with and without Cu^{2+} : changes in the concentrations of (a) As and (b) Ti & Cu with time.	70
Figure 3-10.	Stability of Ti-catecholate complex with varying the concentration of Cu^{2+} added.	71
Figure 3-11	Interaction between Cu^{2+} and arsenopyrite.	71
Figure 3-12	Log activity–pH predominance diagram of Cu^{2+} - H_2O system at 25 °C and 1.013 bar created using the Geochemist’s Workbench with the MINTEQ database (Bethke, 1992; Gustafsson, 2010).	72
Figure 3-13	SEM-EDX results of arsenopyrite treated with the solution containing Cu^{2+} for 1 day.	72
Figure 4-1.	The schematic diagram of the setup for weathering cell tests.	79
Figure 4-2.	Characterization of Al-catecholate complexes: speciation diagram of (a) Al^{3+} only ($[Al^{3+}]$: 1 mM) and (b) Al^{3+} -catechol system ($[Al^{3+}]$: 1 mM, $[H_2Cat]$: 3 mM) (Nurchi et al., 2009), (c) solubility of Al^{3+} with pH in the absence and presence of catechol, and (d) UV-vis spectra of catechol only and Al-catechol solution at pH 5, 7 and 10.	81
Figure 4-3.	Log activity–pH predominance diagram of Al^{3+} at 25 °C and 1.013 bar created using the Geochemist’s Workbench [®] with MINTEQ database (Bethke, 1992; Gustafsson, 2010).	81

- Figure 4-4. Characterization of Al-catecholate complexes: UV-vis spectra of catechol solutions with varying Al^{3+} molar ratio (0.0 to 2.3) at pH 5 (a), at pH 7 (b) and at pH 10 (c), and Al concentration as a function of molar ratio of $[\text{H}_2\text{cat}]/[\text{Al}^{3+}]$ at pH 5 (d), at pH 7 (e) and at pH 10 (f). Note that the insets in Figures 4-4a–c are plots of maximum absorbance vs. $[\text{Al}^{3+}]/[\text{H}_2\text{cat}]$ molar ratio. 82
- Figure 4-5. (a) Cyclic voltammograms of Al-catechol solutions at pH 5, 7 and 10, and first anodic sweeps of (b) Al-catecholate complexes and (c) catechol at pH 5, 7 and 10. Note that arrows denote the sweep direction. 84
- Figure 4-6. Effects of Al-catecholate complexes on the oxidation of arsenopyrite: evolution of (a) pH and (b) Eh, and changes in (c) dissolved Fe, As and S concentrations, (d) dissolved Al concentration. Note: $[\text{Al}^{3+}] = 5 \text{ mM}$; $[\text{H}_2\text{Cat}] = 15 \text{ mM}$; $[\text{Cl}^-]_{\text{tot}} = 15 \text{ mM}$; leaching time = 7 days; pH = 5, 7 and 10 for $[\text{Al}(\text{cat})]^+$, $[\text{Al}(\text{cat})_2]^-$ and $[\text{Al}(\text{cat})_3]^{3-}$, respectively. 85
- Figure 4-7. Effects of time on the oxidation of arsenopyrite: evolution of leachate (a) pH and (b) Eh, and changes in the concentrations of (c) Fe, (d) As, (e) S and (f) Al. Note: Control, Al only ($[\text{Al}^{3+}] = 5 \text{ mM}$), Catechol ($[\text{H}_2\text{Cat}] = 5 \text{ mM}$), $[\text{Al}(\text{cat})]^+$ ($[\text{Al}^{3+}] = 5 \text{ mM}$ and $[\text{H}_2\text{Cat}] = 5 \text{ mM}$); $[\text{Cl}^-]_{\text{tot}} = 15 \text{ mM}$; pH = 5. 88
- Figure 4-8. SEM-EDX analysis of precipitates from the leaching of arsenopyrite in Al^{3+} only solution for 10 day: (a) SEM photomicrograph, elemental maps of (b) Fe, (c) As, (d) Al and (e) O, and (f) energy dispersive X-ray spectrum of the scanned area. 89
- Figure 4-9. Log activity-pH predominance diagram of AsO_4^{3-} at 25 °C and 1.013 bar in the presence of Fe^{3+} ($a = 10^{-2.7}$), Al^{3+} ($a = 10^{-3.0}$) and SO_4^{2-} ($a = 10^{-2.5}$) created using the Geochemist's Workbench® with MINTEQA2 database (Bethke, 1992; Gustafsson, 2010). 89
- Figure 4-10. Characterization of arsenopyrite after treatment in $[\text{Al}(\text{cat})]^+$ solution for 10 day: (a) SEM photomicrograph, elemental maps of (b) Fe, (c) As, (d) S and (e) Al, (f) energy dispersive X-ray spectrum of the scanned area. 90
- Figure 4-11. DRIFT spectra of arsenopyrite before and after leaching. 90
- Figure 4-12. XPS spectra of arsenopyrite treated with control and CME for (a) Al 2p and (b) O 1s. 92
- Figure 4-13. Effects of $[\text{Al}(\text{cat})]^+$ concentrations on the oxidation of arsenopyrite: (a) pH, (b) dissolved Fe, As, and S concentrations leached from arsenopyrite, (c) 93

dissolved Al concentration before and after leaching of arsenopyrite, and (d) the amounts of extracted Al from the coating formed on arsenopyrite. Note: ratio of Al^{3+} to catechol = 1:1; $[\text{Cl}^-]_{\text{tot}} = 45 \text{ mM}$; leaching time = 7 days; pH = 5.

Figure 4-14.	Chronoamperometric response of arsenopyrite pretreated with DI water (control) and Al-catecholate complex (CME): (a) anodic polarization of arsenopyrite at +0.7 V vs. SHE and (b) cathodic polarization of arsenopyrite at 0.0 V vs. SHE. Note that y-axes of Figure 4-14b is “–Current density.”	94
Figure 4-15.	The schematic diagram of a proposed mechanism of Al-based CME.	95
Figure 4-16.	Weathering cell tests of control and CME-treated arsenopyrite: changes in the concentrations of (a) Fe, (b) As, and (c) S, and evolution of leachate (d) pH.	96
Figure 4-17.	SEM-EDX results of residues after weathering cell tests: (a) SEM photomicrograph and (b) EDX spectrum of control, and (c) SEM photomicrograph and (d) EDX spectrum of CME-treated sample.	96
Figure 4-18.	(a) Linear sweep voltammograms and (b) UV-vis spectra of catechol solutions with various air-exposure times.	97
Figure 4-19.	Linear sweep voltammograms of non-treated and pre-oxidized catechol solutions, and regenerated catechol solution using electrolysis.	98
Figure 5-1	The proposed process based on CME for treating mine wastes.	105

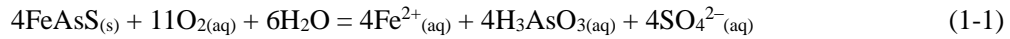
List of Tables

Table 1-1	A list of the number of abandoned/closed mines around the world and the geochemical characteristics of acid mine drainages (AMDs) generated from some representative mines in these countries.	4
Table 1-2	Broad guideline for determining the suitability of passive treatment system based on influent water characteristics (Taylor et al., 2005).	6
Table 1-3	Broad guideline for determining the suitability of active treatment system based on influent water characteristics (Taylor et al., 2005).	10
Table 1-4	Chemical properties and costs associated with some AMD neutralization materials (Taylor et al., 2005).	11
Table 2-1.	Chemical composition of the arsenopyrite sample.	41
Table 2-2.	Electric charges generated during anodic and cathodic polarizations of arsenopyrite pretreated in DI water (control) and Ti-catecholate complex (CME).	55
Table 3-1.	Values of apparent rate constant (k) and correlation coefficient (R^2) obtained from pseudo-first-order kinetic model shown in Figure 3-4.	66
Table 4-1.	Assignments of absorption peaks in DRIFTS spectra of untreated arsenopyrite, and those leached in DI water, catechol and $[Al(cat)]^+$ for 10 days.	91
Table 4-2.	Electric charges generated during anodic and cathodic polarizations of arsenopyrite pretreated in DI water (control) and Al-catecholate complex (CME).	94

CHAPTER 1 – GENERAL INTRODUCTION

1.1 Statement of the problem and objectives of this study

Arsenopyrite (FeAsS), the most common primary arsenic (As)-bearing sulfide mineral in nature, plays an important role in the release of As into the environment. When exposed to atmospheric conditions either naturally or via anthropogenic activities like mining, mineral processing, metallurgy, and underground space developments, it is readily oxidized by oxygen (O₂) and/or ferric ion (Fe³⁺) in the presence of water as illustrated by the following equations:



Arsenic is a strictly regulated substance because of its potential to cause numerous diseases like hyperpigmentation, keratosis, anemia, neuropathy, and several types of cancers even at minute amounts (Boddu et al., 2008; Mohan and Pittman, 2007). Moreover, the oxidation of arsenopyrite generates acid mine drainage (AMD), a serious environmental problem encountered by the mining and mineral processing industries throughout the world because of its extremely low pH (less than pH 3) and elevated concentrations of hazardous heavy metals (e.g., cadmium (Cd), copper (Cu), iron (Fe), manganese (Mn), lead (Pb), and zinc (Zn)) (Johnson and Hallberg, 2005).

To mitigate these problems caused by arsenopyrite, this study investigated carrier-microencapsulation (CME), a process that suppresses arsenopyrite oxidation by forming surface protective coatings on the mineral. This technique uses a redox-sensitive organic compound to carry and deliver the coating material, usually an insoluble metal(loid) ion, preferentially to the surface of sulfide mineral where it is adsorbed and oxidatively decomposed. As a consequence of the complex decomposition, the relatively insoluble metal ion is freed, thus rapidly precipitating and forming a protective coating on the mineral surface. The primary advantage of this technique compared with other microencapsulation techniques is its ability to specifically target sulfide minerals even in complex systems because the oxidative decomposition of the complex occurs only on the surfaces of minerals that dissolve electrochemically like most of the sulfide minerals (Crundwell, 1988; Rimstidt and Vaughan, 2003).

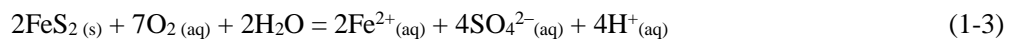
The original CME study of Satur et al. (2007) used Ti-catecholate complex (i.e., [Ti(cat)₃]²⁻) that could suppress the oxidation of pyrite by forming Ti-oxyhydroxide coating on it. However, the mechanisms involved in this process remain unclear due to the lack of understanding of how the Ti-catecholate complex is oxidatively decomposed. Moreover, the applicability of CME for

arsenopyrite has not yet been studied. Thus, the objectives of this study are four-fold: (1) to elucidate the mechanisms involved in Ti-based CME in detail, (2) to apply Ti-based CME to arsenopyrite, (3) to improve the practicality of CME, and (4) to develop a sustainable process based on CME to prevent the formation of As-containing AMD from arsenopyrite.

1.2 Literature review on acid mine drainage

1.2.1 Acid mine drainage formation and its nature of the problem

Mineral resources have, for thousands of years, been exploited to obtain valuable metals for our lives as well as many industries. To produce metals, it requires a series of processes: (1) mining ores from the Earth's crust, (2) mineral processing that separates valuable minerals (i.e., concentrates) from non-valuable minerals (i.e., tailings), and (3) metallurgy that extracts and produces the metals from concentrates. As a consequence, however, large amounts of mine wastes like waste rocks, spoils and tailings are unnecessarily generated and these wastes pose serious threats to the environment because of the formation of acid leachate called acid mine drainage (AMD), also referred to as acid rock drainage (ARD), when exposed to atmospheric conditions (Johnson, 2003). Moreover, this problem also occurs in both open-pit and underground mines after closed. During the life of a mine, water that enters the working areas is pumped out for mining activities but when mines are closed, this pumping system is generally stopped and thus the level of the groundwater or subsurface water table rebounds to its natural level, which forms a pit lake (Johnson, 2003). AMD is not only acidic but also contains high levels of dissolved metal(loid)s and sulfate anions (Zhao et al., 2009). As summarized in Table 1-1, there are a lot of abandoned mines throughout the world that have been producing AMD. Sulfide minerals are the primary reactive components of mine wastes and their oxidations lead to the production, rather than the consumption, of protons unlike most geochemical weathering processes (Johnson, 2003; Banks et al., 1997). Among the sulfides, pyrite (FeS_2) is considered as the main culprit of AMD formation because it is the most common and widespread sulfide mineral in nature (Evangelou, 1995). Pyrite is relatively stable but in the presence of oxidants like oxygen (O_2) and ferric ion (Fe^{3+}), it readily oxidized as illustrated by the following reactions:



Pyrite is initially oxidized by O_2 and releases ferrous ions (Fe^{2+}), sulfate anions (SO_4^{2-}) and protons (H^+) (Eq. (1-3)). Under oxidizing conditions, Fe^{2+} can be further oxidized to Fe^{3+} (Eq. (1-4)), which is either precipitated as ferric hydroxide ($Fe(OH)_3$) that is a yellow-orange precipitate referred to as “yellow boy” (Eq. (1-5)) or consumed to dissolve pyrite (Eq. (1-6)). The oxidation of Fe^{2+} to Fe^{3+} by O_2 (Eq. (1-5)) is known to progress slowly under acidic conditions (Stumm and Lee, 1961), so pyrite oxidation by Fe^{3+} (Eq. (1-6)) should have been limited. In the natural environment, however, the oxidation of Fe^{2+} to Fe^{3+} is enhanced and sustained by microbial activities, which continues and promotes the formation of AMD (Baker and Banfield, 2003; Johnson and Hallberg, 2005; Tabelin et al., 2017). AMD generated from the metal/coal mines is very acidic and contains high concentrations of metal ions (Table 1-1). If left untreated, AMD might flow into the environment and contaminate the receiving water bodies and soils.

Pyrite is not the only sulfide mineral important in AMD formation, arsenopyrite, chalcopyrite ($CuFeS_2$), galena (PbS), gersdorffite ($NiAsS$), pyrrhotite, and sphalerite (ZnS) have also been reported to contribute in the acidification of leachates (Chopard et al., 2017). In nature, acid-consuming minerals like carbonates and silicates typically exist together with acid-producing minerals like most of the sulfide minerals, so the leachate pH is determined by the balance between acid producing potential (AP) and neutralization potential (NP) of mineral mixtures (White et al., 1999). In other words, AMD is formed when the neutralization potential ratio (NPR; NP/AP) is less than 1. If NPR is greater than 1, contaminated neutral drainage (CND) is generated instead that sometimes contains more soluble metal(loid)s like As, Cu, Mn, nickel (Ni), selenium (Se), and Zn (Calugaru et al., 2016; Plante et al., 2014; Tabelin et al., 2018).

1.2.2 Remediation techniques

When AMD formation is unavoidable, suitable treatment techniques should be applied to minimize its environmental impact on the receiving water streams and rivers. In general, these techniques are categorized as either active or passive process; that is, the former (i.e., active treatment) requires the continuous supplies of chemicals, energy and labors while the latter (i.e., passive treatment) only needs occasional maintenance. In this section, the mechanisms and characteristics of the commonly used techniques involving both active and passive will be discussed.

Table 1-1. A list of the number of abandoned/closed mines around the world and the geochemical characteristics of acid mine drainages (AMDs) generated from some representative mines in these countries.

Country	Abandoned/ closed mine	Representative mines (ore-type)	pH	EC ($\mu\text{S}/\text{cm}$)	Fe (mg/L)	Al (mg/L)	Mn (mg/L)	SO_4^{2-} (mg/L)	References
Australia	> 60,000	Jumna (Sn)	2.6–3.9	1810–3410	0.2–148	30–129	7.2–64.2	1020–1960	Edraki et al. (2005), Harris et al. (2003), Lottermoser and Ashley (2006), Unger et al. (2012)
		Montalbion (Ag)	3.4	1438	12.1	27.7	18.5	525	
		Mt. Morgan (Au-Cu)	2.6–3.8	–	13–1487	209–3074	51.1–355.0	8390–56,240	
Canada	10,139	Les Mines Gallen (Zn-Au-Ag)	1.8	–	29,800	3520	146	–	Lyew and Sheppard (1997), Mackasey (2000), Rao et al. (1993)
		Mattabi (Cu-Zn-Pb-Ag)	2.5–3.0	–	209	131.1	36.7	1324	
China	5383 (only in Jiangxi and Zhejiang)	Sitai (REE)	3.6	–	4.7	8.8	4.2	1860	Hua (2018), Li (2016), Wu et al. (2009), Yang et al. (2014), Zhao et al. (2007)
		Tongling (Cu)	2.1–3.5	1810–5890	8.5–121.2	5.0–33.7	0.7–6.2	833–6272	
		Xingren (Coal)	2.7–8.4	373–4010	0.01–740	0.01–180	19.5	18.1–3480	
Japan	5487	Central Hokkaido	3.2	–	211	122	15.7	1820	Fukushi et al. (2003), Herrera et al. (2007a, 2007b), Kano (2000), Yamaguchi et al. (2015)
		Nishinomaki (As)	3.1	947	13.5	10.5	6.5	374	
		Northern Honshu (Cu)	2.1	–	715–739	45.1–46.1	–	2800–2818	
		Tomitaka (Au)	2.8–3.2	1310–1617	0–260	–	–	480–700	
Philippines	800	Bagacay (Cu-Zn)	2.3–3.0	–	4–5	–	–	–	David (2003), Doyle (2007), NPSENRM (2014)
		Marcopper (Au-Cu-Zn)	4.8–5.0	–	0.6–0.7	5–8	11–12.4	–	
South Africa	> 6000	Mpumalanga (Coal)	2.0	600	8000	300	300	30,000	Masindi (2017), Muliwa et al. (2018), Olalde (2016), Tutu et al. (2008)
		Witbank (Coal)	2.4	12,410	6120	506	155	28,980	
		Witwatersrand (Au)	2.3–6.9	520–10,650	0.05–270	0.03–629	0.01–120	109–7570	

Table 1-1 (continued).

Country	Abandoned/ closed mine	Representative mines (ore-type)	pH	EC ($\mu\text{S/cm}$)	Fe (mg/L)	Al (mg/L)	Mn (mg/L)	SO_4^{2-} (mg/L)	References
South Korea	1692	Dogye (Coal)	2.8	1,870	146	35	7.0	2,280	Cheong et al. (2016), Kang et al.
		Donghae (Coal)	3.8–7.3	475–835	0.0–1.5	0.03–22.7	0.0–3.1	117–652	(2008), Kim (2009), Kim et al.
		Ilgwang (Cu)	2.7	–	440	60.7	14.3	1,997	(2003), Park and Jeong (1999),
		Kwangyang (Au-Ag)	2.9–3.2	116.1	41.7–42.5	13.6–18.7	0.3–0.8	–	Ryu et al. (2014)
		Ilwal (Coal)	2.3–3.4	750–771	0.8–1.1	4.6–6.7	12.8–28	608–635	
UK	> 2000	Bullhouse (Coal)	5.9	–	61	1.2	15	–	Bowell (2002), Johnson (2003),
		Mynydd Parys (Cu-Pb-Zn)	2.5	2506	563–650	2.2–70.0	10.0–15.8	800–3100	Kay et al. (2013)
		Wheal Jane (Sn-Cu)	3.6	–	130	50	20	350	
		Ynysarwed (Coal)	6.2	–	160	20	–	460	
USA	> 550,000	Elizabeth (Cu)	3.3	1978	123	13	2.6	1200	Anon (1993), Balistrieri et al.
		Friendship Hill site (Coal)	2.9	–	167	56	9.8	2200	(2007), Clyde et al. (2016),
		Williams Brothers (Au-Zn-Pb)	3.9	–	4.6	–	1.2	101	Hammarstrom et al. (2003)

Note: “–” means not reported.

1.2.2.1 Passive treatment system

Passive treatment systems, an energy saving and environmentally friendly water treatment technology, typically utilize natural construction materials (e.g., soil, clay and rock) and natural materials (e.g., limestone, plant residues like straw, wood chip, manure and compost) (INAP, 2009). Because of this, the capability of treating AMD is limited, so it should accommodate AMD having low acidity and slow flow rate for successfully remediating AMD. Passive treatment systems are suitable to treat influent water with the characteristics shown in Table 1-2.

Table 1-2. Broad guideline for determining the suitability of passive treatment system based on influent water characteristics (Taylor et al., 2005).

Treatment system	Av. Acidity Range (mg CaCO ₃ /L)	Av. Acidity Load (kg CaCO ₃ /day)	Av. Flow rate (L/s)	Typical pH range	Max pH attainable
Passive	1–800	1–150	< 50	> 2	7.5–8.0

➤ Anoxic limestone drains (ALD)

Anoxic limestone drain (ALD) is a buried trench of limestone (CaCO₃) gravels with drainage lines that are capped with an impermeable layer such as clay (Figure 1-1). This impermeable layer plays an important role in limiting oxygen availability to influent water because O₂ can oxidize Fe²⁺ to Fe³⁺ that favors precipitation and causes problems with clogging. Moreover, the influent water should not contain high concentration (> 1 mg/L) of dissolved Al because it is readily precipitated when reacted with limestone, leading to a clogging problem. When limestone is dissolved, Ca²⁺ ion is necessarily released into the system and it reacts with sulfate anion (SO₄²⁻), resulting in the formation of gypsum (CaSO₄·2H₂O). All precipitates (e.g., metal-oxyhydroxides and gypsum) formed in ALD can cause a premature system failure by clogging pore spaces and by coating the limestone surface (i.e., armoring effect) inhibiting further dissolution. Because of these limitations, ALD is more suited for treating AMD generated from coal mines than metal mines (Hammarstrom et al., 2003; Taylor et al., 2005). ALD treatment is usually followed by aerobic pond or wetland that allow the oxidation of Fe²⁺ to Fe³⁺ and its precipitation.

➤ Oxidic limestone drains (OLD)

Most of AMD contains high concentrations of dissolved oxygen (DO), Fe³⁺ and Al³⁺ (> 1 mg/L), which means that the application of ALD for treating AMD is limited (Cravotta, 2008). Oxidic limestone drain (OLD) is almost similar to ALD but it makes no attempts to prevent O₂ introduction into the system and to minimize the formation of precipitates (Figure 1-1). A large amount of limestone is used in OLD compared to ALD to continuously supply alkalinity even if some of

limestones are coated with precipitates. In addition, OLD incorporates flushing pipes that regularly open to remove precipitates (Cravotta, 2008). However, both ALD and OLD can raise the pH of influent water up to 6–8, indicating that only those metal ions that reach saturation below this pH can be precipitated and removed (Figure 1-2).

➤ Aerobic wetland

Aerobic wetland is a shallow pond with a large surface, which provides time for precipitating dissolved metals and settling suspended solids. Unlike other passive treatment techniques, aerobic wetland does not neutralize AMD but allows dissolved metals to be oxidized (e.g., Fe^{2+} to Fe^{3+}) and subsequently precipitated. Because of this, only net-alkaline influent water can be treated in an aerobic wetland, so it is commonly incorporated with ALD. Macrophytes are planted to prevent water channeling and to filter and stabilize the accumulating precipitates. (Johnson and Hallberg, 2005). Some macrophytes can supply oxygen from aerial parts to their root systems, accelerating the oxidation of dissolved metals.

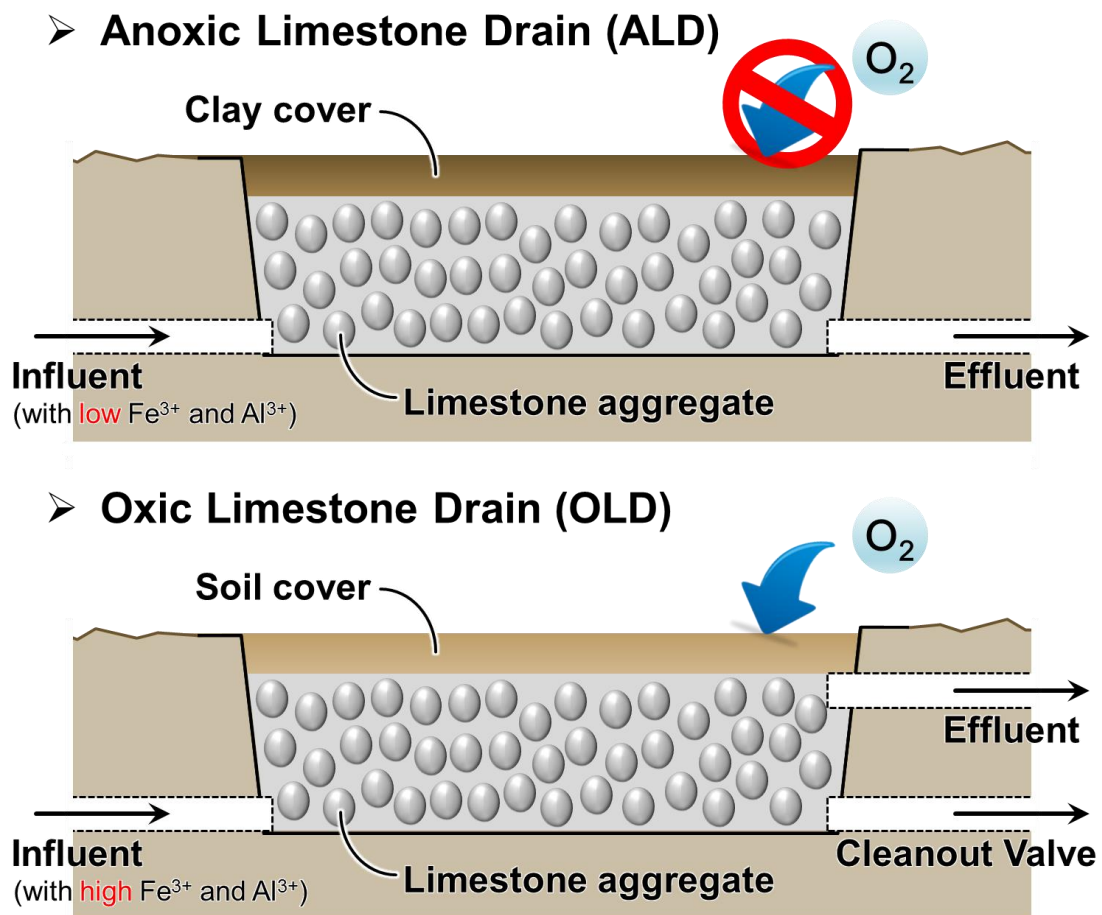


Figure 1-1. The schematic diagrams of anoxic and oxic limestone drains (ALD/OLD).

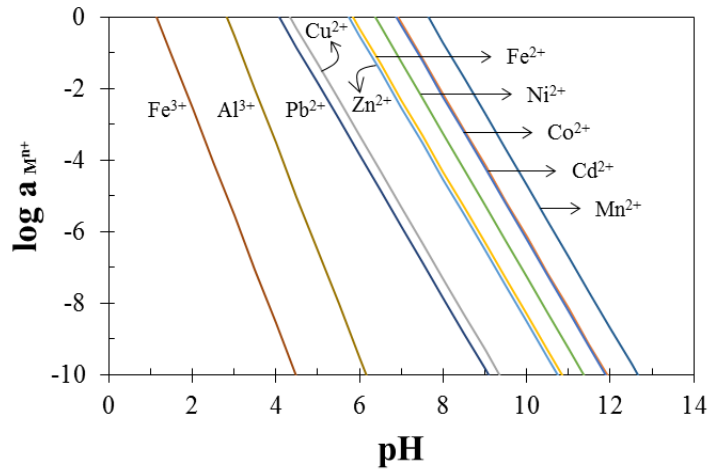


Figure 1-2. The solubility diagram of metal hydroxides as a function of pH.

➤ Anaerobic wetlands

Anaerobic wetland is a water retention pond comprising a substrate of organic matter and limestone aggregate as illustrated in Figure 1-3 (Taylor et al., 2005). It relies on chemical and microbial activities to precipitate dissolved metals and neutralize acidity. This system can maintain anaerobic conditions due to organic matters having high biological oxygen demand (BOD). A key process of this technique is the action of sulfate reducing bacteria (SRB) that reduces sulfate (SO_4^{2-}) to hydrogen sulfide (H_2S). Alkalinity (bicarbonate, HCO_3^-) is produced by a combination of decomposition of organic matter and dissolution of limestone. As shown in Figure 1-4, the solubility of metal sulfide is relatively low compared to that of metal hydroxide (Figure 1-2), so anaerobic wetland can remove such metal ions (e.g., Cd^{2+} , Co^{2+} , Mn^{2+} and Ni^{2+}) that are difficult to precipitate by just raising the pH.

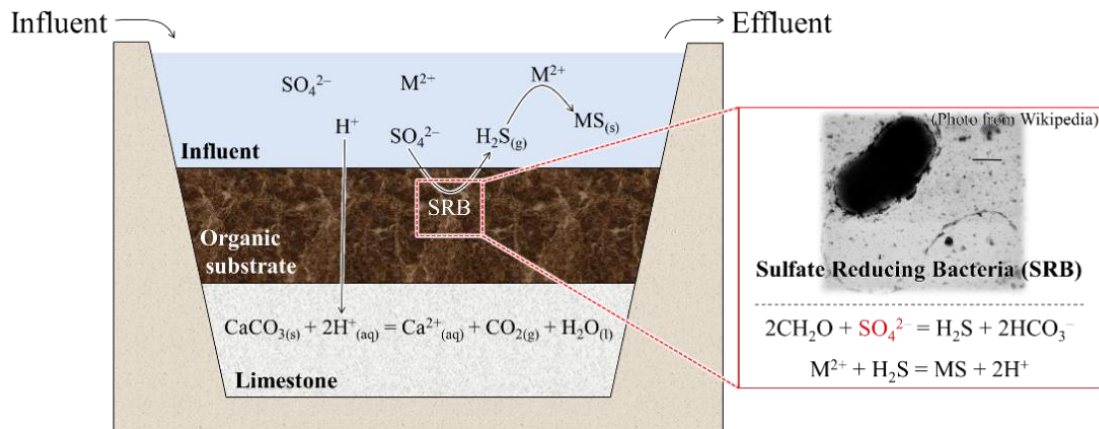


Figure 1-3. The schematic diagram of anaerobic wetland.

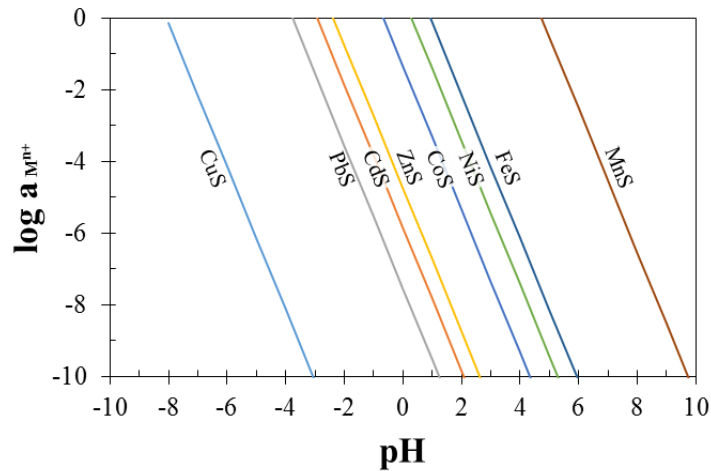


Figure 1-4. The solubility diagram of metal sulfides as a function of pH ($[H_2S] = 1 M$).

➤ Reducing and alkalinity producing system (RAPS)

Reducing and Alkalinity Producing System (RAPS), also referred to as Successive Alkalinity Producing System (SAPS) and Vertical Flow Wetland (VFW), is similar to an anaerobic wetland but it allows influent water to flow vertically through layers of organic substrate to remove DO and limestone gravel to neutralize acidity (Skousen, 1997; Taylor et al., 2005). This system was initially developed to overcome strict requirements of ALD (DO and $Fe^{3+} < 2 \text{ mg/L}$) (INAP, 2009). When influent water passes through a layer of organic substrate, anaerobic conditions are induced because of DO consumption by the decomposition of organic matter, resulting in the reduction of Fe^{3+} to Fe^{2+} . Because of this, the system can limit the formation of ferric hydroxide coating on limestone surface that hinders its dissolution producing alkalinity. RAPS, similar to ALD, is usually combined with other treatments (e.g., aerobic pond or wetland) to oxidize Fe^{2+} to Fe^{3+} and precipitate it.

1.2.2.2 Active treatment system

Unlike passive treatment systems, active treatment systems require continuous chemical addition, maintenance and monitoring, incurring high capital ($> AU\$100,000$) and operational costs ($> AU\$100,000/\text{year}$), but it can be engineered even for severe AMD with high acidity and a rapid flow rate (Table 1-3; Taylor et al., 2005). Some metal ions that tend to precipitate at pH above 8.0 (e.g., manganese) are hard to be removed by passive treatment system (Figure 1-5), but active treatment systems have no problem in removing these metal ions because this approach can raise the pH of AMD up to 14. There are a variety of techniques (e.g., aeration, neutralization, chemical precipitation, adsorption, ion exchange, membrane filtration, and sulfidogenic bioreactor) that fall

under active treatment system, but the most commonly used technique is undoubtedly neutralization (INAP, 2009; Johnson and Hallberg, 2005; Taylor et al., 2005; Trumm, 2010).

Table 1-3. Broad guideline for determining the suitability of active treatment system based on influent water characteristics (Taylor et al., 2005).

Treatment system	Av. Acidity Range (mg CaCO ₃ /L)	Av. Acidity Load (kg CaCO ₃ /day)	Av. Flow rate (L/s)	Typical pH range	Max pH attainable
Active	1–10,000	1–50,000	No Limit	No Limit	14

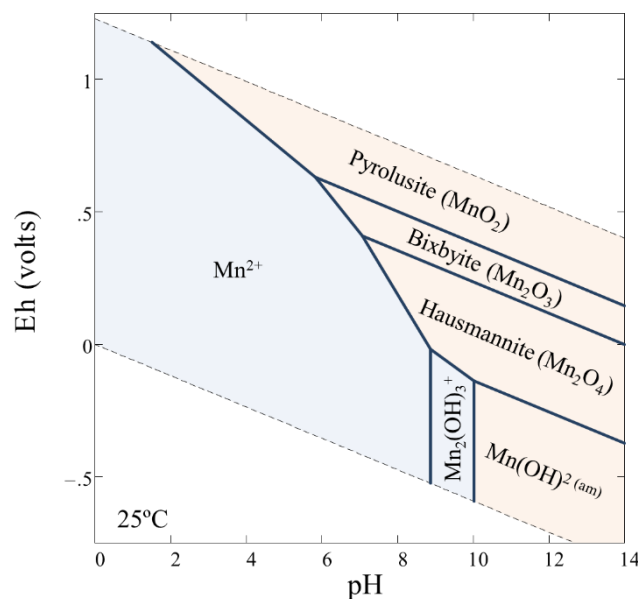


Figure 1-5. Eh-pH predominance diagram of Mn²⁺-H₂O system at 25 °C, 1.013 bar, and activity of Mn²⁺ = 10⁻³ (Bethke, 1992; Gustafsson, 2010).

Neutralization is a technique that uses neutralizing agents to raise the pH of AMD, thereby precipitating dissolved metals and producing clean water. The commonly used neutralizing agents are listed in Table 1-4. The appropriate selection of neutralizing agents, which depends on the characteristics of AMD, is very important for the successful and sustainable treatment. Sometimes, oxidation processes (e.g., aeration and/or addition of oxidant like hydrogen peroxide (H₂O₂)) are employed to accelerate Fe²⁺ oxidation to Fe³⁺ after raising pH by neutralization process. Although effective, a significant drawback of this technique is the production of a large volume of sludge containing only 2–4% solids (Johnson and Hallberg, 2005). To counter this problem, modification to this technique called the high density sludge (HDS) process was developed. The main difference of HDS process is that a portion of sludge collected from thickener is recycled back to a neutralizing

reactor (Figure 1-6). As a consequence, it can produce a sludge containing ca. 20% solids, which further concentrates to ca. 50% solids by dewatering, because the recirculated sludge particles enhance nucleation of dissolved metal onto their surfaces rather than the formation of a new particle (Johnson and Hallberg, 2005; Taylor et al., 2005; Wolkersdorfer and Howell, 2005).

Table 1-4. Chemical properties and costs associated with some AMD neutralization materials (Taylor et al., 2005).

Neutralization material	Saturation pH	Solubility (mg/L) in cold water	AU\$/tonne acid neutralized
Limestone (CaCO_3)	8.0 – 9.4	14	15 – 45
Dolomite ($\text{CaMg}(\text{CO}_3)_2$)	8.0 – 9.5	10 – 300	15 – 45
Quicklime (CaO)	12.4	1300 – 1850	130 – 300
Hydrated lime ($\text{Ca}(\text{OH})_2$)	12.4	1300 – 1850	150 – 350
Caustic magnesia (MgO)	9.5 – 10.8	1 – 50	300 – 600
Mg hydroxide ($\text{Mg}(\text{OH})_2$)	9.5 – 10.8	1 – 50	400 – 650
Soda ash (Na_2CO_3)	11.6	75,000	500
Caustic soda (NaOH)	14	450,000	700 – 900
Ammonia (NH_3)	9.2	900,000	400 – 600

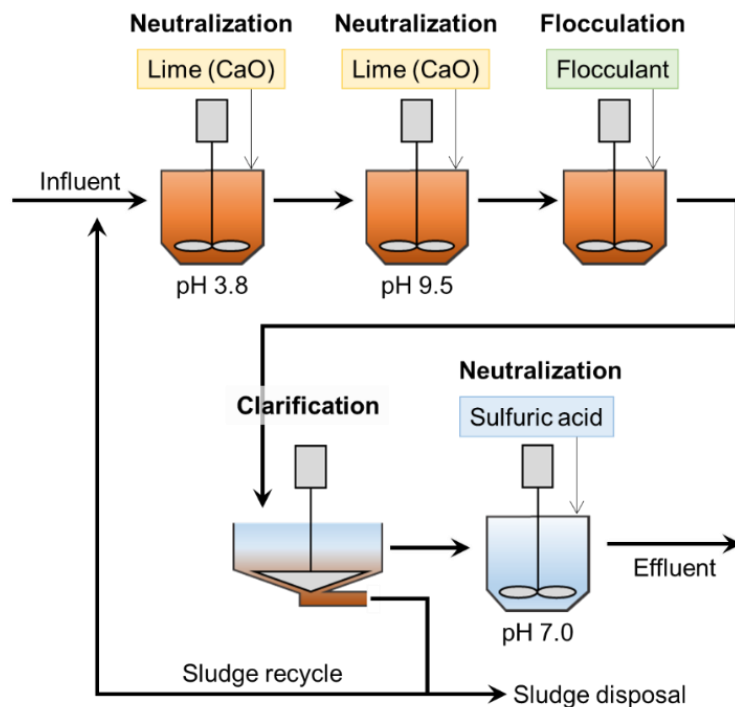


Figure 1-6. The schematic diagram of high density sludge (HDS) process.

1.2.3 Prevention techniques

As mentioned earlier, the formation of AMD is mainly caused by pyrite oxidation in the presence of O₂, water and/or microorganism (e.g., iron-oxidizing bacteria), which means that AMD formation could be limited by excluding any of these three components. Based on this concept, many prevention techniques that inhibit AMD formation have been developed as an alternative strategy to remediation techniques (Table 1-5). In this section, the conventional and state-of-the-art prevention techniques will be discussed.

1.2.3.1 Oxygen barrier

One of the most commonly used techniques to limit O₂ availability to sulfide-rich mine wastes is the application of oxygen barriers such as dry covers and water cover or by subaqueous disposal. For dry covers, various materials like non-reactive fine mine residue and natural till (Molson et al., 2004), low-sulfide tailings (Bussière et al., 2004; Demers et al., 2008), a combination of clay/ash and AMD treatment sludge/natural soil (Demers et al., 2017; Soares et al., 2009, 2010), industrial alkaline wastes (Bellaloui et al., 1999; Chtaini et al., 2001), and organic materials (Peppas et al., 2000; Ribet et al., 1995)) have been effectively used to suppress AMD formation. The overlying layer used in this technique, which is made up of fine-grained materials, has been extensively examined to understand how this kind of system works. Several authors reported that the high degree of saturation in this system occurs via capillary barrier effect, a condition that not only reduces water percolation but also O₂ influx into the underlying mine wastes. The limited supply of water and O₂, both essential components for sulfide oxidation, suppresses pyrite oxidation and AMD formation (Fig. 1-7a). Bussière et al. (2004), for example, evaluated the potential of low-sulfide tailings as a dry cover with capillary barrier effect (CCBE) material using column leaching tests for ca. 400 days. In the control column (i.e., sulfide tailings without any cover), an acidic leachate (pH < 3) with elevated concentrations of dissolved metals (60 g Zn and 4 g Fe) and SO₄²⁻ (120 g) was generated, whereas the effluent from the column with CCBE material remained near neutral pH and the concentrations of dissolved metals and SO₄²⁻ were substantially lower (0.006 g Zn, 0.02 g Fe and 5 g SO₄²⁻). This high performance of CCBE in limiting AMD formation was attributed to the dramatic decrease (up to 90%) of O₂ influx into the mine wastes. Using the same concept but with a different configuration, Igarashi et al. (2006) used a clayey silty soil to encase pyrite-rich excavated rocks in a truncated-pyramid miniature impoundment (Fig. 1-7b). Their field tests showed that O₂ concentration inside the waste rock rapidly decreased to about 1.5% due to the oxidation of sulfide minerals but was not replenished because of the low permeable cover that limited O₂ diffusion into the pyritic wastes, thereby reducing the oxidation rate of sulfide-bearing minerals by up to 93%. Other dry covers made of low-sulfide tailings, desulfurized tailings, silty materials, and industrial or municipal wastes, such as fly ash, bottom ash, cement kiln dust (CKD), red mud, paper mill waste,

pulp/paper residue, and organic wastes have also been reported to limit the formation of AMD by sustaining the high degrees of water saturation of overlying/covering layers (Bellaloui et al., 1999; Bussière et al., 2007; Cabral et al., 2000; Chtaini et al., 2001; Demers et al., 2008; Duchesne and Doye, 2005; Mollamahmutoğlu and Yilmaz, 2001; Molson et al., 2004, 2008; Peppas et al., 2000; Ribet et al., 1995; Soares et al., 2009, 2010). A recent study by Demers et al. (2017) evaluated the potential of sludge produced from AMD neutralization process as possible replacement for natural soil used as covering materials. This sludge is fine ($D_{50} = 25 \mu\text{m}$) enough to act as CCBE and has a high neutralization potential because of the presence of unreacted lime. The results of laboratory column tests for over 500 days and field tests for ca. 4 years showed that a cover layer composed of sludge-soil mixture (25%-75% by weight) over either waste rock or tailings effectively suppressed AMD generation. This strategy improved the quality of effluent generated from the wastes and eventually passed the effluent regulation criteria of Quebec (Directive 019).

Another way to remove oxygen in a system and limit AMD formation is to introduce organic carbon-rich materials like sewage sludge, composted municipal wastes, and sawdust. The decomposition of carbon-rich compounds consumes a large amount of O_2 (i.e., biological oxygen demand (BOD)) (Eq. (1-7)), which suppresses pyrite oxidation and AMD formation because of the very low DO concentration.



The use of organic-rich wastes, however, has one serious drawback. According to Ribet et al. (1995), organic cover may induce the reductive dissolution of secondary minerals like Fe(III)-oxyhydroxides, leading to the release of toxic elements (e.g., As, Cd, Cu, Pb, and Se) previously adsorbed onto or coprecipitated with them.

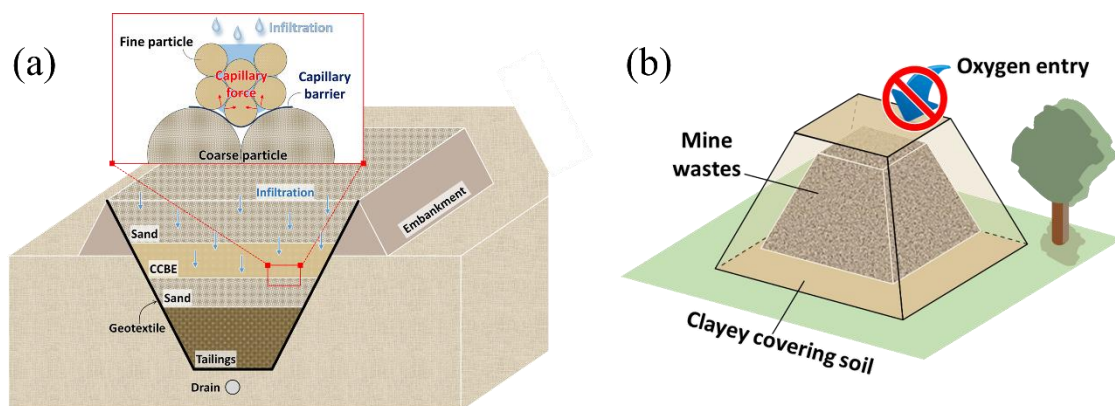


Figure 1-7. The schematic diagrams of (a) cover with capillary barrier effect and (b) impoundment.

Water covers are widely used as an oxygen barrier because of the very slow O_2 diffusion in water ($1.90 \times 10^{-9} \text{ m}^2/\text{s}$) compared with that in the air ($1.98 \times 10^{-5} \text{ m}^2/\text{s}$) as illustrated in Fig. 1-8 (Elberling and Damgaard, 2001; Moncur et al., 2015; Schmitz et al., 2013; Vigneault et al., 2001). For instance, Moncur et al. (2015) investigated the long-term mineralogical and geochemical changes in sulfide mine tailings subjected to two types of weathering for over 60 years: (1) exposed to atmospheric conditions (i.e., sub-aerial tailings), and (2) stored under a 100 cm deep water cover (i.e., sub-aqueous tailings). The core samples of both sub-aerial and sub-aqueous tailings were collected and characterized, and the results showed that the former was extensively oxidized and exhibited a weathering zone that extended from the surface up to a depth of about 40 cm while the latter was only mildly oxidized and the weathering zone was limited to around 6 cm below the water-tailings interface. Moreover, geochemical properties of pore water collected from the sub-aerial and sub-aqueous tailings were consistent with differences of the extent of weathering suggested by the mineralogical characterization of core samples; that is, the former was acidic (pH 1.9–4.43) and contained elevated concentrations of dissolved Fe (3,500–28,000 mg/L) and S (7,900–59,000 mg/L) while the latter was circumneutral (pH 7–7.15) and contained relatively lower concentrations of Fe (0.16–1.35 mg/L) and S (1,600–1,700 mg/L). These results suggest that the use of a water cover is a promising approach to limit the formation of AMD. Unfortunately, this technique is not applicable in arid and semi-arid regions where annual evaporation exceeds precipitation because drying out of saturated tailings will expose them to atmospheric conditions, thereby generating AMD (Lottermoser, 2003).

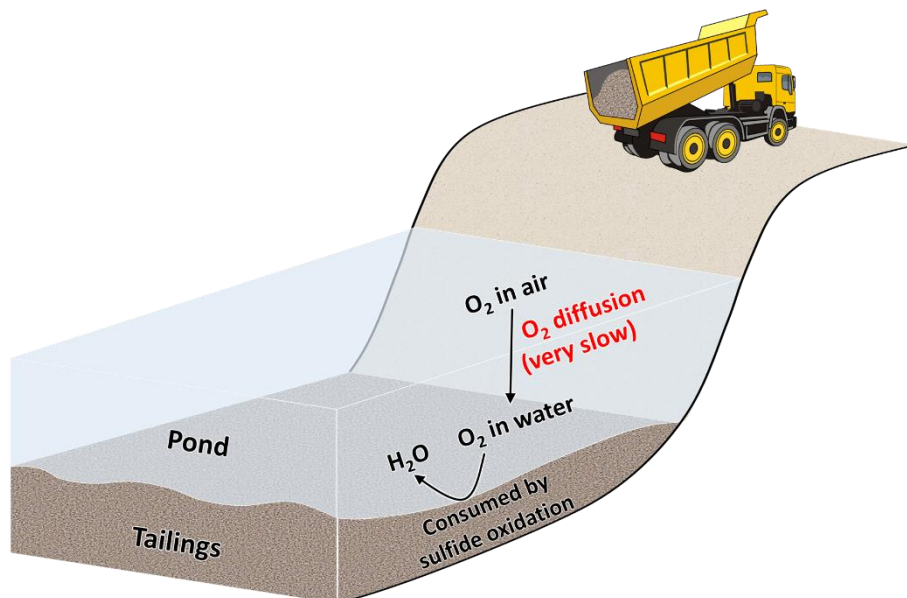


Figure 1-8. The schematic diagram of sub-aqueous disposal.

1.2.3.2 Bactericide

Microorganisms like acidophilic iron- and sulfur-oxidizing bacteria (e.g., *Thiobacillus ferrooxidans* and *Thiobacillus thiooxidans*) are known to accelerate pyrite oxidation, which means that the absence of microorganisms in sulfidic mine wastes could slow down and limit the formation of AMD (Evangelou, 1995; Johnson and Hallberg, 2003; Lottermoser, 2003; Sasaki et al., 1998). Based on this concept, bactericides such as anionic surfactants, cleaning detergents, organic acids, and food preservatives have been used to inhibit the growth of these microorganisms (Evangelou, 1995; Kleinmann, 1982; Kleinmann and Erickson, 1983; Lottermoser, 2003; Parisi et al., 1994; Zhang and Wang, 2017). Acidophiles, the type of bacteria that enhances and sustains AMD formation, thrive under highly acidic conditions (less than pH 3) but to survive, they require a circumneutral intracellular pH between 6.5 and 7.0, which they achieve by restricting proton entry into the cell via the cytoplasmic membrane (Baker-Austin and Dopson, 2007). However, anionic surfactants allow protons to penetrate freely into the bacteria's cell membranes causing disruptions of enzymatic functions at low concentrations and eventual death of the cell at high concentrations (Evangelou, 1995; Lottermoser, 2003; Zhang and Wang, 2017). Similarly, organic acids are harmful to acidophiles because they uncouple the respiratory chain of these microorganisms under acidic conditions via the penetration of their protonated forms through the cell membrane which then deprotonates while inside the cells releasing harmful H^+ (Baker-Austin and Dopson, 2007). Kleinmann and Erickson (1983) utilized sodium lauryl sulfate (SLS) as a bactericide and reported that acid production and iron concentration decreased by around 60–95% and 90–95%, respectively due to the reduction of bacterial activity. The inhibitive performance of another surfactant, sodium dodecyl sulfate (SDS), was also reported by Zhang and Wang (2017). In the absence of SDS, these authors found that *Thiobacillus ferrooxidans* completely oxidized Fe^{2+} to Fe^{3+} after 6 days while only 23–24% of Fe^{2+} was oxidized to Fe^{3+} in the presence of 50 mg/L of SDS, indicating that SDS was effective in suppressing the activity of *Thiobacillus ferrooxidans*. However, utilization of bactericide cannot permanently inhibit microbial activity because these compounds are water-soluble and thus, are easily carried away from the sulfidic wastes-microorganism interface giving rise for the need to repetitively add bactericides to maintain minimal bacterial activities. Because of this short term effect, Parisi et al. (1994) needed to spray sodium dodecylbenzene sulfonate over Branchton refuse disposal area in Butler County, Pennsylvania four times a year, which limited the generation of acidity while at the same time lowering the concentrations of Fe and Mn by 82 and 90%, respectively.

1.2.3.3 Co-disposal and blending

Co-disposal or blending of reactive mine tailings with either potentially acid consuming or alkaline producing materials has been considered as a promising approach to limit AMD formation. Basic materials like lime, limestone, and phosphate minerals (e.g., apatite) have been used because they consume H^+ generated by sulfidic tailings, thereby not only producing circumneutral drainage (Eqs. (1-8) and (1-9)) but also immobilizing soluble metals and metalloids via precipitation (Hakkou et al., 2009; Lottermoser, 2003; Miller et al., 2006; Mylona et al., 2000).



According to Mylona et al. (2000), limestone blending controlled pyrite oxidation via four mechanisms: (1) precipitation of Fe^{3+} that limits the supply of oxidants, (2) increase in pH (pH 6.1–8.4) that impairs the activity of microorganisms (e.g., *Thiobacillus ferrooxidans*), (3) coating formation on the surface of sulfide minerals that reduces their reactive surface areas, and (4) formation of a cemented layer (hardpan) consisting of ferric-oxyhydroxide and gypsum with very low permeability that limits the diffusion of O_2 and infiltration of water (Blowes et al., 1991; Kelley and Tuovinen, 1988; Lin, 1997; Nicholson et al., 1988, 1990; Tasse et al., 1997).

In recent years, industrial by-products and residues (e.g., red gypsum, sugar foam, ashes from biomass combustion, green liquid dregs, fly ash, mesa lime, argon oxygen decarburization slag, cement kiln dust, and red mud bauxite) have become popular blending materials to inhibit the formation of AMD due to their high neutralization potentials (Alakangas et al., 2013; Doye and Duchesne, 2003; Rodríguez-Jordá et al., 2012; Xenidis et al., 2002; Yeheyis et al., 2009). For co-disposal or blending operation to be successful, the correct stoichiometric balance between acid producing and acid consuming materials must be applied. For instance, the lack of acid consuming materials would fail to neutralize the acidic leachate whereas excessive amounts may result in the formation of strongly alkaline leachates (i.e., $pH > 10$) that increases the solubility of some hazardous metals like Al, Cu, Ni, Pb, and Zn (Tabelin et al., 2018a). It is also important to attain homogeneous mixing of acid consuming materials with reactive mine tailings to maximize the efficiency of this approach. If not, preferential water flow through the reactive mine tailings with limited basic materials may result in the formation of acidified leachates as illustrated in Fig. 1-9.

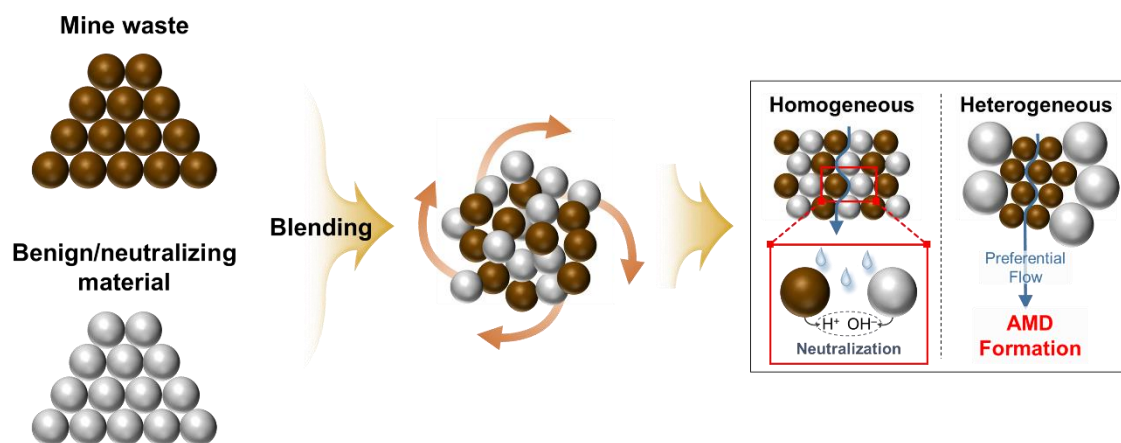


Figure 1-9. The schematic diagram of blending of mine wastes with neutralizing materials.

1.2.3.4 Passivation

➤ Organic coatings

The formation of organic coatings on the surface of sulfide minerals could potentially suppress pyrite oxidation because these kinds of coatings not only make the mineral surface hydrophobic that limits water-mineral interactions but also reduces the exposed surface area of sulfide minerals by acting as physical barriers. For example, sodium oleate ($CH_3(CH_2)_7CH=CH(CH_2)_7COONa$), a commonly used organic collector in flotation, had been utilized to form an inert hydrophobic film on pyrite (Jiang et al., 2000). According to these authors, oleate ions suppressed pyrite oxidation via two mechanisms: (1) it limits the concentration of Fe^{3+} at $pH < 8$ via precipitation reducing available oxidants to pyrite, and (2) oleate ions favorably coordinates with Fe^{2+} and Fe^{3+} of partially oxidized pyrite and forms an organic coating that makes pyrite electrochemically inactive. Their weathering test results also showed that the Fe-oleate coating formed on pyrite was quite stable and limited the oxidation of pyrite for up to 30 days. The effectiveness of coating was also improved if additional oleate solution is sprayed on the tailings at 5-day intervals.

Natural organic matter (NOM) like humic acid and lignin has also been reported to passivate pyrite and limit its oxidation (Açai et al., 2009; Belzile et al., 1997; Lalvani et al., 1990). Açai and coworkers (2009), for example, noted that the adsorption of humic acid on pyrite was almost irreversible because of its strong affinity to intermediate hydrated ferric sulfate ($Fe_2(SO_4)_3 \cdot nH_2O$ ($n=0-7.5$)) and ferric oxyhydroxide ($Fe(OH)_3$ and $FeOOH$) phases formed during the partial oxidation of pyrite. These authors used cyclic voltammetry, an electrochemical technique that measures the amount of electrons lost or gained with changes in applied potential, to evaluate the effects of humic acids on the electrochemical properties of pyrite. Their results confirmed that

adsorbed humic acids on pyrite made the mineral electrochemically inactive, indicating that organic molecules like humic acids could passivate pyrite. In the work of Lalvani et al. (1990), several organic compounds (e.g., acetyl acetone, humic acid, lignin, oxalic acid, and silanes) were examined to passivate pyrite and most of them (except the silanes (methyl triacetoxo silane, MTS)) were effective in lowering the corrosion current of pyrite.

Phospholipids having two hydrophobic tails, such as Egg Sphingomyelin (Egg SM), 1,2-Dipalmitoyl-SN-Glycero-3-[Phospho-L-Serine] (16:0 PS), 1,2-Dimyristoyl-SN-Glycero-3-[Phospho-RAC-(1-Glycerol)] (14:0 PG), 1-Palmitoyl-2-Palmitoyl-SN-Glycero-3-Succinate (16:0 DGS), 1,2-bis(10,12-tricosadiynoyl)-SN-Glycero-3-Phosphocholine (23:2 Diyne PC), 1,2-Di-O-Octadecyl-SN-Glycero-3-Phosphocholine (18:0 Diether PC) and 1,2-Distearoyl-SN-Glycero-3-Phosphocholine (DSPC), have also been used as coating materials to inhibit pyrite oxidation (Elsetinow et al., 2003; Kargbo et al., 2004; Zhang et al., 2003a, 2003b). The hydrophilic “head” in phospholipids are readily adsorbed onto the pyrite surface, which render it more hydrophobic due to the presence of two long hydrocarbon tails surrounding the mineral. The results of laboratory leaching tests showed that samples treated with two-tailed lipids were about 60–80% less oxidized than the control (without phospholipids) even under strongly acidic conditions ($\text{pH} < 2$) (Elsetinow et al., 2003; Zhang et al., 2003a). Moreover, Elsetinow et al. (2003) and Zhang et al. (2003a) found that the extent of suppression was related to the number of hydrocarbon tails and their length; that is, a single-tailed lipid (Stearic acid) and a short two-tailed lipid (1,2-Dipropionoyl-SN-Glycero-3-Phosphocholine (3:0 PC lipid)) were less effective than those having two long tails. Zhang and coworkers (2003b) improved the effectiveness of a two-tailed lipid (23:2 Diyne PC) to passivate pyrite by applying UV irradiation that polymerized and cross-linked the adsorbed lipids to form a more impermeable coating. According to Kargbo et al. (2004), however, silicates commonly found in the natural environments decreased the ability of lipids to suppress pyrite oxidation although the detailed mechanism remains unclear. Thus, the effects of coexisting components should be extensively studied before phospholipids could be applied to limit AMD formation of actual mine wastes.

Similarly, other organic materials, such as diethylenetriamine (DETA), triethylenetetramine (TETA), sodium triethylenetetramine-bisdithiocarbamate (DTC-TETA), methyl ethyl ketone formaldehyde resin modified carbazoles, and 8-hydroxyquinoline, had been shown to suppress the oxidation of iron sulfides (e.g., pyrite and pyrrotite) through the formation of hydrophobic coatings (Cai et al., 2005; Chen et al., 2006; Lan et al., 2002; Liu et al., 2013; Shu et al., 2013; Ustamehmetoğlu et al., 2013). Although many organic coatings have effectively passivated sulfide minerals, these results have been limited to small-scale and controlled laboratory experiments. The long-term stability of these organic-based coatings under natural conditions remains unclear and

should be thoroughly evaluated because in the environment, some microorganisms are known to degrade even very complex organic compounds, which could remove organic coatings and then restart pyrite oxidation and AMD formation.

➤ Microencapsulation

Under the right conditions, pyrite could passivate itself due to the formation of iron oxyhydroxide coatings on its surface. Nicholson et al. (1990) investigated the kinetics of pyrite oxidation in carbonate-buffered solution (pH 7.6–8.6) and confirmed that ferric oxyhydroxide layers accumulated with time on the pyrite surface that significantly lowered its rate of oxidation. These authors applied the shrinking core model to interpret their leaching results and concluded that the reaction rate was controlled by surface reactions but only for a relatively short period of time. Overall, diffusion through the product layer (i.e., ferric oxyhydroxide) of reactants and oxidation products appeared to be the rate determining step. Similarly, Huminicki and Rimstidt (2009) examined the rate of pyrite oxidation in a mixture of 0.3 M H₂O₂ and 0.1 M NaHCO₃ with pH of around 8.5, and they observed two oxidation rates: one with a shallow slope of r versus $t^{-1/2}$ ($r = 2.19 \times 10^{-6} t^{-1/2} + 3.42 \times 10^{-7}$) while the other has a steeper slope ($r = 7.72 \times 10^{-5} t^{-1/2} - 5.31 \times 10^{-8}$). Based on these results, they proposed that the mechanism of iron oxyhydroxide coating formation on pyrite occurs as follows: (1) the deposition of colloidal iron oxyhydroxide precipitates on the pyrite surface driven by electrostatic attraction between negatively charged pyrite and positively charged iron oxyhydroxide, and (2) the densification of coatings making it more impermeable. Fly ash also has the potential to encapsulate pyrite with iron oxyhydroxide coatings by supplying a sufficient amount of alkalinity (Pérez-López et al., 2007). However, the extrapolated results of Huminicki and Rimstidt (2009) suggest that pyritic mine wastes require extra sources of alkalinity for several decades to facilitate the formation of an iron oxyhydroxide coating thick enough to be effective. Under acidic conditions, formation of a passivating oxidation layer on pyrite was also reported by Tabelin et al. (2016). Using a pyrite-rich natural geologic containing arsenopyrite and melanterite, they found that a passivating oxidation layer on pyrite was formed, which was enhanced by the addition of hematite. The coating not only suppressed the oxidation of pyrite but also immobilized As via the formation of iron-arsenates (e.g., scorodite) and oxyhydroxide phases.

Huang and Evangelou (1992) developed a new microencapsulation technique that forms a ferric phosphate-dominated coating on pyrite using hydrogen peroxide (H₂O₂), phosphate (KH₂PO₄), and sodium acetate (CH₃COONa). These three components play critical roles in the formation of the surface protective layer; that is, H₂O₂ oxidizes surface Fe²⁺ to Fe³⁺, phosphate reacts with Fe³⁺ to form ferric phosphate, and sodium acetate maintains the pH at around 5 where ferric phosphate is stable (Fig. 1-10). The effectiveness of ferric phosphate coating in the suppression of pyrite oxidation was also reported in follow up papers of these authors and several later studies by other

groups (Evangelou 1995, 2001; Nyavor and Egiebor, 1995; Vandiviere and Evangelou, 1998). For example, Evangelou (1995, 2001) showed that pyrite was rapidly oxidized in 0.106 M H₂O₂ and about 35% of the mineral was consumed after 800 min, but in the presence of 0.001 M KH₂PO₄ (i.e., H₂O₂ + KH₂PO₄), pyrite dissolution was only less than 10%. This suppressive effect was further enhanced when sodium acetate was present in the system together with H₂O₂ and H₂PO₄⁻ (Evangelou, 1995, 2001).

Ji et al. (2012) compared the ability of soluble phosphate salt (i.e., KH₂PO₄) and partly soluble phosphate mineral (i.e., apatite, Ca₁₀(PO₄)₆(OH)₂) in the presence of an oxidant (either H₂O₂ or NaClO) and acetate buffer to passivate sulfides with ferric phosphate coatings. These authors reported that only the former suppressed sulfate production from pure pyrite as well as abandoned coal and metal mine wastes (about 70–93%) while the latter had negligible suppressive effects due most likely to the relatively low solubility of apatite. Ji et al. (2012) also evaluated the potential of MgO, KMnO₄, manganite (MnOOH), and cement as coating materials of pyrite. Mg²⁺ and Mn²⁺ are known to coprecipitate with Fe³⁺ under circumneutral conditions, which may eventually cover pyrite and prevent its oxidation (Azzam et al., 1969; Lee et al., 2002). After leaching for 8 days, MgO and KMnO₄ limited the production SO₄²⁻ by 61–65 and 47–82%, respectively. Among the six coating agents evaluated in the study of Ji and coworkers (2012), cement had the best result and suppressed the production of SO₄²⁻ by up to 95%, which could be attributed to the following reactions:

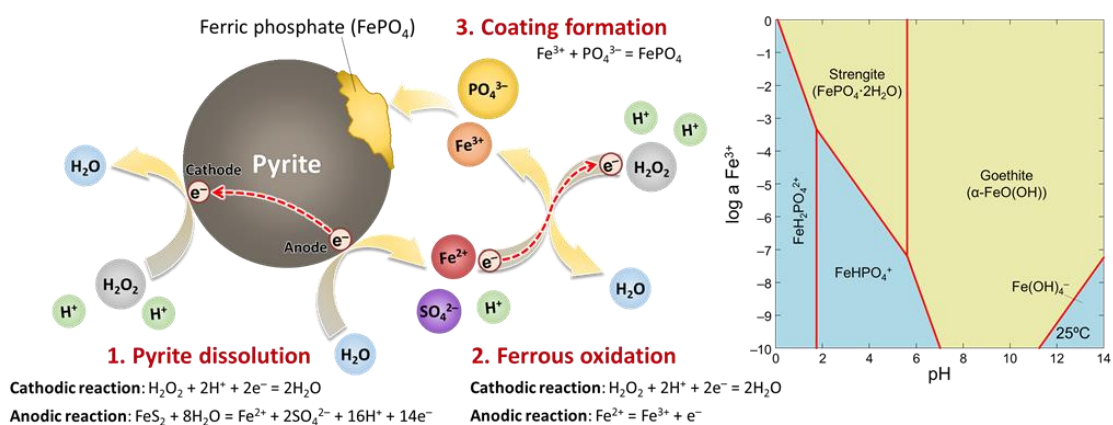
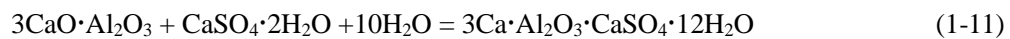
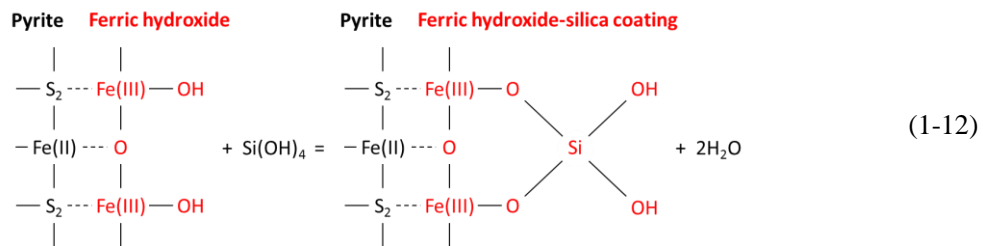


Figure 1-10. The schematic diagram of the formation of ferric phosphate coating on pyrite, and Log activity–pH predominance diagram of Fe³⁺ at 25 °C and 1.013 bar in the presence of PO₄³⁻ (a = 1.0) created using the Geochemist’s Workbench®.

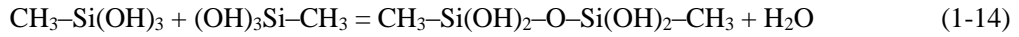
Evangelou (1996) developed another microencapsulation technique based on silicate rather than phosphate, which forms a ferric hydroxide-silica coating on the surface of sulfide minerals like pyrite and marcasite. In the presence of silicate, H₂O₂ and acetate buffer, pyrite was readily covered with a ferric hydroxide-silica coating where silicate ions are coordinated by the replacement of H in OH groups (Eq. (1-12)).



Zhang and Evangelou (1998) evaluated the effectiveness of this coating and found that pyrite dissolution in the coating solution (Si(OH)₄ + H₂O₂ + CH₃COONa) after 1,000 min was only about 10% while in the control (H₂O₂ only), almost 65% of the sample was oxidized. In addition, comparative studies between ferric phosphate and ferric hydroxide-silica coatings showed that the latter performed better than the former (Evangelou, 2001; Vandiviere and Evangelou, 1998). The use of silicate to passivate pyrite was also reported by other authors (Fan et al., 2017; Miller et al., 2009; Smart et al., 2010; Zeng et al., 2013). According to Fan et al. (2017), the oxidation of pyrite at neutral pH (7.4) formed an overlayer composed of crystalline goethite (α-FeOOH) or lepidocrocite (γ-FeOOH) with needle-like morphologies and porous structures (pore diameter: 10–100 nm). In the presence of silicate, a smooth, continuous, and coherent coating was formed but with an amorphous nature. This silicate-stabilized coating suppressed pyrite oxidation for ca. 290 days by over 97% (0.03 mmol/m²) in comparison to that without silicate (1.3 mmol/m²).

However, the use of phosphate and H₂O₂ in microencapsulation techniques explained previously has several drawbacks. Firstly, phosphate is a nutrient that governs the growth rate of organisms especially in freshwater ecosystems, so it may cause eutrophication of the receiving water bodies if used haphazardly (Khummalai and Boonamnuayvitaya, 2005). Secondly, H₂O₂ used for the production of Fe³⁺ is not only expensive but also difficult to store and handle in large scale applications because it is unstable especially at high concentrations (Ouyang et al., 2015). To overcome these limitations, silane-based coatings using alkoxysilanes have been proposed recently by other authors (Diao et al., 2013; Khummalai and Boonamnuayvitaya, 2005; Liu et al., 2017; Ouyang et al., 2015; You et al., 2013). Alkoxysilanes are composed of inorganic silicon atoms and functional organic groups (e.g., methoxy (CH₃O–) and ethoxy (CH₃CH₂O–)), and because these compounds have both inorganic and organic components, they have several advantages over pure inorganic or organic coatings; that is, the inorganic part imparts durability and superior adhesion to

the target surface while the organic part contributes in enhancing flexibility, crack-resistance, and compatibility with polymer coatings (Diao et al., 2013; Metroke et al., 2001). Khummalai and Boonamnuayvitaya (2005) examined the ability of methyltrimethoxysilane (MTMOS), tetramethoxysilane (TMOS), tetraethoxysilane (TEOS), and N-(2-aminoethyl)-3-aminopropyltrimethoxysilane (AAPS) to passivate arsenopyrite. Among them, MTMOS formed the most effective coating that decreased the rates of biological oxidation by *Acidithiobacillus ferrooxidans*-like bacterium by about 13% and H₂O₂-induced chemical oxidation by around 5% because of the formation of a crack-free coating on the surface of arsenopyrite. The mechanism of MTMOS coating formation involves the hydrolysis and condensation of MTMOS monomer as explained by the following reactions:



TEOS has been widely used to make Si—O—Si bonds via the sol-gel process. However, one problem with this coating was the deterioration of the silica network because of the breaking down of Si—O—Si bonds by nucleophilic attack of OH⁻ on Si atoms (Diao et al., 2013; Rao et al., 2003). To overcome the limitations of TEOS, Diao and coworkers (2013) examined the potential of n-propyltrimethoxysilane (NPS) to inhibit pyrite oxidation. In comparison to TEOS-based coating, NPS could form a crack-free coating because of the presence of non-hydrolyzable propyl groups that made the coating more flexible and hydrophobic. Because of this, NPS-based coatings successfully protected pyrite against both chemical and biological oxidations. Ouyang et al. (2015) investigated the passivation of pyrite using three organosilanes (i.e., γ -mercaptopropyltrimethoxysilane (PropS-SH), γ -aminopropyltrimethoxysilane (APS) and vinyltrimethoxysilane (VTMS)) and reported about the exceptional ability of PropS-SH to render pyrite electrochemically inactive, which was suggested by the very low corrosion current (0.09 $\mu\text{A}/\text{cm}^2$; Bare pyrite (1.80 $\mu\text{A}/\text{cm}^2$); APS (0.72 $\mu\text{A}/\text{cm}^2$); VTMS (0.36 $\mu\text{A}/\text{cm}^2$)) and the very high charge transfer resistivity (10.85 $\times 10^4 \Omega\cdot\text{cm}^2$; Bare pyrite (0.41 $\times 10^4 \Omega\cdot\text{cm}^2$); APS (1.73 $\times 10^4 \Omega\cdot\text{cm}^2$); VTMS (2.51 $\times 10^4 \Omega\cdot\text{cm}^2$)) of pyrite treated in this organosilanes. Furthermore, the passivation efficiency of PropS-SH was improved by adding appropriate amounts of SiO₂ nanoparticles, which filled micro-cracks of the coating and improved coating coverage (Liu et al., 2017). If added in excess, however, SiO₂ nanoparticles weakened the hydrophobicity of the coating due to the formation of SiO₂ aggregates with a large number of exposed hydrophilic hydroxyl groups.

➤ Carrier-microencapsulation (CME)

Although the previous passivation techniques could suppress the oxidation of sulfide mineral, it has a serious drawback; that is, these methods cannot specifically target sulfide minerals in complex systems, leading to unnecessarily large consumption of expensive reagents. A great improvement to those techniques was proposed by Satur et al. (2007) called carrier-microencapsulation (CME). CME uses a redox-sensitive organic compound to carry and deliver the coating material, usually an insoluble metal(loid) ion, preferentially to the surface of pyrite where it is adsorbed or precipitated to form the protective coating (Figure 1-11). The redox-sensitive complex used in CME could specifically target pyrite and arsenopyrite because their dissolution is electrochemical in nature (Crundwell, 1988; Rimstidt and Vaughan, 2003), a process that requires movement of electrons between distinct anodic and cathodic sites. Because CME could target pyrite and arsenopyrite even in complex systems containing other minerals like silicates and aluminosilicates, unwanted consumption of chemicals during treatment is dramatically reduced. This technique has been shown to suppress pyrite oxidation as well as pyrite floatability in coal flotation (Jha et al., 2008; 2011; Satur et al., 2007; Yuniati, 2015).

This chapter is edited from “Park et al., 2019. A review of recent strategies for acid mine drainage prevention and mine tailings recycling. Chemosphere 219, 588–606.”

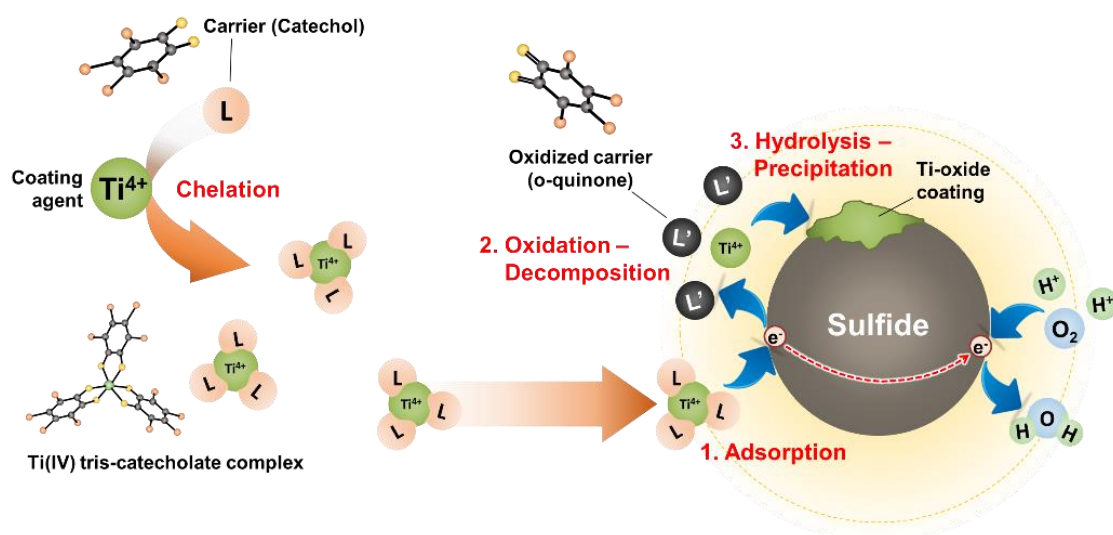


Figure 1-11. The schematic diagram of carrier-microencapsulation using Ti-catecholate complex.

1.3 Outline of the dissertation

The dissertation is comprised of five chapters and summaries of each chapter are outlined as follows:

Chapter 1 introduces statement of the problem and objectives of this study, background and literature reviews of the formation of AMD and its control.

Chapter 2 identifies the decomposition mechanism of Ti-catecholate complex, evaluates the effect of CME using Ti-catecholate complex on the suppression of As release from arsenopyrite, characterizes its surface treated by Ti-based CME, and finally proposes a detailed mechanism.

Chapter 3 investigates the effects of temperature and additives (e.g., Cu^{2+} and Cu-NH_3 complex) to improve the kinetics of Ti-based CME.

Chapter 4 examines the potential of Al-catecholate complex as an alternative to Ti-catecholate complex to overcome the limitation of Ti-based CME. In this chapter, the electrochemical behaviors of Al-catecholate complexes are elucidated, and their effects on the suppression of arsenopyrite oxidation and the detailed surface characterizations of arsenopyrite treated by Al-catecholate complex are investigated to propose a detailed mechanism of Al-based CME.

Chapter 5 gives the summary and conclusion of the dissertation.

References

- Ačai, P., Sorrenti, E., Gorner, T., Polakovič, M., Kongolo, M. and Donato, P., 2009. Pyrite passivation by humic acid investigated by inverse liquid chromatography. *Colloids Surf. A Physicochem. Eng. Asp.* 337 (1–3), 39–46.
- Alakangas, L., Andersson, E., Mueller, S., 2013. Neutralization/prevention of acid rock drainage using mixtures of alkaline by-products and sulfidic mine wastes. *Environ. Sci. Pollut. Res.* 20, 7907–7916.
- Anon, 1993. With or without reform, mining cleanup could cost \$71 billion. *U.S. Water News.* 10.
- Azzam, A.M., Elatrash, A.M., Ghattas, N.K., 1969. The co-precipitation of manganese by iron(III) hydroxide. *J. Radioanal. Chem.* 2, 255–262.
- Baker, B.J. and Banfield, J.F., 2003. Microbial communities in acid mine drainage. *FEMS Microbiol. Ecol.* 44, 139–152.

- Baker-Austin, C., Dopson, M., 2007. Life in acid: pH homeostasis in acidophiles. *Trends Microbiol.* 15 (4), 165–171.
- Balistrieri, L.S., Seal, R.R., Piatak, N.M., Paul, B., 2007. Assessing the concentration, speciation, and toxicity of dissolved metals during mixing of acid-mine drainage and ambient river water downstream of the Elizabeth Copper Mine, Vermont, USA. *Appl. Geochem.* 22, 930–952.
- Banks, D., Younger, P.L., Arnesen, R.-T., Iversen, E.R. and Banks, S.B., 1997. Mine-water chemistry: the good, the bad and the ugly. *Environ. Geol.* 32 (3), 157–174.
- Bellaloui, A., Chtaini, A., Ballivy, G., Narasiah, S., 1999. Laboratory investigation of the control of acid mine drainage using alkaline paper mill waste. *Water Air Soil Pollut.* 111, 57–73.
- Belzile, N., Maki, S., Chen, Y.-W., Goldsack, D., 1997. Inhibition of pyrite oxidation by surface treatment. *Sci. Total Environ.* 196, 177–186.
- Bethke, C.M., 1992. *The Geochemist's Workbench – A User's Guide to Rxn, Act2, Tact, React and Gtplot.* University of Illinois, Urbana Illinois.
- Blowes, D.W., Reardon, E.J., Jambor, J.L., Cherry, A., 1991. The formation and potential importance of cemented layers in inactive sulphide mine tailings. *Geochim. Cosmochim. Acta* 55, 965–978.
- Boddu, V.M., Abburi, K., Talbott, J.L., Smith, E.D., Haasch, R., 2008. Removal of arsenic (III) and arsenic (V) from aqueous medium using chitosan-coated biosorbent. *Water Res.* 42 (3), 633–642.
- Bowell, R.J., 2002, The United Kingdom has thousands of abandoned metal mines. *SRK News* 34 <https://www.srkexploration.com/en/newsletter/focus-waste-geochemistry/united-kingdom-has-thousands-abandoned-metal-mines> (accessed 02 July 2018).
- Bussière, B., Benzaazoua, M., Aubertin, M. and Mbonimpa, M., 2004. A laboratory study of covers made of low-sulphide tailings to prevent acid mine drainage. *Environ. Geol.* 45, 609–622.
- Bussière, B., Aubertin, M., Mbonimpa, M., Molson, J.W. and Chapuis, R.P., 2007. Field experimental cells to evaluate the hydrogeological behaviour of oxygen barriers made of silty materials. *Can. Geotech. J.* 44, 245–265.
- Cabral, A., Racine, I., Burnotte, F., Lefebvre, G., 2000. Diffusion of oxygen through a pulp and paper residue barrier. *Can. Geotech. J.* 37, 201–217.
- Cai, M.-F., Dang, Z., Chen, Y.-W., Belzile, N., 2005. The passivation of pyrrhotite by surface coating. *Chemosphere* 61 (5), 659–667.

- Calugaru, I. L., Neculita, C.M., Genty, T., Bussière, B., Potvin, R., 2016. Performance of thermally activated dolomite for the treatment of Ni and Zn in contaminated neutral drainage. *J. Hazard. Mater.* 310, 48–55.
- Chen, Y.-W., Li, Y., Cai, M.-F., Belzile, N., Dang, Z., 2006. Preventing oxidation of iron sulfide minerals by polyethylene polyamines. *Miner. Eng.* 19 (1), 19–27.
- Cheong, Y., Hur, W., Yim, G., Ji, S., Seo, E., 2016. Evaluation of neutralization-precipitation process of acid mine drainage using a process simulator. *J. Korean Soc. Miner. Energy Resour. Eng.* 53 (1), 1–9.
- Chopard, A., Benzaazoua, M., Bouzahzah, H., Plante, B., Marison, P., 2017. A contribution to improve the calculation of the acid generating potential of mining wastes. *Chemosphere* 175, 97–107.
- Chtaini, A., Bellaloui, A., Ballivy, G., Narasiah, S., 2001. Field investigation of controlling acid mine drainage using alkaline paper mill waste. *Water Air Soil Pollut.* 125, 357–374.
- Clyde, E.J., Champagne, P., Jamieson, H.E., Gorman, C., Sourial, J., 2016. The use of a passive treatment system for the mitigation of acid mine drainage at the Williams Brothers Mine (California): pilot-scale study. *J. Clean. Prod.* 130, 116–125.
- Cravotta III, C.A., 2008. Laboratory and field evaluation of a flushable oxalic limestone drain for treatment of net-acidic drainage from a flooded anthracite mine, Pennsylvania, USA. *Appl. Geochem.* 23 (12), 3404–3422.
- Crundwell, F.K., 1988. The influence of the electronic structure of solids on the anodic dissolution and leaching of semiconducting sulphide minerals. *Hydrometallurgy* 21 (2), 155–190.
- David, C.P.C., 2003. Establishing the impact of acid mine drainage through metal bioaccumulation and taxa richness of benthic insects in a tropical Asian stream (the Philippines). *Environ. Toxicol. Chem.* 22 (12), 2952–2959.
- Demers, I., Bussière, B., Benzaazoua, M., Mbonimpa, M., Blier, A., 2008. Column test investigation on the performance of monolayer covers made of desulphurized tailings to prevent acid mine drainage. *Miner. Eng.* 21, 317–329.
- Demers, I., Mbonimpa, M., Benzaazoua, M., Bouda, M., Awoh, S., Lortie, S. and Gagnon, M., 2017. Use of acid mine drainage treatment sludge by combination with a natural soil as an oxygen barrier cover for mine waste reclamation: Laboratory column tests and intermediate scale field tests. *Miner. Eng.* 107, 43–52.

- Diao, Z., Shi, T., Wang, S., Huang, X., Zhang, T., Tang, Y., Zhang, X. and Qiu, R., 2013. Silane-based coatings on the pyrite for remediation of acid mine drainage. *Water Res.* 47, 4391–4402.
- Doye, I., Duchesne, J., 2003. Neutralisation of acid mine drainage with alkaline industrial residues: laboratory investigation using batch-leaching tests. *Appl. Geochem.* 18, 1197–1213.
- Doyle, C., 2007. Mining in the Philippines – Concerns and conflicts. Fact Finding Mission to the Philippines Report.
- Duchesne, J., Doye, I., 2005. Effectiveness of covers and liners made of red mud bauxite and/or cement kiln dust for limiting acid mine drainage. *J. Environ. Eng.* 131 (8), 1230–1235.
- Edraki, M., Golding, S.D., Baublys, K.A., Lawrence, M.G., 2005. Hydrochemistry, mineralogy and sulfur isotope geochemistry of acid mine drainage at the Mt. Morgan mine environment, Queensland, Australia. *Appl. Geochem.* 20 (4), 789–805.
- Elberling, B., Damgaard, L.R., 2001. Microscale measurements of oxygen diffusion and consumption in subaqueous sulfide tailings. *Geochim. Cosmochim. Acta* 65 (12), 1897–1905.
- Elsetinow, A.R., Borda, M.J., Schoonen, M.A.A., Strongin, D.R., 2003. Suppression of pyrite oxidation in acidic aqueous environments using lipids having two hydrophobic tails. *Adv. Environ. Res.* 7, 969–974.
- Evangelou, V.P., 1995. Pyrite oxidation and its control, CRC press, Boca Raton, FL.
- Evangelou, V.P., 1996. Oxidation proof silicate surface coating on iron sulfides. U.S. Patent No. 5,494,703.
- Evangelou, V.P., 2001. Pyrite microencapsulation technologies: Principles and potential field application. *Ecol. Eng.* 17, 165–178.
- Fan, R., Short, M.D., Zeng, S.-J., Qian, G., Li, J., Schumann, R.C., Kawashima, N., Smart, R.S.C., Gerson, A.R., 2017. The formation of silicate-stabilized passivating layers on pyrite for reduced acid rock drainage. *Environ. Sci. Technol.* 51, 11317–11325.
- Fukushi, K., Sasaki, M., Sato, T., Yanase, N., Amano, H., Ikeda, H., 2003. A natural attenuation of arsenic in drainage from an abandoned arsenic mine dump. *Appl. Geochem.* 18 (8), 1267–1278.
- Gustafsson, J.P., 2010. Visual MINTEQ Thermodynamic Databases in GWB Format. <http://vminteq.lwr.kth.se> (accessed 08 April 2017).

- Hakkou, R., Benzaazoua, M., Bussière, B., 2009. Laboratory evaluation of the use of alkaline phosphate wastes for the control of acidic mine drainage. *Mine Water Environ.* 28, 206–218.
- Hammarstrom, J.M., Sibrell, P.L. and Belkin, H.E., 2003. Characterization of limestone reacted with acid-mine drainage in a pulsed limestone bed treatment system at the Friendship Hill National Historical Site, Pennsylvania, USA. *Appl. Geochem.* 18, 1705–1721.
- Harris, D.L., Lottermoser, B.G., Duchesne, J., 2003. Ephemeral acid mine drainage at the Montalbion silver mine, north Queensland. *Aust. J. Earth Sci.* 50, 797–809.
- Herrera, P., Uchiyama, H., Igarashi, T., Asakura, K., Ochi, Y., Iyatomi, N., Nagae, S., 2007a. Treatment of acid mine drainage through a ferrite formation process in central Hokkaido, Japan: Evaluation of dissolved silica and aluminum interference in ferrite formation. *Miner. Eng.* 20 (13), 1255–1260.
- Herrera, P., Uchiyama, H., Igarashi, T., Asakura, K., Ochi, Y., Ishizuka, F., Kawada, S., 2007b. Acid mine drainage treatment through a two-step neutralization ferrite-formation process in northern Japan: Physical and chemical characterization of the sludge. *Miner. Eng.* 20 (14), 1309–1314.
- Hua, X., Li, S., 2018. Restoration and remediation of 19,000 hectare mine area in Jiangxi province (江西恢复治理矿山环境 1.9 万公顷). http://www.zrzyb.net/dizhikuangchan/20180409_113106.shtml (accessed 12 July 2018).
- Huang, X., Evangelou, V.P., 1992. Abatement of acid mine drainage by encapsulation of acid producing geologic materials. U.S. Department of the Interior, Bureau of Mines, Contact No. J0309013.
- Huminichi, D.M.C. and Rimstidt, J.D., 2009. Iron oxyhydroxide coating of pyrite for acid mine drainage control. *Appl. Geochem.* 24, 1626–1634.
- Jha, R.K.T., Satur, J., Hiroyoshi, N., Ito, M. and Tsunekawa, M., 2008. Carrier-microencapsulation using Si–catechol complex for suppressing pyrite floatability. *Miner. Eng.* 21 (12–14), 889–893.
- Jha, R.K.T., Satur, J., Hiroyoshi, N., Ito, M. and Tsunekawa, M., 2011. Suppression of floatability of pyrite in coal processing by carrier microencapsulation. *Fuel Process. Technol.* 92 (5), 1032–1036.
- Ji, M.-K., Gee, E.-D., Yun, H.-S., Lee, W.-R., Park, Y.-T., Khan, M.A., Jeon, B.-H., Choi, J., 2012. Inhibition of sulfide mineral oxidation by surface coating agents: Batch and field studies. *J. Hazard. Mater.* 229–230, 298–306.

- Jiang, C.L., Wang, X.H., Parekh, B.K., 2000. Effect of sodium oleate on inhibiting pyrite oxidation. *Int. J. Miner. Proc.* 58, 305–318.
- Johnson, D.B., 2003. Chemical and microbiological characteristics of mineral spoils and drainage waters at abandoned coal and metal mines. *Water Air Soil Pollut.* 3, 47–66.
- Johnson, D.B. and Hallberg, K.B., 2005. Acid mine drainage remediation options: a review. *Sci. Total Environ.* 338, 3–14.
- Kang, H., Park, S.-M., Jang, Y.-D., Kim, J.-J., 2008. Studies for neutralization treatment of acid mine drainage from abandoned mine. *Econ. Environ. Geol.* 41 (1), 33–45.
- Kano, K., 2000. Prevention of hazard in mining waste heap. In: *Proceedings of the Third Asia-Pacific Regional Workshop on Hazardous Waste Management in Mining Industry*. Beijing. September. 5–10.
- Kargbo, D.M., Atallah, G., Chatterjee, S., 2004. Inhibition of pyrite oxidation by a phospholipid in the presence of silicate. *Environ. Sci. Technol.* 38, 3432–3441.
- Kay, C.M., Rowe, O.F., Rocchetti, L., Coupland, K., Hallberg, K.B., Johnson, D.B., 2013. Evolution of microbial “streamer” growths in an acidic, metal-contaminated stream draining an abandoned underground copper mine. *Life* 3, 189–210.
- Kelley, B.C., Tuoniven, O.H., 1988. Microbiological oxidations of minerals in mine tailings, In: Salomons W., Förstner U. (Eds.), *Chemistry and biology of solid waste*. Springer, Berlin, Heidelberg, 33–53.
- Khummalai, N. and Boonamnuayvitaya, V., 2005. Suppression of arsenopyrite surface oxidation by sol-gel coatings. *J. Biosci. Bioeng.* 99 (3), 277–284.
- Kim, D.-H., 2009. Study on mine reclamation regimes for redeveloping closed mines of Korea. *Econ. Environ. Geol.* 42 (6), 619–626.
- Kim, J.-J., Kim, S.-J., Kim, Y.-Y., 2003. Mineralogy of evaporation residues and geochemistry of acid mine drainage in the Donghae mine area. *Econ. Environ. Geol.* 36 (2), 103–109.
- Kleinmann, R., 1982. Method of control of acid drainage from exposed pyritic materials. U.S. Patent No. 4,314,966.
- Kleinmann, R.L.P., Erickson, P.M., 1983. Control of acid mine drainage from coal refuse using anionic surfactants. U.S. Bureau of Mines, RI 8847.

- Lalvani, S.B., DeNeve, B.A., Weston, A., 1990. Passivation of pyrite due to surface treatment. *Fuel* 69, 1567–1569.
- Lan, Y., Huang, X. and Deng, B., 2002. Suppression of pyrite oxidation by iron 8-hydroxyquinoline. *Arch. Environ. Contam. Toxicol.* 43, 168–174.
- Lee, G., Bigam, J.M., Faure, G., 2002. Removal of trace metals by coprecipitation with Fe, Al and Mn from natural waters contaminated with acid mine drainage in the Ducktown Mining District, Tennessee. *Appl. Geochem.* 17 (5), 569–581.
- Li, F., 2016. Comprehensive remediation of 1,223 abandoned mines in 13th-five-year plan of Zhejiang province (浙江“十三五”全面治理 1223 个废弃矿山). http://www.zrzyb.net/dizhikuangchan/20160713_98181.shtml (accessed 12 July 2018).
- Lin, Z., 1997. Mobilization and retention of heavy metals in mill-tailings from Garpenberg sulfide mines, Sweden. *Sci. Total Environ.* 198, 13–31.
- Liu, Y., Dang, Z., Xu, Y. and Xu, T., 2013. Pyrite passivation by triethylenetetramine: An electrochemical study. *J. Anal. Methods Chem.*, 1–8.
- Liu, Y., Hu, X. and Xu, Y., 2017. PropS-SH/SiO₂ nanocomposite coatings for pyrite oxidation inhibition to control acid mine drainage at the source. *J. Hazard. Mater.* 338, 313–322.
- Lottermoser, B.G., 2003. *Mine wastes: characterization, treatment and environmental impacts.* Springer-Verlag Berlin Heidelberg, Germany.
- Lottermoser, B.G., Ashley, P.M., 2006. Mobility and retention of trace elements in hardpan-cemented cassiterite tailings, north Queensland, Australia. *Environ. Geol.* 50 (6), 835–846.
- Lyew, D., Sheppard, J.D., 1997. Effects of physical parameters of a gravel bed on the activity of sulphate-reducing bacteria in the presence of acid mine drainage. *J. Chem. Technol. Biotechnol.* 70, 223–230.
- Mackasey, W.O., 2000. *Abandoned mines in Canada. A review for Mining Watch Canada by WOM Geological Associations Inc.* Sudbury, Ontario.
- Masindi, V., 2017. Recovery of drinking water and valuable minerals from acid mine drainage using an integration of magnesite, lime, soda ash, CO₂ and reverse osmosis treatment processes. *J. Environ. Chem. Eng.* 5, 3136–3142.

- Metroke, T.L., Parkhill, R.L., Knobbe, E.T., 2001. Passivation of metal alloys using sol-gel-derived materials — a review. *Prog. Org. Coat.* 41 (4), 233–238.
- Miller, S., Rusdinar, Y., Smart, R., Andrina, J., Richards, D., 2006. Design and construction of limestone blended waste rock dumps – Lessons learned from a 10-year study at Grasberg. In: *Proceedings of 7th International conference on acid rock drainage (ICARD)*, St. Louis MO., USA, 1287–1301.
- Miller, S., Schumann, R., Smart, R., Rusdinar, Y., 2009. ARD control by limestone induced armouring and passivation of pyrite mineral surfaces. In: *Proceedings of the 8th International Conference on Acid Rock Drainage (ICARD)*, Skelleftea, Sweden, 1–11.
- Mohan, D., Pittman, C.U., 2007. Arsenic removal from water/wastewater using adsorbent – a critical review. *J. Hazard. Mater.* 142 (1–2), 1–53.
- Mollamahmutoglu, M., Yilmaz, Y., 2001. Potential use of fly ash and bentonite mixture as liner or cover at waste disposal areas. *Environ. Geol.* 40, 1316–1324.
- Molson, J.W., Aubertin, M., Bussière, B., Joanes, A-M., 2004. Simulating acid mine drainage through mine wastes constructed with capillary barrier covers. In: *Proceedings of the 5th joint IAH-CNC and CGS Groundwater Specialty Conference, 57th Canadian Geotechnical Conference*, Quebec, Canada, Session 8D, 29–36.
- Molson, J., Aubertin, M., Bussière, B., Benzaazoua, M., 2008. Geochemical transport modeling of drainage from experimental mine tailings cells covered by capillary barriers. *Appl. Geochem.* 23, 1–24.
- Moncur, M.C., Ptacek, C.J., Lindsay, M.B.J., Blowes, D.W., Jambor, J.L., 2015. Long-term mineralogical and geochemical evolution of sulfide mine tailings under a shallow water cover. *Appl. Geochem.* 57, 178–193.
- Muliwa, A.M., Leswifi, T.Y., Onyango, M.S., 2018. Performance evaluation of eggshell waste material for remediation of acid mine drainage from coal dump leachate. *Miner. Eng.* 122, 241–250.
- Mylona, E., Xenidis, A., Paspaliaris, I., 2000. Inhibition of acid generation from sulphidic wastes by the addition of small amounts of limestone. *Miner. Eng.* 13 (10–11), 1161–1175.
- National Program Support for Environment and Natural 877 Resources Management Project (NPSENRM), 2014. Project Completion Report, Annex C: Remediation of Risk, CY 2014.

- Nicholson, R.V., Gillham, R.W., Reardon, E.J., 1988. Pyrite oxidation in carbonate - buffered solutions: 1. Experimental kinetics. *Geochim. Cosmochim. Acta* 52, 1077–1085.
- Nicholson, R.V., Gillham, R.W., Reardon, E.J., 1990. Pyrite oxidation in carbonate-buffered solutions: 2. Rate control by oxide coatings. *Geochim. Cosmochim. Acta* 54, 395–402.
- Nyavor, K., Egiebor, N.O., 1995. Control of pyrite oxidation by phosphate coating. *Sci. Total Environ.* 162, 225–237.
- Olalde, M., 2016. South Africa's Toxic Legacy. <https://pulitzercenter.org/projects/south-africas-toxic-legacy> (accessed 02 July 2018).
- Ouyang, Y., Liu, Y., Zhu, R., Ge, F., Xu, T., Luo, Z. and Liang, L., 2015. Pyrite oxidation inhibition by organosilane coatings for acid mine drainage control. *Miner. Eng.* 72, 57–64.
- Parisi, D., Horneman, J., Rastogi, V., 1994. Use of bactericides to control acid mine drainage from surface operations. In: *Proceedings of the International Land Reclamation and Mine Drainage Conference*, U.S. Bureau of Mines SP 06B-94, Pittsburgh, PA, 319–325.
- Park, C.Y., Jeong, Y.J., 1999. Seasonal variation of heavy metal content in acid mine drainage from Kwangyang mine. *J. Korean Soc. Miner. Energy Resour. Eng.* 36 (1), 91–102.
- Park, I., Tabelin, C.B., Jeon, S., Li, X., Seno, K., Ito, M., Hiroyoshi, N., 2019. A review of recent strategies for acid mine drainage prevention and mine tailings recycling. *Chemosphere* 219, 588–606.
- Peppas, A., Komnitsas, K. and Halikia, I., 2000. Use of organic covers for acid mine drainage control. *Miner. Eng.* 13 (5), 563–574.
- Pérez-López, R., Cama, J., Nieto, J.M., Ayora, C., 2007. The iron-coating role on the oxidation kinetics of a pyritic sludge doped with fly ash. *Geochim. Cosmochim. Acta* 71, 1921–1934.
- Plante, B., Bussière, B., Benzaazoua, M., 2014. Lab to field scale effects on contaminated neutral drainage prediction from the Tio mine waste rocks. *J. Geochem. Explor.* 137, 37–47.
- Rao, A.V., Kulkarni, M.M., Pajonk, G.M., Amalnerkar, D.P., Seth, T., 2003. Synthesis and characterization of hydrophobic silica aerogels using trimethylethoxysilane as a co-precursor. *J. Sol-Gel Sci. Technol.* 27 (2), 103–109.
- Rao, S.R., Kuyucak, N., Sheremata, T., Leroux, M., Finch, J.A., Wheeland, K.G., 1993. Prospect of metal recovery/recycle from acid mine drainage. In: *Proceedings of the International Land*

- Reclamation and Mine Drainage Conference and the 3rd International Conference on the Abatement of Acidic Drainage, Pittsburg, PA, 223–232.
- Ribet, I., Ptacek, C.J., Blowes, D.W., Jambor, J.L., 1995. The potential for metal release by reductive dissolution of weathered mine tailings. *J. Contam. Hydrol.* 17, 239–273.
- Rimstidt, J.D. and Vaughan, D.J., 2003. Pyrite oxidation: a state-of-the-art assessment of the reaction mechanism. *Geochim. Cosmochim. Acta* 67 (5), 873–880.
- Rodríguez-Jordá, M.P., Garrido, F., García-González, M.T., 2012. Effect of the addition of industrial by-products on Cu, Zn, Pb and As leachability in a mine sediment. *J. Hazard. Mater.* 213–214, 46–54.
- Ryu, C.S., Kim, Y.H., Kim, J.J., 2014. Evaluation of purification efficiency of passive treatment systems for acid mine drainage and characterization of precipitates in Ilwal coal mine. *J. Miner. Soc. Korea* 27 (2), 97–105.
- Sasaki, K., Tsunekawa, M., Ohtsuka, T., Konno, H., 1998. The role of sulfur-oxidizing bacteria *Thiobacillus thiooxidans* in pyrite weathering. *Colloids Surf. A* 133, 269–278.
- Satur, J., Hiroyoshi, N., Tsunekawa, M., Ito, M. and Okamoto, H., 2007. Carrier-microencapsulation for preventing pyrite oxidation. *Int. J. Miner. Eng.* 83 (3–4), 116–124.
- Schmitz, D., Anlauf, R., Rehrmann, P., 2013. Effect of air content on the oxygen diffusion coefficient of growing media. *Am. J. Plant Sci.* 4, 955–963.
- Shu, X., Dang, Z., Zhang, Q., Yi, X., Lu, G., Guo, C., Yang, C., 2013. Passivation of metal-sulfide tailings by covalent coating. *Miner. Eng.* 42, 36–42.
- Skousen, J., 1997. Overview of passive systems for treating acid mine drainage. *Green Lands* 27, 34–43.
- Smart, R.S.C., Miller, S.D., Stewart, W.S., Rusdinar, Y., Schumann, R.E., Kawashima, N., Li, J., 2010. In situ calcite formation in limestone-saturated water leaching of acid rock waste. *Sci. Total Environ.* 408 (16), 3392–3402.
- Soares, A.B., Ubaldo, M.O., Souza, V.P., Soares, P.S.M., Barbosa, M.C., Mendonca, R.M.G., 2009. Design of a dry cover pilot test for acid mine drainage abatement in southern Brazil. I: Materials characterization and numerical modeling. *Mine Water Environ.* 28, 219–231.
- Soares, A.B., Possa, M.V., Souza, V.P., Soares, P.S.M., Barbosa, M.C., Ubaldo, M.O., Bertolino, A.V.F.A., Borma, L.S., 2010. Design of a dry cover pilot test for acid mine drainage abatement in

- southern Brazil, Part II: Pilot unit construction and initial monitoring. *Mine Water Environ.* 29, 277–284.
- Stumm, W. and Lee, G.F., 1961. Oxygenation of ferrous iron. *Ind. Eng. Chem.* 52, 143–146.
- Tabelin, C.B., Corpuz, R., Veerawattananun, S., Ito, M., Hiroyoshi, N., Igarashi, T., 2016. Formation of schwertmannite-like and scorodite-like coatings on pyrite and its implications in acid mine drainage control. In: *Proceedings of the XXVIII International Mineral Processing Congress (IMPC 2016)*, 101-112, Quebec City, Canada.
- Tabelin, C.B., Veerawattananun, S., Ito, M., Hiroyoshi, N. and Igarashi, T., 2017. Pyrite oxidation in the presence of hematite and alumina: I. Batch leaching experiments and kinetics modeling calculations. *Sci. Total Environ.* 580, 687–698.
- Tabelin, C.B., Igarashi, T., Villacorte-Tabelin, M., Park, I., Opiso, E.M., Ito, M., Hiroyoshi, N., 2018. Arsenic, selenium, boron, lead, cadmium, copper, and zinc in naturally contaminated rocks: A review of their sources, modes of enrichment, mechanisms of release, and mitigation strategies. *Sci. Total Environ.* 645, 1522–1553.
- Tabelin, C.B., Igarashi, T., Villacorte-Tabelin, M., Park, I., Opiso, E.M., Ito, M., Hiroyoshi, N., 2018a. Arsenic, selenium, boron, lead, cadmium, copper, and zinc in naturally contaminated rocks: A review of their sources, modes of enrichment, mechanisms of release, and mitigation strategies. *Sci. Total Environ.* 645, 1522–1553.
- Tasse, N., Germain, D., Dufour, C., Tremblay, R., 1997. Hard-pan formation in the Canadian Malartic mine tailings: Implication for the reclamation of the abandoned impoundment. In: *Proceedings of 4th International conference on acid rock drainage*. Vancouver, B.C, Canada, 1797–1812.
- Taylor, J., Pape, S. and Murphy, N., 2005. A summary of passive and active treatment technologies for acid and metalliferous drainage (AMD). In: *5th Australian workshop on acid mine drainage*, Fremantle, Australia.
- The International Network for Acid Prevention (INAP), 2009. *Global Acid Rock Drainage Guide (GARD Guide)*. <http://www.gardguide.com/>.
- Trumm, D., 2010. Selection of active and passive treatment systems for AMD—flow charts for New Zealand conditions. *N. Z. J. Geol. Geophys.* 53, 195–210.

- Tutu, H., McCarthy, T.S., Cukrowska, E., 2008. The chemical characteristics of acid mine drainage with particular reference to sources, distribution and remediation: The Witwatersrand Basin, South Africa as a case study. *Appl. Geochem.* 23, 3666–3684.
- Unger, C., Lechner, A., Glenn, V., Edraki, M. and Mulligan, D.R., 2012. Mapping and prioritizing rehabilitation of abandoned mines in Australia. *Life-of-Mine Conference 2012*, Brisbane, Australia, 1–14.
- Ustamehmetoğlu, B., Sezer, E., Kızılcın, N., Yazıcı, P., Tayyar, Ş., Saraç, A.S., 2013. Inhibition of pyrite corrosion and photocorrosion by MEKF-R modified carbazoles. *Prog. Org. Coat.* 76, 533–540.
- Vandiviere, M.M., Evangelou, V.P., 1998. Comparative testing between conventional and microencapsulation approaches in controlling pyrite oxidation. *J. Geochem. Explor.* 64, 161–176.
- Vigneault, B., Campbell, P.G.C., Tessier, A., de Vitre, R., 2001. Geochemical changes in sulfidic mine tailings stored under a shallow water cover. *Water Res.* 35 (4), 1066–1076.
- White III, W.W., Lapakko, K.A., Cox, R.L., 1999. Static-test methods most commonly used to predict acid mine drainage: Practical guidelines for use and interpretation. In: Plumlee, G.S., Logsdon, M.J. (Eds.), *The Environmental Geochemistry of Mineral Deposits. Part A: Processes Techniques and Health Issues*. Society of Economic Geologists, Inc., pp. 325–338.
- Wolkersdorfer, C. and Bowell, R. (Eds.), 2005. Contemporary reviews of mine water studies in Europe, part 2. *Mine Water Environ.* 24, 2–37.
- Wu, P., Tang, C., Liu, C., Zhu, L., Pei, T., Feng, L., 2009. Geochemical distribution and removal of As, Fe, Mn and Al in a surface water system affected by acid mine drainage at a coalfield in Southwestern China. *Environ. Geol.* 57, 1457–1467.
- Xenidis, A., Mylona, E., Paspaliaris, I., 2002. Potential use of lignite fly ash for the control of acid generation from sulphidic wastes. *Waste Manage.* 22, 631–641.
- Yamaguchi, K., Tomiyama, S., Metugi, H., Ii, H., Ueda, A., 2015. Flow and geochemical modeling of drainage from Tomitaka mine, Miyazaki, Japan. *J. Environ. Sci.* 36, 130–143.
- Yang, Y., Li, Y., Sun, Q.-Y., 2014. Archaeal and bacterial communities in acid mine drainage from metal-rich abandoned tailings ponds, Tongling, China. *Trans. Nonferrous Met. Soc. China* 24, 3332–3342.
- Yeheyis, M.B., Shang, J.Q., Yanful, E.K., 2009. Long-term evaluation of coal fly ash and mine tailings co-placement: A site-specific study. *J. Environ. Manage.* 91, 237–244.

- You, G.-X., Yu, C.-C., Lu, Y., Dang, Z., 2013. Evaluation of the protective effect of polysiloxane coating on pyrite with electrochemical techniques. *Electrochim. Acta* 93, 65–71.
- Yuniati, M.D., Kitagawa, K., Hirajima, T., Miki, H., Okibe, N. and Sasaki, K., 2015. Suppression of pyrite oxidation in acid mine drainage by carrier microencapsulation using liquid product of hydrothermal treatment of low-rank coal, and electrochemical behavior of resultant encapsulating coatings. *Hydrometallurgy* 158, 83–93.
- Zeng, S., Li, J., Schumann, R., Smart, R., 2013. Effect of pH and dissolved silicate on the formation of surface passivation layers for reducing pyrite oxidation. *Comput. Water Energy Environ. Eng.* 2, 50–55.
- Zhang, M., Wang, H., 2017. Utilization of bactericide technology for pollution control of acidic coal mine waste. *Adv. Eng. Res.* 129, 667–670.
- Zhang, X., Borda, M.J., Schoonen, M.A.A., Strongin, D.R., 2003a. Adsorption of phospholipids on pyrite and their effect on surface oxidation. *Langmuir* 19, 8787–8792.
- Zhang, X., Borda, M.J., Schoonen, M.A.A., Strongin, D.R., 2003b. Pyrite oxidation inhibition by a cross-linked lipid coating. *Geochem. Trans.* 4 (2), 8–11.
- Zhang, Y.L. and Evangelou, V.P., 1998. Formation of ferric hydroxide-silica coatings on pyrite and its oxidation behavior. *Soil Sci.* 163 (1), 53–62.
- Zhao, F., Cong, Z., Sun, H., Ren, D., 2007. The geochemistry of rare earth elements (REE) in acid mine drainage from the Sitai coal mine, Shanxi Province, North China. *Int. J. Coal Geol.* 70, 184–192.
- Zhao, L.Y.L., McCullough, C.D. and Lund, M.A., 2009. Mine voids management strategy (I): Pit lake resources of the Collie basin. MiWER/Centre for Ecosystem Management Report 2009-10 Edith Cowan University, Perth, Australia.

CHAPTER 2 – SUPPRESSION OF THE RELEASE OF ARSENIC FROM ARSENOPYRITE BY CARRIER-MICROENCAPSULATION USING TITANIUM-CATECHOLATE COMPLEX

2.1 Introduction

In the first CME study of Satur et al. (2007), titanium (Ti)-catecholate complex was synthesized by mixing TiO₂ minerals (i.e., rutile (α -TiO₂) and anatase (β -TiO₂)) and pyrocatechol (1,2-dihydroxybenzene, C₆H₄(OH)₂). These authors showed that catechol extracted Ti-ions directly from TiO₂ but extraction efficiency was very low (i.e., < 0.3%). Although CME was successfully applied to suppress pyrite oxidation in this previous study, the mechanism(s) involved remain unclear because the authors mixed TiO₂ and catechol together with pyrite. In other words, the suppression of pyrite oxidation by Ti-catecholate complex was masked by the effects of TiO₂ and “free” catechol. Mineral oxides attached to pyrite could directly minimize its oxidation by protecting cathodic sites from oxidants like dissolved O₂ (DO) and Fe³⁺ (Tabelin et al., 2017a, 2017b). Likewise, free catechol might indirectly suppress pyrite oxidation by consuming DO and forming stable complexes with Fe³⁺ (Pracht et al., 2001; Schweigert et al., 2001). In addition, the electrochemical properties of free catechol and Ti-catecholate complex was not elucidated in detail, so the mechanism involved in Ti-catecholate complex formation and oxidative decomposition remains poorly understood.

In this chapter, the effects of pH and molar ratio on the formation of Ti-catecholate complex were investigated, and a simple and more efficient method to synthesize it for CME treatment was introduced. Electrochemical studies (i.e., cyclic voltammetry and chronoamperometry) were carried out to understand the electrochemical behavior of synthesized Ti-catecholate complex and identify the mechanism(s) involved in its oxidative decomposition as well as in its ability to passivate arsenopyrite (FeAsS). Finally, the synthesized Ti-catecholate complex was used to treat arsenopyrite, the most common arsenic (As)-bearing sulfide mineral closely associated with gold and copper mineralization (Corkhill and Vaughan, 2009; Coussy et al., 2011; Islam et al., 2013; Murciego et al., 2011; Salzsauler et al., 2005). Arsenopyrite was selected because not only is it common in mine wastes but its weathering also leads to the release of toxic arsenic into the environment when exposed to atmospheric conditions either naturally or via anthropogenic activities like mining, mineral processing, metallurgy, and underground space developments (Johnson and Hallberg, 2005; Tabelin et al., 2012). Arsenic is a strictly regulated due to its toxicity at high concentrations and its potential to cause numerous diseases like hyperpigmentation, keratosis, anemia, neuropathy and several types of cancers even at minute amounts (Boddu et al., 2008; Mohan and Pittman, 2007).

2.2 Materials and methods

2.2.1 Synthesis of Ti-catecholate complex

In our preparation method to synthesize Ti-catecholate complex, Ti^{4+} ions and catechol molecules were mixed directly at very acidic condition ($\text{pH} < 2$). Several studies have already reported that Ti-oxides (i.e., rutile, anatase and ilmenite) dissolve in concentrated sulfuric acid solutions (Agatzini-Leonardou et al., 2008; He et al., 2016; Meng et al., 2016), so we skipped the dissolution part in this study. Instead, Ti-catecholate complex was prepared by mixing reagent grade pyrocatechol and in place of TiO_2 dissolved in concentrated H_2SO_4 , we used high purity (99.9%) titanium solution (Ti^{4+} in 1M H_2SO_4) (Wako Pure Chemical Industries, Ltd., Japan) to avoid the effects of contaminants like Si and Fe that are ubiquitous in TiO_2 ores.

Our preliminary experiments showed that Ti-catecholate complex was only synthesized when the very acidic Ti^{4+} and catechol mixture was rapidly neutralized between pH 5 and 12. If neutralization was more gradual (e.g., titration), Ti-catecholate complex was not formed because Ti^{4+} ions were rapidly precipitated to TiO_2 . In the succeeding sections, all Ti-catechol solutions were prepared by “rapid neutralization”.

2.2.2 Ti-catecholate complex formation with various stoichiometric molar ratios of Ti^{4+} to catechol

Catechol is a strong chelating agent that coordinates with various metal ions (e.g., Ti^{4+} , Fe^{3+} , Cu^{2+} , and etc.) to form several metal-catecholate complexes (i.e., mono-, bis- and tris-catecholate) (Borgias et al., 1984; Sever and Wilker, 2004). To evaluate the composition of Ti-catecholate complex(es) formed during synthesis, 1 mM of Ti^{4+} solution was mixed with varying stoichiometric molar ratios of Ti^{4+} to catechol (1:0–1:5) at 25°C and 200 rpm. After this, the pH of each solution was rapidly adjusted to 9, transferred to a volumetric flask to adjust the precise concentration by adding small amounts of DI water. The solutions were then filtered and analyzed by an inductively coupled plasma atomic emission spectrometer (ICP-AES, ICPE 9820, Shimadzu Corporation, Japan; margin of error = $\pm 2\%$).

2.2.3 Identification of Ti-catecholate complex stability

Solutions containing Ti^{4+} only (1 mM Ti^{4+}) and 1:3 molar ratio of Ti^{4+} to catechol (1 mM Ti^{4+} and 3 mM catechol) were prepared at pH values ranging from 0 to 12 to evaluate the formation and

stability of Ti-catecholate complex. After rapid neutralization and equilibration, the pH were measured and filtrates were collected by filtration through 0.2 μm syringe-driven filters (Sartorius AG, Germany) to remove precipitates and polymerized organic molecules prior to ICP-AES analyses.

2.2.4 Ultraviolet-visible light spectrophotometric measurements

Ultraviolet-visible light (UV-vis) spectrophotometric measurements (UV-2500 PC, Shimadzu Corporation, Japan) were conducted to identify Ti-catecholate complex(es) formed under various conditions. Catechol only and Ti-catechol solutions adjusted to various pH (1, 3, 6 and 9) were measured in the range of 250–550 nm using a single-crystal quartz cell.

2.2.5 Electrochemical studies for the insights into Ti-catecholate complex decomposition

Cyclic voltammetry (CV) measurements were performed using SI 1280B electrochemical measurement unit (Solartron Instruments, UK) with a conventional three-electrode system (Figure 2-1). Platinum (Pt) electrode, platinum wire and Ag/AgCl electrode filled with 3.3 M NaCl were used as working, counter and reference electrodes, respectively. Three types of solutions were measured by CV: 6 mM catechol at pH 5, 6 mM catechol at pH 9 and Ti-catechol solution (2 mM Ti^{4+} and 6 mM catechol) at pH 9, all of which were prepared in 0.1 M Na_2SO_4 as supporting electrolyte. All experiments were carried out at 25°C under nitrogen atmosphere. The CV measurements started after equilibration at the open circuit potential (OCP), and the sweep direction was towards more positive potentials first (i.e., anodic direction) at a scan rate of 5 mV/s for 5 cycles. In addition, CV measurements of Ti-catechol solution (pH 9) at various scan rates of 1, 5 and 30 mV/s were carried out.

Chronoamperometry was performed to identify the products formed when Ti-catecholate complex is anodically decomposed. In this experiment, a similar setup as the CV measurements was used but with magnetic stirring at 200 rpm. The Ti-catecholate complex solution was first equilibrated at the OCP, and then anodically polarized at +1.0 V vs. SHE for 3 h. After this, the Pt working electrode was analyzed by scanning electron microscopy with energy dispersive X-ray spectroscopy (SEM-EDX, SSX-550, Shimadzu Corporation, Japan) to determine the oxidation products deposited on it.

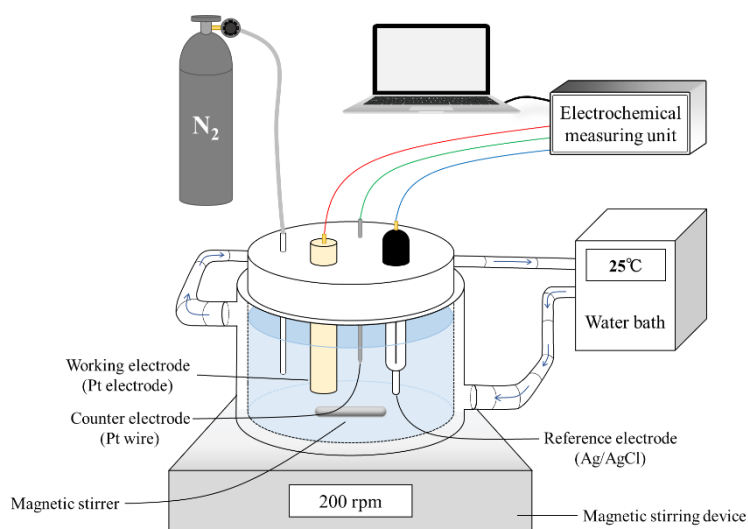


Figure 2-1. The schematic diagram of the setup for electrochemical studies.

2.2.6 Characterization of arsenopyrite sample

The arsenopyrite sample used in this study was obtained from Toroku Mine, Miyazaki, Japan. It was crushed by a jaw crusher (BB 51, Retsch Inc., Germany), ground by a disk mill (RS 100, Retsch Inc., Germany) and screened to obtain a size fraction of 106–150 μm in diameter. For its mineralogical characterization, the sample was further ground to $<50 \mu\text{m}$ and analyzed by X-ray powder diffraction (XRD, MultiFlex, Rigaku Corporation, Japan) under the following conditions: radiation, Cu $K\alpha$, 40°kV, 40°mA; scan speed, 2 deg/min; angle range, 20–70°/2 θ . The XRD pattern of arsenopyrite sample shows that it is mainly composed of arsenopyrite with pyrite and quartz as minor minerals (Figure 2-2).

The chemical composition of the sample was determined by wet method, which involves the dissolution of 100 mg of sample with 5 ml of 12 M HCl and 3 ml of 16 M HNO₃ (Wako Pure Chemical Industries, Ltd., Japan) using microwave-assisted acid digestion (Ethos, Milestone Inc., USA) and analyses of the leachate by ICP-AES. The chemical composition of the sample is 32.6, 30.9 and 20.1% of Fe, As and S, respectively, and these values are equivalent to ca. 67% of arsenopyrite, 13% of pyrite and 15% of quartz (Table 2-1).

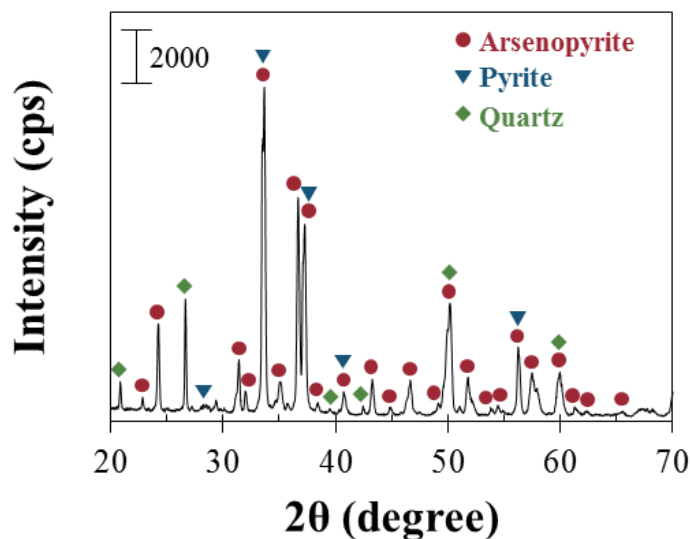


Figure 2-2. Mineralogical composition of the arsenopyrite sample.

Table 2-1. Chemical composition of the arsenopyrite sample.

Elements	Fe	As	S	Na	Mg	Cu	Al	Others
wt. %	32.6	30.9	20.1	0.5	0.4	0.3	0.1	15.1

2.2.7 Batch leaching experiments

Three types of solutions were used as leachants in the batch leaching experiments: deionized (DI) water (18 MΩ·cm, Milli-Q® Integral Purification System, Merck Millipore, USA) (control), catechol (15 mM catechol), and synthesized Ti-catecholate complex (5 mM Ti⁴⁺ and 15 mM catechol), all of which were adjusted to pH 9 before mixing them with washed arsenopyrite. The washing technique used to remove any oxidized layer formed on arsenopyrite during sample preparation was based on the method developed by McKibben et al. (2008). This method involves ultrasonic desliming in methanol, washing with 1.8 M HNO₃, rinsing with DI water, dewatering with acetone, and drying in a vacuum desiccator.

For the leaching experiments, 1 g of arsenopyrite and 10 ml of prepared leachant were put in a 50 ml Erlenmeyer flask and shaken in a constant temperature water bath (25 °C) at 120 strokes/min under oxic conditions for up to 25 days. All leaching experiments were done in triplicates to ascertain that differences observed were statistically significant. At pre-designated time intervals, samples were collected, and their pH and oxidation-reduction potential (Eh) were measured. The leachates were collected by filtration through 0.2 μm syringe-driven membrane filters, and immediately analyzed using ICP-AES to measure the concentrations of As and Ti. Meanwhile, the

residues were thoroughly washed with DI water and vacuum-dried at 40°C for 24 h. After drying, the residues were analyzed by SEM-EDX to observe the surface of leached arsenopyrite. In addition, diffuse reflectance infrared Fourier transform spectroscopy (DRIFTS, FT/IR-6200HFV with DR PR0410-M attachment, Jasco Analytical Instruments, Japan) was used to characterize changes in the surface of samples before and after leaching under the following conditions: 1000 scans at a resolution of 4 cm⁻¹ and in the range of 400–4000 cm⁻¹.

2.2.8 Chronoamperometry to identify the suppressive effects of coatings on arsenopyrite oxidation

The working electrode was prepared using arsenopyrite sample obtained from Yaogangxian mine, Hunan, Chania. It was cut using a diamond cutter to collect small size of crystal, connected to a copper wire with silver conducting paste (DOTITE, Fujikura Kasei Co., Ltd., Japan). After dried, it was fixed inside a plastic holder with Technovit® non-conductive resin (Heraeus Kulzer GmbH, Germany). To expose mineral surface, the electrode was polished with a series of silicon carbide papers (#200, #600, #1000 and #1500) and alumina (Al₂O₃) pastes (5 and 1 μm). After this, the polished electrode was cleaned using ultrasonicator (W-113, Honda Electronics Co., Ltd., Japan) for 5 min to remove residual Al₂O₃ particles attached on it, washed with DI water and then used for experiments.

Chronoamperometry, an electrochemical technique that applies a fixed potential to the working electrode and measures electron transfer between working and counter electrodes, was conducted to investigate anodic and cathodic half-cell reactions of arsenopyrite oxidation. Before measurements, arsenopyrite electrode was pretreated in DI water (control) and solutions containing either catechol or Ti-catecholate complex at an applied potential of +0.6 V vs. SHE for 1 h to create distinct oxidation products on it. After this, electrode was thoroughly washed with DI water, dried under ambient conditions for 1 h, and used for chronoamperometric measurements. The treated working electrode was first equilibrated at the OCP in 0.1 M Na₂SO₄ solution, and then polarized at 0.0 V vs. SHE for cathodic polarization and at +0.8 V vs. SHE for anodic polarization.

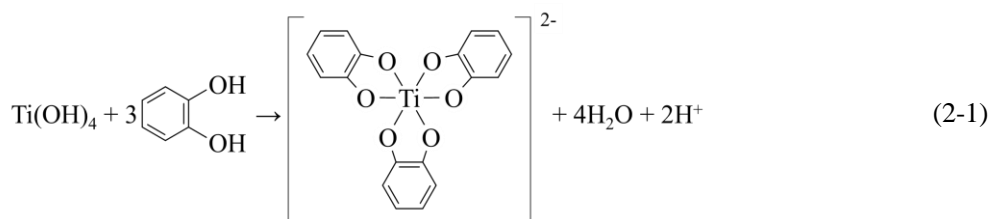
2.3 Results and discussion

2.3.1 Evaluation and characterization of Ti-catecholate complex

The effects of pH and solution composition on Ti-catecholate complex formation and stability are illustrated in Figure 2-3. In the absence of catechol, Ti⁴⁺ ions remained dissolved in solution under strongly acidic conditions (less than pH 2.0) (Figure 2-3a). At pH values higher than 3.5, whitish

colored particulates were observed and the concentration of Ti^{4+} ions decreased below the detection limit of ICP-AES (0.001 mg/L), which could be attributed to precipitation of Ti^{4+} as titanium oxide (TiO_2). This deduction is supported by thermodynamic considerations as illustrated by the equilibrium log activity-pH diagram of $Ti(OH)_4$ at 25°C (Figure 2-2b), which showed that the stability of Ti^{4+} as the hydrolyzed $Ti(OH)_4$ ion decreases with pH from 0 to 4. With catechol, however, the solubility of Ti^{4+} ion dramatically increased and the plot exhibited three distinct regions (Figure 2-3a). Regions I and II have similar trends with those of the Ti^{4+} only solution, indicating that Ti^{4+} ions in Region I exist because of the very acidic pH while the rapid Ti^{4+} concentration decrease in Region II was due primarily to the precipitation of TiO_2 . In Region III, Ti^{4+} concentration started increasing after pH 3.5 coincident with the change in color of solution from transparent to light orange, both of which are strong indicators of Ti-catecholate complex formation (Borgias et al., 1984). Over 80% of Ti^{4+} ion remained in aqueous phase above pH 5.5 (Region III), indicating that most of it was complexed with catechol because Ti^{4+} ion alone cannot exist in solution at this pH without any complexation reaction (Figures 2-3a and b).

To identify the composition of synthesized Ti-catecholate complex, solutions of Ti^{4+} and catechol with various molar ratios at pH 9 were investigated. As shown in Figure 2-3c, Ti^{4+} concentration increased at higher molar ratios of catechol to Ti^{4+} until the catechol/ Ti^{4+} ratio reached 3. These results fitted well with the theoretical curve of Ti^{4+} ion coordinated with three catechol molecules in the tris-catecholate configuration, suggesting that the synthesized Ti-catecholate complex was most likely $[Ti(cat)_3]^{2-}$. The complexation reaction of Ti^{4+} and catechol could be explained as follows:



This deduction is also supported by UV-vis spectrophotometric measurements of “free” catechol and Ti-catechol solutions at pH 1, 3, 6 and 9 (Figure 2-3d). Solutions of Ti^{4+} and catechol at pH 1 and 3 showed only one absorption peak at 274 nm, but at pH 6 and 9, a new peak appeared at around 382 nm. The absorption peak at 274 nm could be attributed to catechol as suggested by the UV-vis spectra of “free” catechol under various pH conditions (Figure 2-3d) while the broad absorption band between 375–389 nm is assigned to the Ti(IV) tris-catecholate complex consistent with the results of other authors (Borgias et al., 1984; Sever and Wilker, 2004). It is also noteworthy that the $[Ti(cat)_3]^{2-}$ absorption band was only apparent at pH 6 and 9, which is in strong agreement with the results shown in Figure 2-3a.

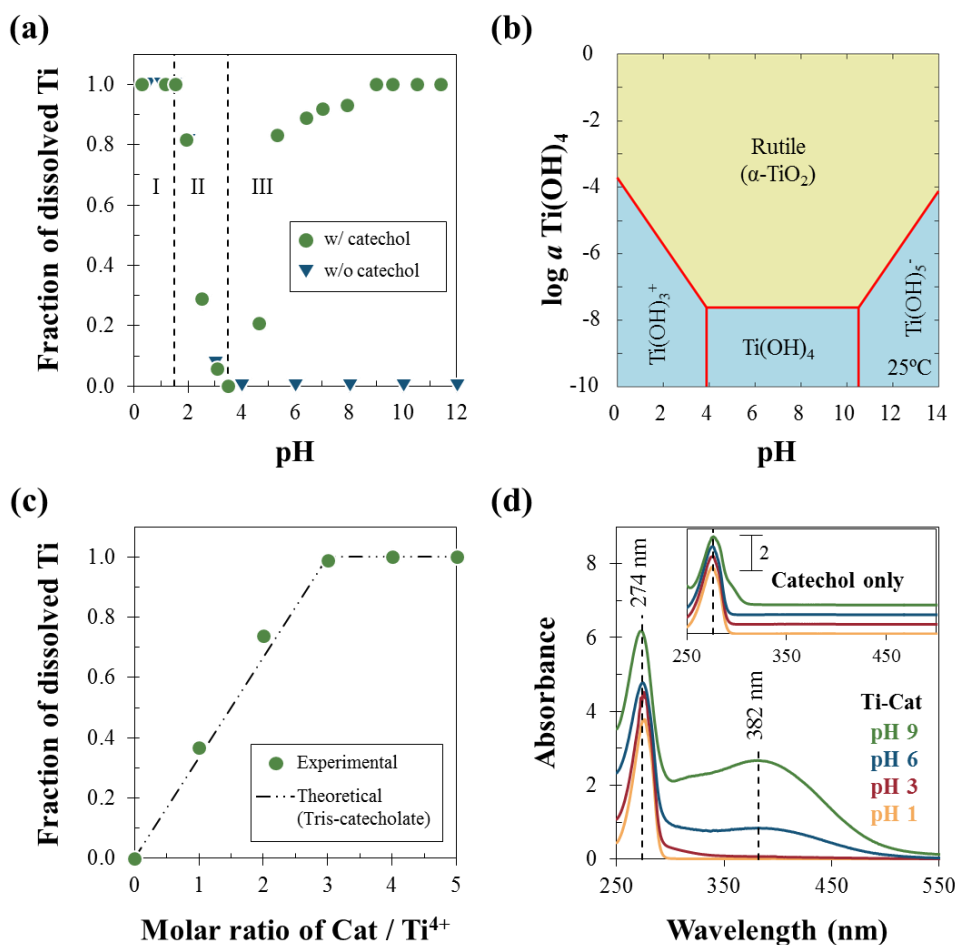


Figure 2-3. Properties of synthesized Ti-catecholate complex: (a) Ti^{4+} ion stability with pH in the presence and absence of catechol, (b) Log a – pH predominance diagram of Ti(OH)_4 at 25 °C and 1.013 bar created using the Geochemist’s Workbench® with MINTEQA2 database (Bethke, 1992; Gustafsson, 2010), (c) Ti^{4+} ion stability as a function of molar ratio of catechol to Ti^{4+} , (d) UV-vis spectra of “free” catechol and Ti-catechol solutions at pH 1, 3, 6 and 9.

2.3.2 Mechanism of Ti-catecholate complex decomposition and coating formation

Cyclic voltammetry (CV), a type of potentiodynamic electrochemical technique that provides insights into the redox reactions of compounds in solutions, was carried out to understand how “free” catechol and Ti-catecholate complex decompose under conditions that roughly simulate those existing on the surface of arsenopyrite during oxidation. Cyclic voltammogram of catechol at pH 5 (Figure 2-4a-1) showed an anodic peak at 770 mV vs. SHE (A_1) and a cathodic peak at 500 mV (C_1), which are consistent with the well documented reversible redox reaction of this organic compound (Danilewicz, 2012; Schweigert et al., 2001; Yang et al., 2014). Catechol is oxidized to quinone

(1,2-Benzoquinone) during the anodic sweep at 770 mV and is reduced back to catechol in the succeeding cathodic sweep at 500 mV (Eq. (2-2)). In contrast, the voltammogram of catechol at pH 9 (Figure 2-4a-2) showed two anodic peaks at 780 (A₁') and 260 mV (A₂') but only one cathodic peak at 500 mV (C₁'). The peaks at A₁' and C₁' were similar to that of catechol at pH 5 while the additional anodic peak at ca. 260 mV (A₂') could be attributed to oxidation of semi-quinone (Eq. (2-3)) formed during solution preparation. The strong presence of semi-quinone at pH 9 could be explained by the following reasons: (1) faster oxidation rate of catechol to semi-quinone under alkaline conditions by O₂ (Wright and Mason, 1946), and (2) greater stability of semi-quinone because of its lower one-electron reduction potential at higher pH (Yang et al., 2014).



A new anodic peak at ca. 680 mV (A₁'') appeared in the cyclic voltammogram of Ti-catecholate complex (Figure 2-4a-3) indicating that the synthesized Ti-catecholate complex, [Ti(cat)₃]²⁻, could undergo anodic decomposition. The cathodic peak observed at 440 mV (C₁'') was most likely due to the reduction of quinone to catechol as discussed earlier. In the second cycle (Figure 2-4a-3), however, the anodic peak decreased and shifted towards higher potentials compared with that of the first cycle. Succeeding cycles (i.e., 3rd and 4th) also showed continuous shift and decrease of the anodic peak until it virtually disappeared on the fifth cycle. This gradual decrease of the anodic peak could be attributed to the decreasing amount of Ti-catecholate complex due to its oxidative decomposition near the surface of working electrode, which was not regenerated from oxidation products in the succeeding cathodic sweep. This means that the oxidative decomposition of Ti-catecholate complex is irreversible. Furthermore, shifting of the anodic peak may suggest that surface of the platinum electrode is gradually being covered by oxidation products.

Some metal tris-catecholate complexes like those of Mn(IV) and Fe(III) have been reported to decompose sequentially (Boles, 2014), so to determine whether this is also the case for the synthesized Ti-catecholate complex, CV measurements at several scan rates were conducted to change the extent of oxidation-reduction reactions. Despite the various scan rates (1 to 30 mV/s), however, only one anodic peak was observed (Figure 2-4b), indicating that the oxidative decomposition of Ti-catecholate complex occurred via a one-step process and not sequentially. Satur et al. (2007) proposed that the one-step oxidation of Ti-catecholate complex occur via simultaneous

oxidation of the three catechol molecules coordinated with Ti^{4+} , which would be precipitated as Ti-hydroxide/oxide because of its very low solubility at $\text{pH} > 4$. If their hypothesis is correct, then the product after oxidation would be composed almost entirely of Ti-hydroxide/oxide. To verify this, chronoamperometry was carried out at 1.0 V vs. SHE for 3 h to generate enough oxidation products on the Pt electrode for SEM-EDX analysis. As illustrated in Figure 2-5, there were two distinct materials observed in the coating formed on Pt electrode after chronoamperometry: (1) a high carbon-containing substance (Ti–O–C), and (2) a high titanium and oxygen-containing material (Ti–O). These materials are definitely oxidation products of Ti-catecholate complex decomposition because they were not observed when the same experiment was done without applying any potential (Figure 2-6). Based on these results, decomposition of Ti-catecholate complex is much more complicated than the earlier mechanism proposed by Satur et al. (2007).

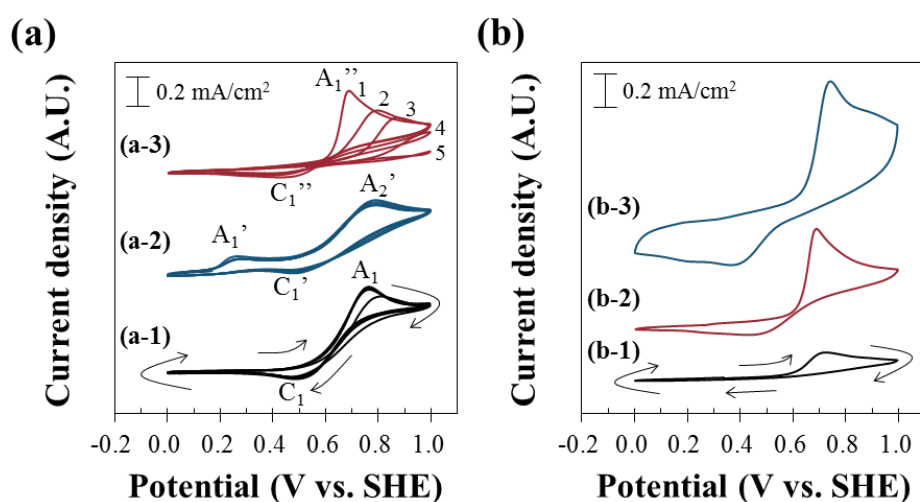


Figure 2-4. Cyclic voltammograms of (a) catechol only and Ti-catechol solution at a scan rate of 5 mV/s, (a-1) catechol at pH 5, (a-2) catechol at pH 9, (a-3) Ti-catechol at pH 9, and (b) Ti-catechol solution at pH 9 with various scan rates (1 mV/s (b-1), 5 mV/s (b-2), and 30 mV/s (b-3)). Note that arrows denote the sweep direction.

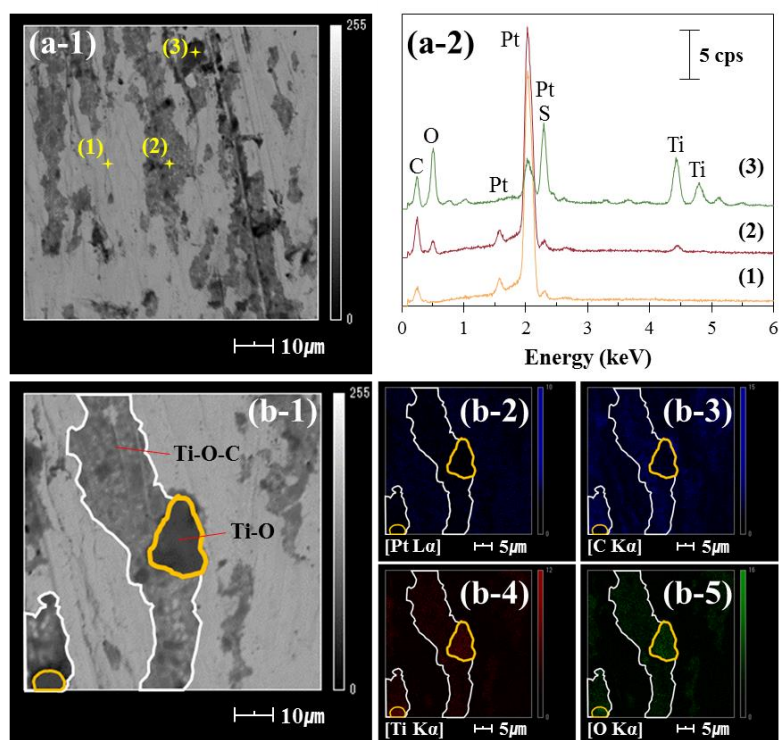


Figure 2-5. SEM-EDX analysis of Pt electrode after chronoamperometry at 1.0 V vs. SHE for 3h: (a-1) SEM photomicrograph and (a-2) energy dispersive X-ray spectra of several points, (b-1) SEM photomicrograph and the corresponding elemental maps of Pt (b-2), C (b-3), Ti (b-4), and O (b-5).

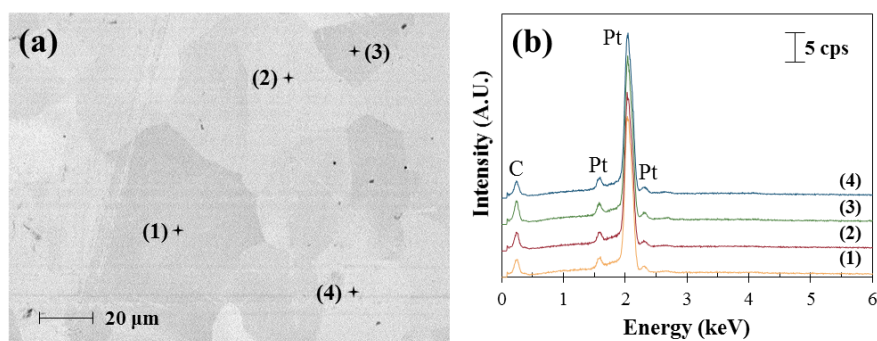


Figure 2-6. SEM-EDX analysis of Pt electrode after immersion in Ti-catechol solution for 3h: (a) SEM photomicrograph and (b) energy dispersive X-ray spectra of several points.

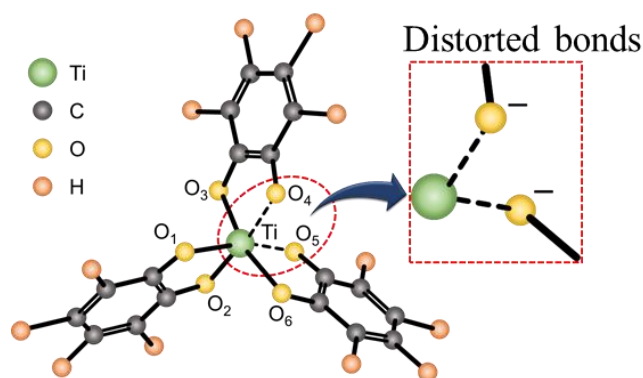
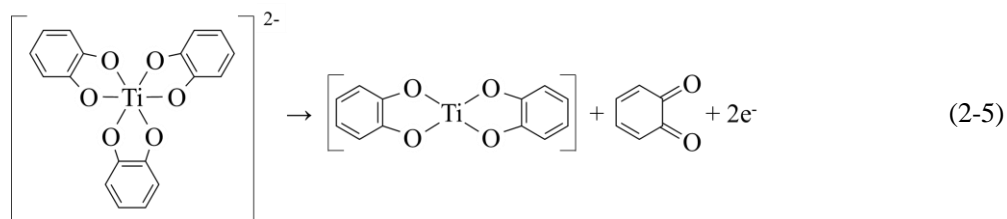
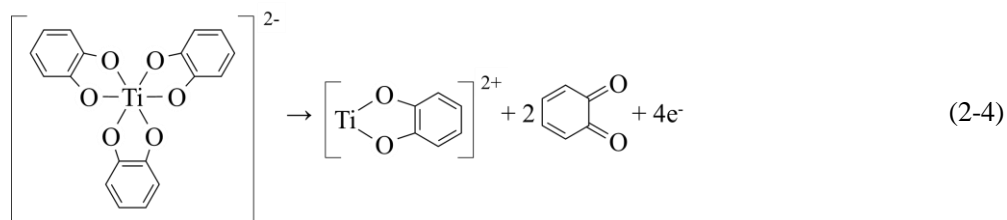


Figure 2-7. Molecular structure of Ti(IV) tris-catecholate complex.

In the structure of Ti(IV) tris-catecholate complex (Figure 2-7), one catechol molecule is “normally” coordinated with the central Ti^{4+} ion while the remaining two molecules are coordinated with distortions because of unpaired electrons in two oxygen atoms (O_4 and O_5) (Borgias et al., 1984). These oxygen atoms, O_4 and O_5 , are relatively more reactive than the others, so during anodic decomposition, Ti-O_4 and/or Ti-O_5 bonds are most probably attacked first and dislodged, resulting in the formation of Ti(IV) mono- and/or bis-catecholate complex (Eqs. (2-4) and (2-5)). Mono- and bis-catecholate complexes have been reported for Mn(IV) and Fe(III) but not for Ti(IV), which could indicate that $[\text{Ti}(\text{cat})]^{2+}$ and/or $[\text{Ti}(\text{cat})_2]$ complex(es) are very unstable (Boles, 2014; Sever and Wilker, 2004). Another possible explanation is the formation of more stable polymerized metal-organic molecule by partially oxidized Ti-catecholate complexes. In a recent paper of Bazhenova et al. (2016), a new family of polymerized Ti-catecholate complexes were introduced that contain both Ti^{4+} mono- and bis-catecholate complexes as their “elementary” components, suggesting that the presence of Ti-O-C “intermediate” was likely the result of partial oxidation-polymerization reactions.



Ti-O in the coating, observed as regions with darker hues in the BSE image with very strong Ti and O signals (Figure 2-5), was most likely formed by the decomposition of Ti-O-C “intermediate”, which did not require electron transfer. This is consistent with the cyclic voltammogram of Ti-catecholate complex showing a one-step electrochemical reaction (i.e., $[\text{Ti}(\text{cat})_3]^{2-}$ oxidation \rightarrow Ti-O-C “intermediate” formation) (Figure 2-4). Finally, Ti^{4+} ion released from intermediate was precipitated as Ti-hydroxide/oxide that formed the Ti-O material in the Ti-O-C coating. Based on these results, a three-step mechanism is proposed for the decomposition of Ti-catecholate complex (Figure 2-8). In Step 1, Ti-catecholate complex is partially oxidized, most probably via the Ti-O distorted bonds, and forms an intermediate phase. After this, the intermediate is gradually dissociated until “free” Ti^{4+} ion is released (Step 2). In the final step (Step 3), “free” Ti^{4+} ion is hydrolyzed and precipitated to form Ti-oxyhydroxide coatings.

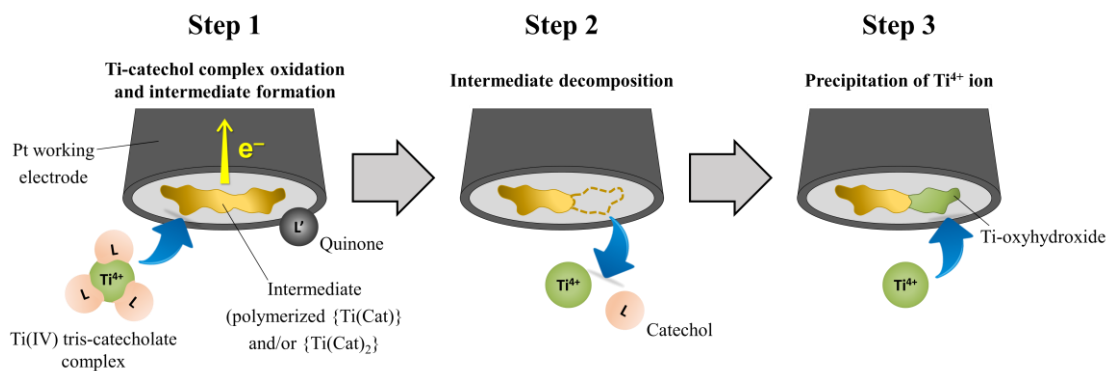


Figure 2-8. The schematic diagram of the anodic decomposition of Ti-catecholate complex.

2.3.3 Ti-based CME to suppress the release of As from arsenopyrite

Figure 2-9 shows the evolution of pH, Eh, and concentrations of As and Ti in DI water (control), catechol only and Ti-catecholate complex solution (CME). In the control, the pH rapidly decreased from 9 to 3.5 after 1 day due to the production of hydrogen ion by arsenopyrite oxidation (Mohan and Pittman, 2007; Schweigert et al., 2001), which is consistent with the redox potential (Eh) increase from ca. 250 to 500 mV (Figures 2-9a and b). The oxidation of arsenopyrite was also apparent in the rapid concentration increase of As in the control with time that reached ca. 1000 mg/L after 7 days. After this period, the change in As concentration with time became statistically insignificant indicating that apparent equilibrium was reached.

In the presence of catechol, As concentration was lower and the pH was higher than those of the control (Figures 2-9a and c), which means that arsenopyrite oxidation was somehow limited by this

organic compound. This suppressive effect could be explained by two possible mechanisms. First, catechol adsorption to the surface of arsenopyrite could suppress the overall dynamics of arsenopyrite oxidation by protecting the mineral from oxidants. This “direct” effect of catechol is most likely similar to that previously reported by Lalvani et al. (1990) and Belzile et al. (1997) on pyrite passivation by humic acids, large organic molecules that contain catechol as one of their most common functional groups. Noteworthy in the results was the continuous increase in As concentration with time in the catechol only solution, which suggests that although arsenopyrite oxidation was minimized, the mineral was not passivated by catechol (Figure 2-9c). Second, catechol could “indirectly” suppress arsenopyrite oxidation by consuming DO and complexing with Fe^{3+} , both of which are essential oxidants of arsenopyrite. According to Pracht et al. (2001), catechol consumes DO and metal ions such as Fe^{3+} in its oxidation to quinone (Eqs. (2-6) and (2-7)). Catechol has also been reported that form several stable complexes with Fe^{3+} (e.g., Eq. (2-8)) preventing it from directly acting as an oxidant of arsenopyrite (Schweigert et al., 2001). The combined effects of adsorption, consumption of oxidants and formation of Fe(III)-catecholate complexes could explain the decrease in As concentration observed in the presence of catechol.



The amounts of As released from arsenopyrite was even lower in Ti-catecholate complex solution (CME) compared with the other two cases (Figure 2-9c). After 25 days, As concentration in CME was ca. 330 mg/L, which was roughly four-fold lower than the control (1150 mg/L) and less than half of that in catechol only solution (880 mg/L). The pH was also higher in CME compared with the other cases while Eh was the lowest (Figures 2-9a and b). These results suggest that the substantial decrease in As release from arsenopyrite could be attributed to passivation of the mineral itself by Ti-catecholate complex. The passivation of arsenopyrite was closely related to Ti^{4+} precipitation that was apparent in the concentration decrease of dissolved Ti with time, which was not observed in Ti-catechol solution without arsenopyrite (Figure 2-9d). SEM-EDX results also showed that arsenopyrite in CME after 25 days exhibited strong signals of Ti and O (Figure 2-10).

The nature of this passivation layer was characterized using DRIFTS, a surface-sensitive technique able to identify molecular coordinations of ions and molecules in the structure of minerals (Carlson et al., 2002) including the very thin oxidation products of pyrite oxidation (Borda et al., 2004; Evangelou, 1995; Tabelin et al., 2017a). The DRIFTS spectra of washed arsenopyrite and leached residues (control, catechol and CME) show that several oxidation products were formed on arsenopyrite (Figure 2-11a). Absorption bands at 457 and 792 cm^{-1} are assigned to vibrations of Fe–As and arsenate (O–As–O), respectively. The stronger signal of arsenate (792 cm^{-1}) in the control indicates that arsenopyrite oxidation was more extensive in DI water compared with those in the other cases (Achimovičová and Baláž, 2005; Monte et al., 2002). Absorption bands at 569, 487 and 478 cm^{-1} are assigned to Fe–O bonds of iron oxide and the peak at 1371 cm^{-1} is most likely due to Fe³⁺–OH band of Fe³⁺–hydroxides or oxyhydroxides (Chernyshova, 2003; Monte et al., 2002; Tabelin et al., 2017a). Vibrations of sulfate coordinated with Fe³⁺ and Fe²⁺ were also observed at 1050 and 1163 cm^{-1} , respectively (Achimovičová and Baláž, 2005; Borda et al., 2004; Carlson et al., 2002; Chernyshova, 2003; Monte et al., 2002). The wide peak between 1115–1230 cm^{-1} is assigned to the vibrations of C–H (1165 cm^{-1}), O–H (1187 cm^{-1}), and C–O (1193 cm^{-1}), indicating two possibilities: (1) adsorbed catechol on arsenopyrite (Ramírez and López Navarrete, 1993), and (2) an “intermediate” phase formed on arsenopyrite by the partial decomposition of Ti-catecholate complex as discussed previously. The deconvoluted spectrum between 500 and 400 cm^{-1} of arsenopyrite leached in Ti-catecholate complex solution (Figure 2-11b) shows several absorption bands at 488, 474, 445 and 427 cm^{-1} , which are consistent with Ti–O vibrations (Alam and Cameron, 2002; Bagheri et al., 2013; Djaoued et al., 2002a, 2002b). This means that the Ti and O signals detected by SEM-EDX were likely due to the Ti-oxyhydroxide coating formed on arsenopyrite that passivated the mineral itself and limited the release of As.

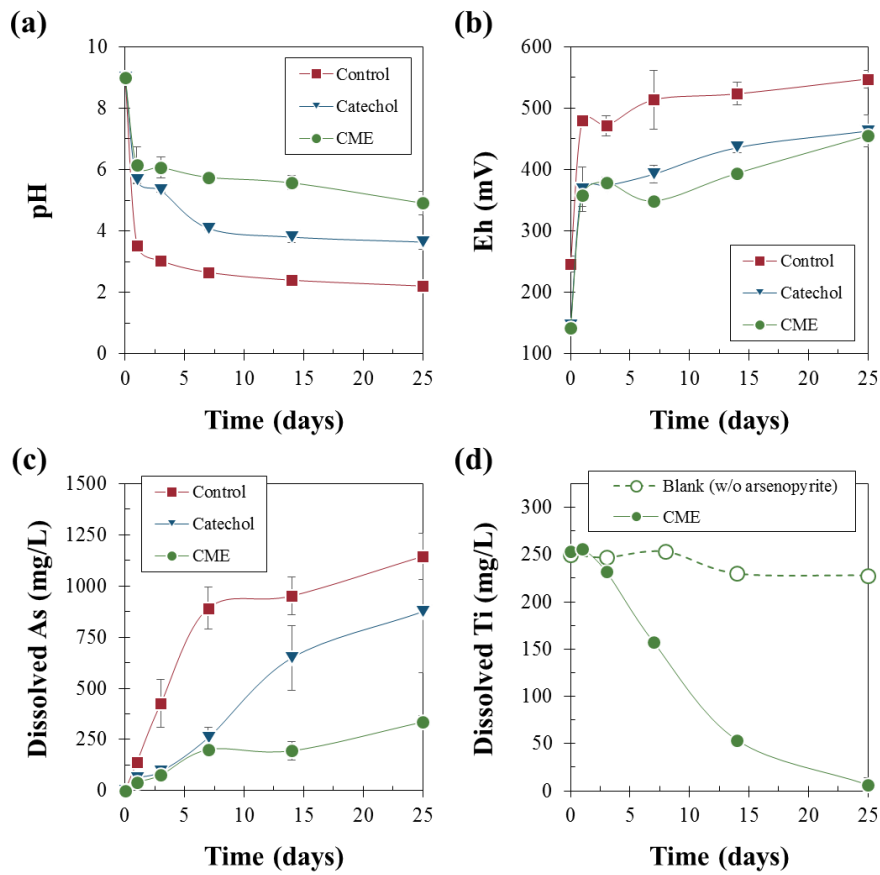


Figure 2-9. Leaching of arsenopyrite in DI water (control), catechol only, Ti-catecholate complex (CME): evolution of (a) pH and (b) Eh, and changes in the concentrations of (c) As and (d) Ti with time.

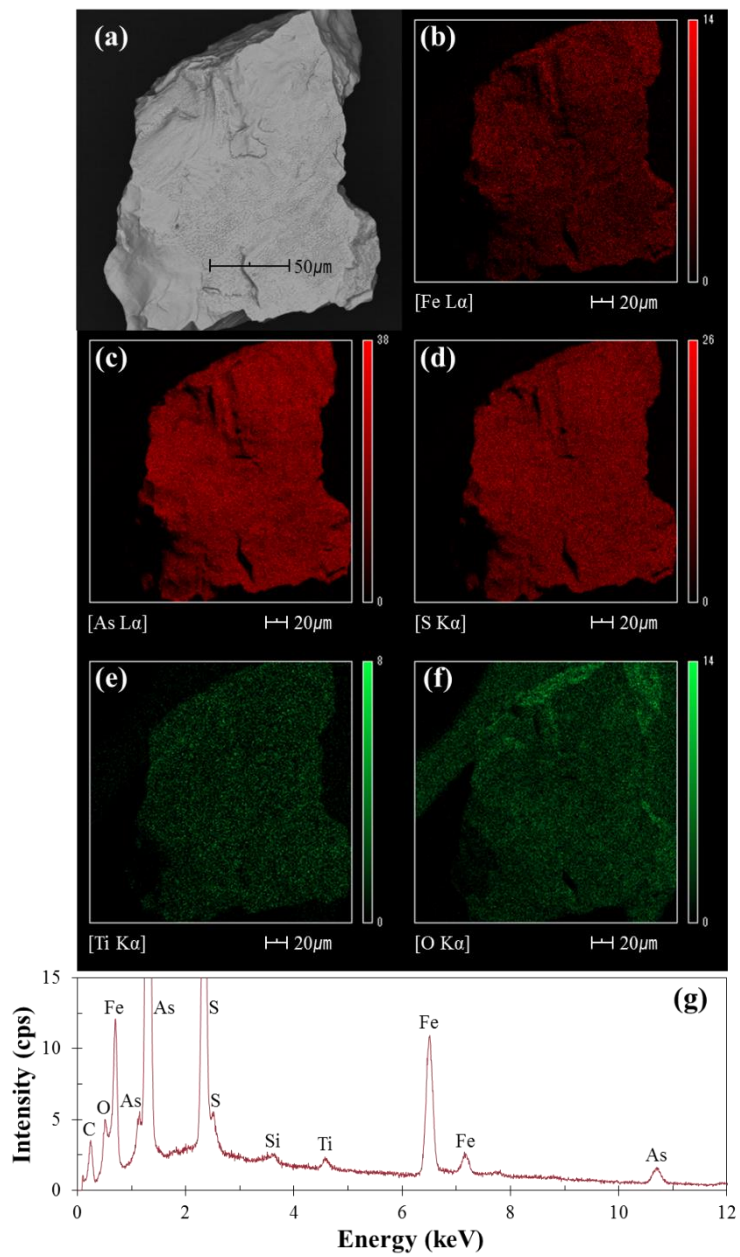


Figure 2-10. SEM-EDX analysis of arsenopyrite after Ti-based CME treatment: (a) SEM photomicrograph, elemental maps of (b) Fe, (c) As, (d) S, (e) Ti and (f) O, and (g) energy dispersive X-ray spectrum of scanned area.

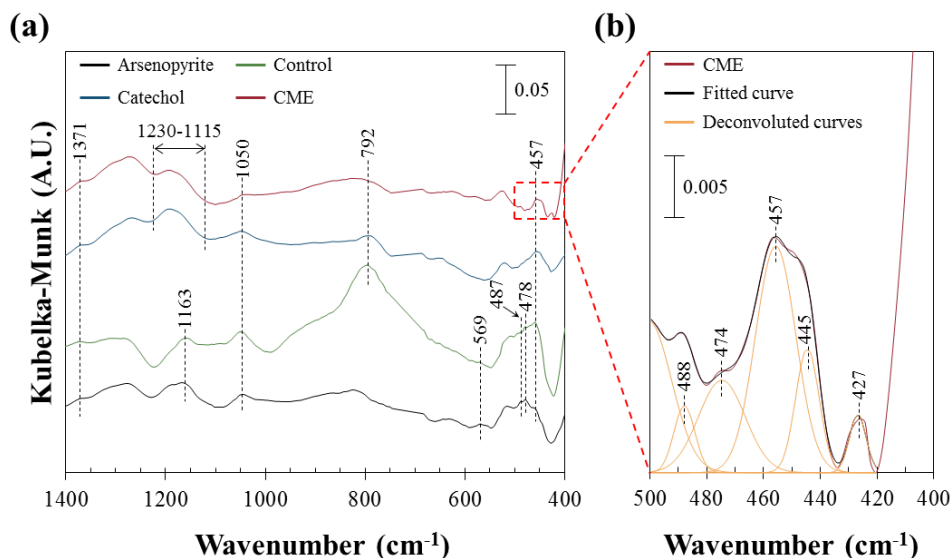


Figure 2-11. DRIFT spectra of arsenopyrite before and after 25 days of leaching experiments: (a) spectra of washed arsenopyrite and residues leached in DI water (control), catechol only and Ti-catechol solution (CME), and (b) deconvoluted spectrum of CME-treated arsenopyrite. Note that the scale of (a) and (b) are 0.05 and 0.005, respectively.

2.3.4 Anodic and cathodic half-cell reactions of arsenopyrite oxidation

Figure 2-12 shows the anodic and cathodic polarization curves of arsenopyrite electrode pretreated with DI water (control) and Ti-catecholate complex (CME). Current density profile of arsenopyrite pretreated with $[\text{Ti}(\text{cat})_3]^{2-}$ measured during anodic polarization (Figure 2-12a) was substantially lower than that of control, which means that $[\text{Ti}(\text{cat})_3]^{2-}$ could suppress anodic half-cell reaction of arsenopyrite oxidation. In the case of cathodic polarization (Figure 2-12b), CME-treated arsenopyrite also showed lower current density than the control, indicating that $[\text{Ti}(\text{cat})_3]^{2-}$ suppressed cathodic half-cell reaction of arsenopyrite oxidation. The area below current density curve indicates the amount of electric charge ($Q [\text{C}] = I [\text{A}] \times t [\text{s}]$) transferred during polarization. As shown in Table 2-2, the amounts of electric charge transferred through CME-treated arsenopyrite during both anodic and cathodic polarizations were lower than that of control, which are in good agreement with leaching result (Figure 2-9).

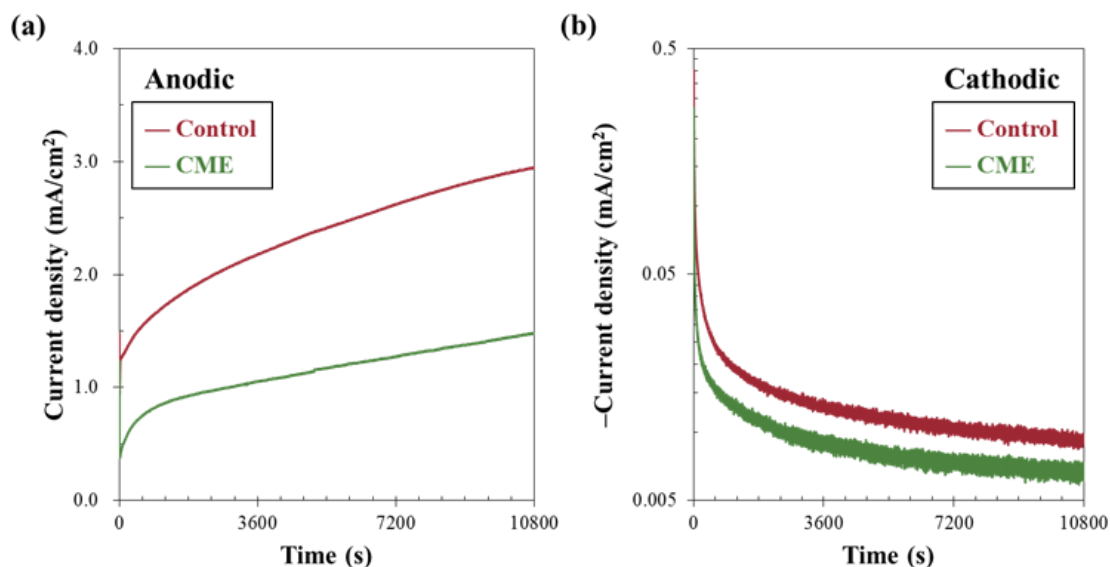


Figure 2-12. Chronoamperometric response of arsenopyrite pretreated with DI water (control) and Ti-catecholate complex (CME): (a) anodic polarization at +0.8 V vs. SHE, and (b) cathodic polarization at 0.0 V vs. SHE. Note that y-axes of Figures 3-5a and b are “Current density” and “-Current density,” respectively.

Table 2-2. Electric charges generated during anodic and cathodic polarizations of arsenopyrite pretreated in DI water (control) and Ti-catecholate complex (CME).

Pretreatment	Electric charge, Q (C/cm ²)	
	Anodic	Cathodic
Control	23.31	0.15
CME	12.34	0.10

2.3.5 The proposed mechanism of Ti-based CME

Based on the findings obtained in this chapter, a detailed mechanism of Ti-based CME was proposed as illustrated in Figure 2-13. Ti(IV) tris-catecholate complex is adsorbed on the surface of arsenopyrite where it is partially decomposed and forms an intermediate coating. This intermediate is further decomposed and releases “free” Ti⁴⁺ that is precipitated and forms Ti-oxyhydroxide coating protecting arsenopyrite against further oxidation.

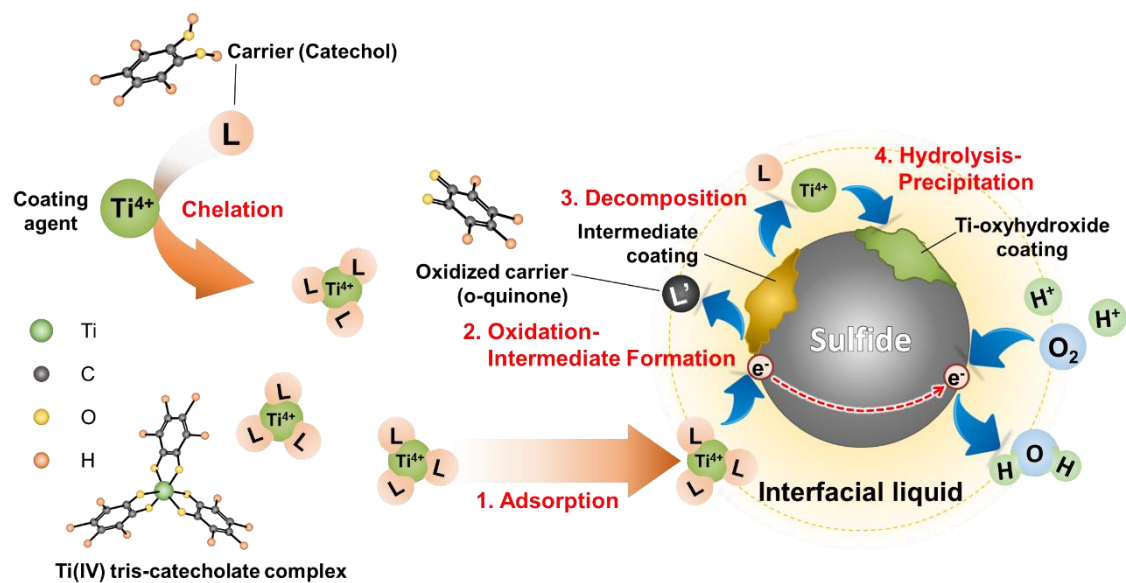


Figure 2-13. The schematic diagram of a proposed mechanism of Ti-based CME.

2.4 Conclusions

Ti-catecholate complex, $[\text{Ti}(\text{cat})_3]^{2-}$, was successfully synthesized by rapid neutralization of acidic Ti^{4+} and catechol solution to $\text{pH} > 5$. If gradually neutralized, Ti^{4+} ions were precipitated as TiO_2 or $\text{Ti}(\text{OH})_4$ at pH between 2 and 4. Once it precipitated, it became hard to be extracted by catechol. $[\text{Ti}(\text{cat})_3]^{2-}$ was oxidized at 680 mV vs. SHE most probably via partial oxidation of either one or both of the catechol molecules with distorted Ti–O bonds. The partially oxidized complex(es) likely reacted with each other to form an “intermediate” phase composed of Ti, O and C. Under certain conditions, the “intermediate” could be completely dissociated, which released “free” Ti^{4+} ion into solution that rapidly precipitated as Ti-oxyhydroxide. Moreover, Ti-based CME suppressed the release of As from arsenopyrite compared with those of control and catechol, while dissolved Ti^{4+} concentration decreased with time. SEM-EDX and DRIFTS analyses of CME-treated arsenopyrite indicated that it was covered with Ti-oxyhydroxide coating. This coating could suppress anodic and cathodic half-cell reactions of arsenopyrite oxidation.

This chapter is edited from “Park et al., 2018. Suppression of the release of arsenic from arsenopyrite by carrier-microencapsulation using Ti-catechol complex. *J. Hazard. Mater.* 344, 322–332.”

References

- Achimovičová, M. and Baláž, P., 2005. Influence of mechanical activation on selectivity of acid leaching of arsenopyrite. *Hydrometallurgy* 77, 3–7.
- Agatzini-Leonardou, S., Oustadakis, P., Tsakiridis, P.E. and Markopoulos, Ch., 2008. Titanium leaching from red mud by diluted sulfuric acid at atmospheric pressure. *J. Hazard. Mater.* 157, 579–586.
- Alam, M.J. and Cameron, D.C., 2002. Preparation and Characterization of TiO₂ Thin Films by Sol-Gel Method. *J. Sol-Gel Sci. Technol.* 25, 137–145.
- Bagheri, S., Shameli, K. and Hamid, S.B.A., 2013. Synthesis and Characterization of Anatase Titanium Dioxide Nanoparticles Using Egg White Solution via Sol-Gel Method. *J. Chem.* 1–5.
- Bazhenova, T.A., Kovaleva, N.V., Shilov, G.V., Petrova, G.N. and Kuznetsov, D.A., 2016. A family of titanium complexes with catechol ligands: structural investigation and catalytic application. *Eur. J. Inorg. Chem.* 33, 5215–5221.
- Belzile, N., Maki, S., Chen, Y.W. and Goldsack, D., 1997. Inhibition of pyrite oxidation by surface treatment. *Sci. Total Environ.* 196, 177–186.
- Bethke, C.M., 1992. *The Geochemist's Workbench – A User's Guide to Rxn, Act2, Tact, React and Gtplot.* University of Illinois, Urbana, Illinois.
- Boddu, V.M., Abburi, K., Talbott, J.L., Smith, E.D., and Haasch, R., 2008. Removal of arsenic (III) and arsenic (V) from aqueous medium using chitosan-coated biosorbent. *Water Res.* 42 (3), 633–642.
- Boles, K.A., 2014. *Electrochemistry of tris(tetrachlorocatecholate) complexes of manganese, iron, and cobalt.* Chemistry & biochemistry graduate theses & dissertations.
- Borda, M.J., Strongin, D.R. and Schoonen, M.A., 2004. A vibrational spectroscopic study of the oxidation of pyrite by molecular oxygen. *Geochim. Cosmochim. Acta* 68, 1807–1813.
- Borgias, B.A., Cooper, S.R., Koh, Y.B. and Raymond, K.N., 1984. Synthetic, Structural, and Physical Studies of Titanium Complexes of Catechol and 3,5-Di-*tert*-butylcatechol. *Inorg. Chem.* 23, 1009–1016.
- Carlson, L., Bingham, J.M., Schwertmann, U., Kyek, A. and Wagner, F., 2002. Scavenging of As from Acid Mine Drainage by Schwertmannite and Ferrihydrite: A Comparison with Synthetic Analogues. *Environ. Sci. Technol.* 36, 1712–1719.

- Chernyshova, I.V., 2003. An in situ FTIR study of galena and pyrite oxidation in aqueous solution. *J. Electroanal. Chem.* 558, 83–98.
- Corkhill, C.L., Vaughan, D.J., 2009. Arsenopyrite oxidation – a review. *Appl. Geochem.* 24, 2342–2361.
- Coussy, S., Benzaazoua, M., Blanc, D., Moszkowicz, P., Bussière, B., 2011. Arsenic stability in arsenopyrite-rich cemented paste backfills: A leaching test-based assessment. *J. Hazard. Mater.* 185, 1467–1476.
- Danilewicz, J.C., 2012. Review of Oxidative Processes in Wine and Value of Reduction Potentials in Enology. *Am. J. Enol. Vitic.* 63, 1–10.
- Djaoued, Y., Badilescu, S., Ashrit, P.V., Bersani, D., Lottici, P.P. and Brüning, R., 2002a. Low Temperature Sol-Gel Preparation of Nanocrystalline TiO₂ Thin Films. *J. Sol-Gel Sci. Technol.* 24, 247–254.
- Djaoued, Y., Badilescu, S., Ashrit, P.V., Bersani, D., Lottici, P.P. and Robichaud, J., 2002b. Study of Anatase to Rutile Phase Transition in Nanocrystalline Titania Films. *J. Sol-Gel Sci. Technol.* 24, 255–264.
- Evangelou, V.P., 1995. Pyrite oxidation and its control. CRC press, Boca Raton, FL.
- Gustafsson, J.P., 2010. Visual MINTEQ thermodynamic databases in GWB format. <http://vminteq.lwr.kth.se> (accessed 08 April 2017).
- He, S., Sun, H., Tan, D. and Peng, T., 2016. Recovery of titanium compounds from Ti-enriched product of alkali melting Ti-bearing blast furnace slag by dilute sulfuric acid leaching. *Procedia Environ. Sci.* 31, 977–984.
- Islam, A.B.M.R., Maity, J.P., Bundschuh, J., Chen, C.Y., Bhowmik, B.K., Tazaki, K., 2013. Arsenic mineral dissolution and possible mobilization in mineral-microbe-groundwater environment. *J. Hazard. Mater.* 262, 989–996.
- Johnson, D.B., Hallberg, K.B., 2005. Acid mine drainage remediation options: a review. *Sci. Total Environ.* 338, 3–14.
- Lalvani, S.B., Deneve, B.A. and Weston, A., 1990. Passivation of pyrite due to surface treatment. *Fuel* 69, 1567–1569.
- McKibben, M.A., Tallant, B.A., del Angel, J.K., 2008. Kinetics of inorganic arsenopyrite oxidation in acidic aqueous solutions. *Appl. Geochem.* 23, 121–135.

- Meng, F.C., Xue, T.Y., Liu, Y.H., Zhang, G.Z. and Qi, T., 2016. Recovery of titanium from undissolved residue (tionite) in titanium oxide industry via NaOH hydrothermal conversion and H₂SO₄ leaching. *Trans. Nonferrous Met. Soc. China* 26, 1696–1705.
- Mohan, D., Pittman, C.U., 2007. Arsenic removal from water/wastewater using adsorbents – a critical review. *J. Hazard. Mater.* 142 (1–2), 1–53.
- Monte, M.B.M., Dutra, A.J.B., Albuquerque, C.R.F., Tondo, L.A. and Lins, F.F., 2002. The influence of the oxidation state of pyrite and arsenopyrite on the flotation of an auriferous sulphide ore. *Miner. Eng.* 15, 1113–1120.
- Murciego, A., Álvarez-Ayuso, E., Pellitero, E., Rodríguez, M.A., García-Sánchez, A., Tamayo, A., Rubio, J., Rubio, F., Rubin, J., 2011. Study of arsenopyrite weathering products in mine wastes from abandoned tungsten and tin exploitations. *J. Hazard. Mater.* 186, 590–601.
- Park, I., Tabelin, C.B., Magaribuchi, K., Seno, K., Ito, M., Hiroyoshi, N., 2018. Suppression of the release of arsenic from arsenopyrite by carrier-microencapsulation using Ti-catechol complex. *J. Hazard. Mater.* 344, 322–332.
- Pracht, J., Boenigk, J., Isenbeck-Schröter, M., Keppler, F. and Schöler, H.F., 2001. Abiotic Fe(III) induced mineralization of phenolic substances. *Chemosphere* 44, 613–619.
- Ramírez, F.J. and López Navarrete, J.T., 1993. Normal coordinate and rotational barrier calculations on 1,2-dihydroxybenzene. *Vib. Spectrosc.* 4, 321–334.
- Salzsauler, K.A., Sidenko, N.V., Sherriff, B.L., 2005. Arsenic mobility in alteration products of sulfide-rich, arsenopyrite-bearing mine wastes, Snow Lake, Manitoba, Canada. *Appl. Geochem.* 20, 2303–2314.
- Satur, J., Hiroyoshi, N., Tsunekawa, M., Ito, M. and Okamoto, H., 2007. Carrier-microencapsulation for preventing pyrite oxidation. *Int. J. Miner. Eng.* 83, 116–124.
- Schweigert, N., Zehnder, A.J.B. and Eggen, R.I.L., 2001. Chemical properties of catechols and their molecular modes of toxic action in cells, from microorganisms to mammals. *Environ. Microbiol.* 3, 81–91.
- Sever, M.J. and Wilker, J.J., 2004. Visible absorption spectra of metal-catecholate and metal-tironate complexes. *Dalton Trans.* 1061–1072.
- Tabelin, C.B., Igarashi, T., Arima, T., Sato, D., Tatsuhara, T., Tamoto, S., 2012. Characterization and evaluation of arsenic and boron adsorption onto natural geologic materials, and their application in the disposal of excavated altered rock. *Geoderma* 213, 163–172.

Tabelin, C.B., Veerawattananun, S., Ito, M., Hiroyoshi, N. and Igarashi, T., 2017a. Pyrite oxidation in the presence of hematite and alumina: I. Batch leaching experiments and kinetic modeling calculations. *Sci. Total Environ.* 580, 687–698.

Tabelin, C.B., Veerawattananun, S., Ito, M., Hiroyoshi, N. and Igarashi, T., 2017b. Pyrite oxidation in the presence of hematite and alumina: II. Effects on the cathodic and anodic half-cell reactions. *Sci. Total Environ.* 581-582, 126–135.

Wright, C.I. and Mason, H.S., 1946. The oxidation of catechol by tyrosinase. *J. biol. Chem.* 165, 45–53.

Yang, J., Stuart, M.A.C. and Kamperman, M., 2014. Jack of all trades: versatile catechol crosslinking mechanisms. *Chem. Soc. Rev.* 43, 8271–8298.

CHAPTER 3 – IMPROVEMENTS IN THE KINETICS OF TITANIUM-BASED CARRIER-MICROENCAPSULATION

3.1 Introduction

In the previous chapter, Ti-based CME was successfully shown to suppress the release of As from arsenopyrite because of the formation of a surface protective layer on the mineral. However, long-term treatment (at least 14 days) is required to create a coating thick enough to be effective, which makes Ti-based CME impractical to be applied to real treatment system. One possibility of this sluggish formation of the surface protective coating is lack of oxidants for the complex decomposition. In natural conditions, dissolved oxygen (DO) acts as an oxidant but its concentration is low, approximately 8 mg/L at 25 °C. This means that if some additional oxidants are added into the system, the coating formation during Ti-based CME treatment might be improved. In this regard, copper(II) ammine complex (e.g., tetraamminecopper(II), $[\text{Cu}(\text{NH}_3)_4]^{2+}$) was selected in this study because it can act as an oxidant under alkaline conditions (pH 8–11) that might accelerate the oxidative decomposition of Ti-catecholate complex as illustrated in Figure 3-1 (Koyama et al., 2006; Oishi et al., 2007). The effect of not only Cu^{2+} - NH_3 complex but also Cu^{2+} on Ti-based CME was examined because it has been reported to oxidize catechol, which would be available to improve the kinetics of Ti-based CME (Schweigert et al., 2000; 2001; Speier, 1986). Finally, the effect of temperature was also studied because it can be one approach to accelerate the chemical reactions like the decomposition of Ti-catecholate complex.

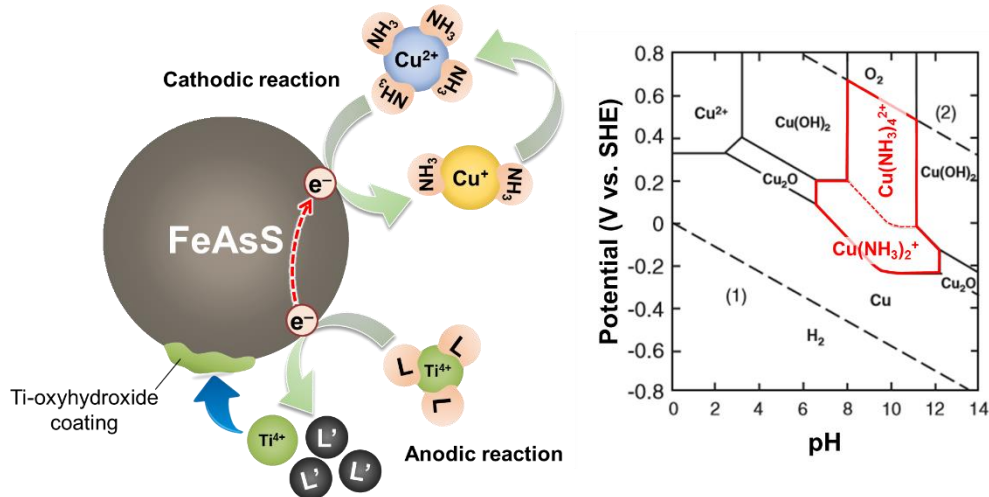


Figure 3-1. The schematic diagram of the catalytic effect of Cu^{2+} - NH_3 complex in Ti-based CME and Eh-pH diagram of Cu^{2+} - NH_3 - H_2O system at 25 °C calculated by assuming that the activity of Cu is 0.5 and the total concentration of ammonia is $7.0 \text{ kmol}\cdot\text{m}^{-3}$ (Koyama et al., 2006).

3.2 Materials and methods

3.2.1 Materials

The arsenopyrite sample used in this chapter is the same as that used in Chapter 2. The solution containing Ti-catecholate complex was prepared in an identical way as introduced in the previous chapter. For the source of Cu^{2+} , copper sulfate pentahydrate ($\text{CuSO}_4 \cdot 5\text{H}_2\text{O}$, Wako Pure Chemical Industry Ltd., Japan) was used while ammoniacal solution was prepared by mixing ammonia solution (NH_4OH , Wako Pure Chemical Industry Ltd., Japan) and ammonium sulfate ($(\text{NH}_4)_2\text{SO}_4$, Wako Pure Chemical Industry Ltd., Japan) at 1:0.5 ratio, i.e., $\text{NH}_3:\text{NH}_4^+ = 1:1$.

3.2.2 Effects of temperature and Cu^{2+} - NH_3 complex on Ti-based CME

Prior to the leaching experiments, arsenopyrite sample was washed to remove any oxidized layer formed on its surface using a method developed by McKibben et al. (2008). As shown in Figure 3-2, 200 ml of the prepared Ti-catechol solution (1 mM Ti^{4+} and 3 mM catechol) was poured into a 500 ml four-necked reactor set in a heating mantle that keeps a constant temperature. The reflux condenser was inserted in one port to prevent the evaporation of solution at a high temperature. Solution was mechanically stirred using an overhead agitator at 600 rpm, an optimized agitation speed for the sufficient dispersion of particles determined by the preliminary leaching tests. Once the solution temperature reached thermal equilibrium (30, 50, and 70 °C), 2 g of arsenopyrite sample were added to the reactor and a 2 ml of solution was periodically collected at a predetermined time interval. The solution was filtered through 0.2 μm syringe-driven membrane filter and analyzed by ICP-AES.

Similarly, the effects of Cu^{2+} - NH_3 complex on Ti-based CME were investigated using the same setup as explained above. Cu^{2+} - NH_3 complex, 1 mM $\text{CuSO}_4 \cdot 5\text{H}_2\text{O}$ dissolved in a mixture of 5 mM NH_4OH and 2.5 mM $(\text{NH}_4)_2\text{SO}_4$ (i.e., 1 mM Cu^{2+} with 10 mM $\text{NH}_3/\text{NH}_4^+$), was mixed with 1 mM Ti-catechol solution, and then used for leaching experiments at 30 °C and 600 rpm with 2 g/200 ml pulp density.

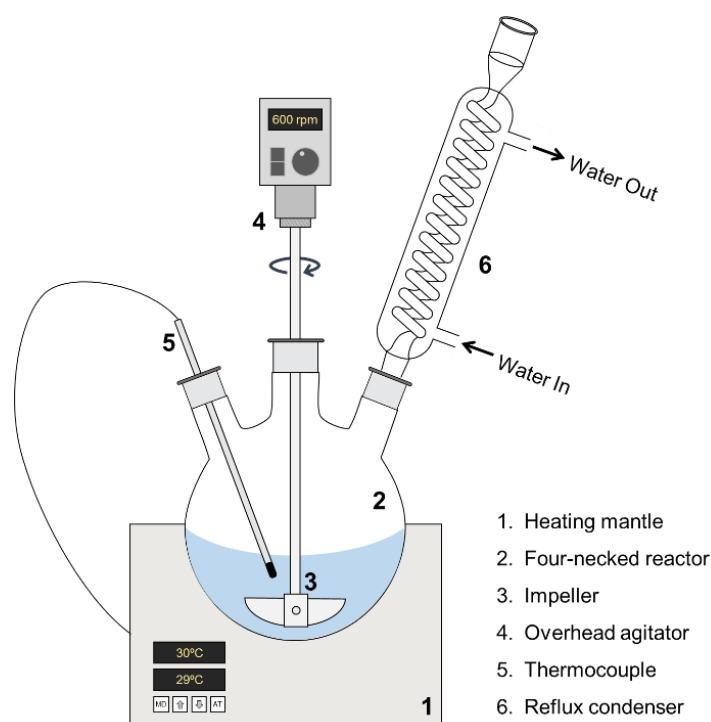


Figure 3-2. The schematic diagram of the reactor-type leaching apparatus.

3.2.3 Interaction of Cu^{2+} with Ti-catechol complex and/or arsenopyrite

To investigate the effects of the presence of Cu^{2+} on Ti-based CME, batch leaching experiments were conducted. One gram of arsenopyrite sample and 10 ml of leachant (5 mM $[\text{Ti}(\text{cat})_3]^{2-}$ with or without 5 mM Cu^{2+}) were put in a 50 ml Erlenmeyer flask and shaken in a constant temperature water bath (25 °C) at 120 min^{-1} under ambient conditions. At pre-designated time intervals, solution was collected by filtration using 0.2 μm syringe-driven membrane filter and analyzed by ICP-AES. The interaction of Cu^{2+} with either $[\text{Ti}(\text{cat})_3]^{2-}$ or arsenopyrite was also investigated to elucidate the behavior of Cu^{2+} during Ti-based CME. To understand the interaction between Cu^{2+} and $[\text{Ti}(\text{cat})_3]^{2-}$, Cu^{2+} was gradually added into 1 mM $[\text{Ti}(\text{cat})_3]^{2-}$ solution stirred magnetically at 200 rpm. Afterwards the mixture was allowed to stabilize for 10 min, and a 2 ml of solution was taken. This procedure was repeated until the concentration of Cu^{2+} reached 75 mg/L. For the interaction between Cu^{2+} and arsenopyrite, 50 ml of 1 mM Cu^{2+} solution and 1 g of washed arsenopyrite were mixed at 200 rpm under ambient conditions. After 1 day, the suspension was filtered using a 0.2 μm membrane filter and the filtrate was analyzed by ICP-AES while the residue was thoroughly washed with DI water, dried in a vacuum oven dryer at 40 °C for 24 h, and analyzed by scanning electron microscopy with energy dispersive X-ray spectroscopy (SEM-EDX, S5X-550, Shimadzu Corporation, Japan). Some experiments were done in triplicates to ascertain that the differences observed were statistically significant.

3.3 Results and discussion

3.3.1 Effects of temperature

Leaching experiments under various temperature ranging from 30 to 70 °C were conducted to identify the temperature dependence of the reaction rate of Ti-catecholate complex decomposition. At 30 °C, the concentration of As released from arsenopyrite continuously increased for 48 h and afterwards, As release was stopped (Figure 3-3a). Meanwhile, dissolved Ti gradually decreased with time (Figure 3-3b), indicating that Ti-catecholate complex was decomposed and released Ti^{4+} was precipitated as TiO_2 as discussed in Chapter 2. At 50 °C, the initial rate of As release was faster than that at 30 °C but after 24 h, the concentration of dissolved As did not change until 72 h (Figure 3-3a), which means that the suppressive effect of Ti-based CME on arsenopyrite oxidation was achieved early at a higher temperature due most likely to the faster complex decomposition/coating formation (Figure 3-3b). In general, the oxidation rates of not only arsenopyrite but also most of the minerals are known to be accelerated at a high temperature (Yu et al., 2004, 2007). However, it is interesting to note that with further increasing temperature up to 70 °C, the release of As from arsenopyrite was significantly suppressed compared with those at 30 and 50 °C. This phenomenon could be explained by a rapid decrease of the Ti^{4+} concentration at 70 °C, implying that Ti^{4+} was precipitated and transformed into the surface coatings protecting arsenopyrite against further oxidation.

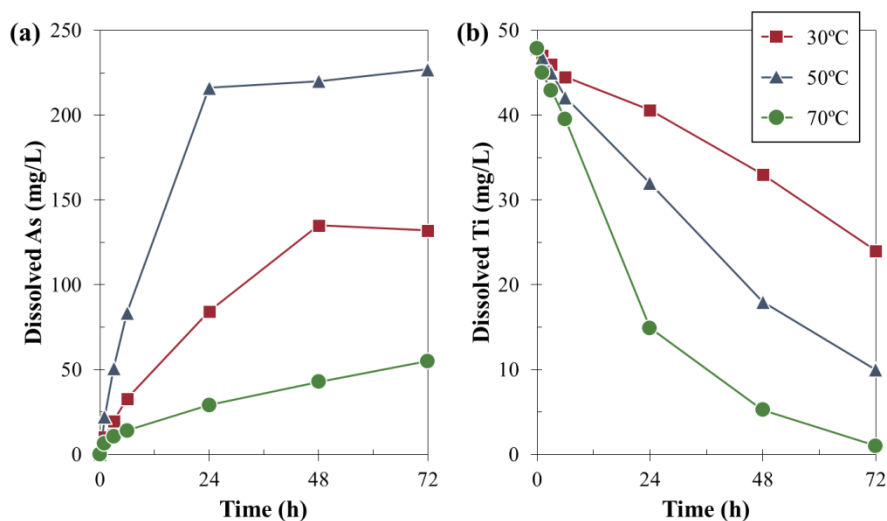


Figure 3-3. Leaching of arsenopyrite in Ti-catechol solution under various temperature: changes in the concentrations of (a) As and (b) Ti with time.

As shown in Figure 3-3b, the rate of complex decomposition was strongly dependent on the temperature. To further understand the kinetics of the complex decomposition, pseudo-first-order kinetic model was applied. The detailed mechanism of Ti-based CME for passivating arsenopyrite was identified in Chapter 2; that is, Ti-catecholate complex is decomposed on the surface of arsenopyrite and it forms intermediate coating finally transformed into TiO₂ (Eq. (3-1)).



As a consequence of the complex decomposition, the concentration of Ti⁴⁺ decreases, so its rate could be expressed by the following equation:

$$rate = \frac{d[X]}{dt} = -k[X] \quad (3-2)$$

where $[X]$ is the concentration of Ti⁴⁺, t is time, and k is rate constant.

$$\int_{[X]_0}^{[X]_t} \frac{d[X]}{[X]} = -k \int_{t_0}^t dt \quad (3-3)$$

As shown in Eq. (3-3), by rearranging and integrating Eq. (3-2) with boundary conditions ($t = 0$, $[X] = [X]_0$ and $t = t$, $[X] = [X]_t$), the integrated rate law was obtained as illustrated in Eq (3-4), a form of a linear equation ($y = ax + b$), in which the slope “ a ” corresponds to the rate constant k in a plot of $\ln [X]_t$ vs. t .

$$\ln[X]_t = \ln[X]_0 - kt \quad (3-4)$$

To determine the rate constants of the complex decomposition at various temperatures, the experimental data show in Figure 3-3b were applied to the pseudo-first-order kinetic model (Eq. (3-4)) and the corresponding results were illustrated in Figure 3-4 and Table 3-1. The rate constants of complex decomposition at 30, 50, and 70 °C were 0.009, 0.021, and 0.051 h⁻¹, respectively, and the coefficients of determination (R^2) were 0.9779–0.9935, which supports the validity of the applied model. In the parity plots (Figure 3-5), the R^2 values were greater than 0.9796, which also confirms that the obtained rate constants are reliable.

Using the obtained rate constants, activation energy for the reaction of complex decomposition was calculated by Arrhenius equation:

$$k = Ae^{-E_a/RT} \quad (3-5)$$

where A is the pre-exponential factor (h⁻¹), E_a is the activation energy for the reaction of complex decomposition (J/mol), R is the universal gas constant (J/mol·K), and T is temperature in Kelvin (K). Figure 3-6 shows Arrhenius plot, fitting with a linear relation between $\ln k$ and T^{-1} corresponding to $k = 24711e^{-37405/RT}$, from which the activation energy was determined to be 37.4 kJ/mol.

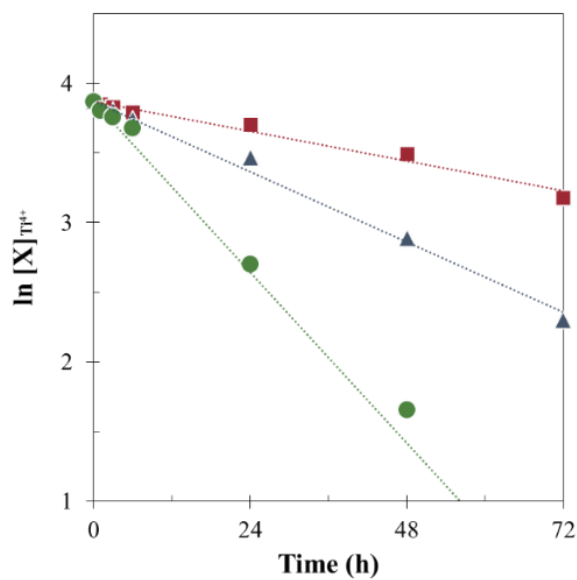


Figure 3-4. Linear pseudo-first-order kinetic model for Ti^{4+} precipitation at various temperatures.

Table 3-1. Values of apparent rate constant (k) and correlation coefficient (R^2) obtained from pseudo first-order kinetic model shown in Figure 3-4.

Temperature ($^{\circ}\text{C}$)	Rate constant (h^{-1})	R^2
30	0.009	0.9779
50	0.021	0.9935
70	0.051	0.9914

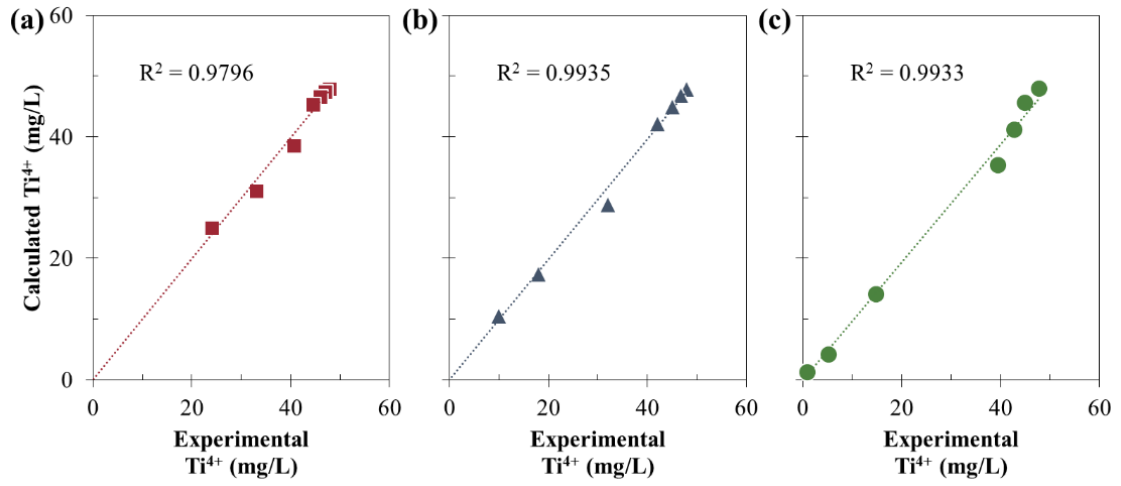


Figure 3-5. The parity plots comparing experimental and calculated data of Ti⁴⁺ concentration at (a) 30 °C, (b) 50 °C, and (c) 70 °C.

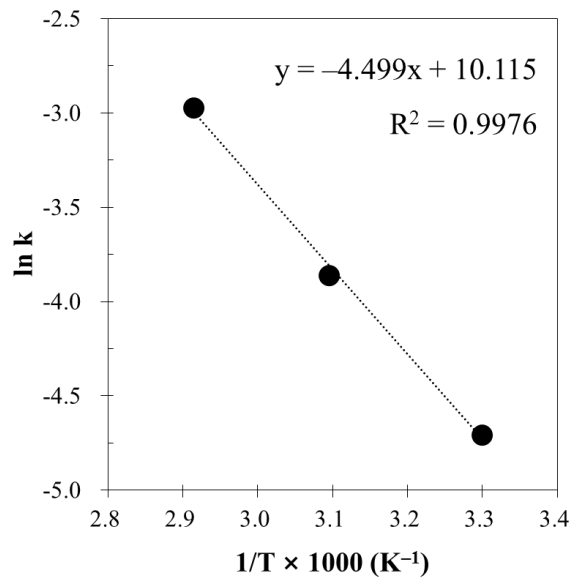


Figure 3-6. Arrhenius plot between $\ln k$ and T^{-1} .

3.3.2 Effects of $\text{Cu}^{2+}\text{-NH}_3$ complex

To investigate the effects of $\text{Cu}^{2+}\text{-NH}_3$ complex on Ti-based CME, leaching of arsenopyrite in Ti-catechol solution in absence and presence of $\text{Cu}^{2+}\text{-NH}_3$ complex was carried out (Figure 3-7). The As release from arsenopyrite was substantially suppressed with $\text{Cu}^{2+}\text{-NH}_3$ complex (Figure 3-7a). After 7 days, the concentrations of As released from arsenopyrite in Ti-catechol solution with and without $\text{Cu}^{2+}\text{-NH}_3$ complex were around 8 and 35 mg/L As, respectively. It was also confirmed that $\text{Cu}^{2+}\text{-NH}_3$ complex accelerated the precipitation of Ti^{4+} (Figure 3-7b). Moreover, dissolved Cu concentration also decreased with time and its trend was similar to the change in dissolved Ti concentration (Figure 3-7c).

To check the interaction between Ti-catecholate and $\text{Cu}^{2+}\text{-NH}_3$ complexes, Ti-catechol solutions were mixed with $\text{Cu}^{2+}\text{-NH}_3$ complex in the absence of arsenopyrite. As shown in Figure 3-8a, Ti-catecholate complex was stable and its concentration was not changed without $\text{Cu}^{2+}\text{-NH}_3$ complex but Ti-catecholate complex became unstable and the concentration decreased with time when $\text{Cu}^{2+}\text{-NH}_3$ complex was mixed. The precipitation of Cu^{2+} was also observed (Figure 3-8b), implying that Ti-catecholate complex was most likely precipitated with $\text{Cu}^{2+}\text{-NH}_3$ complex. Although the presence of $\text{Cu}^{2+}\text{-NH}_3$ suppressed As release from arsenopyrite (Figure 3-7a), it would not selectively form the protective coating on arsenopyrite because Ti-catecholate complex was not electrochemically decomposed on the surfaces of the sulfide mineral but it was just precipitated in the bulk solution phase as shown in Figure 3-8.

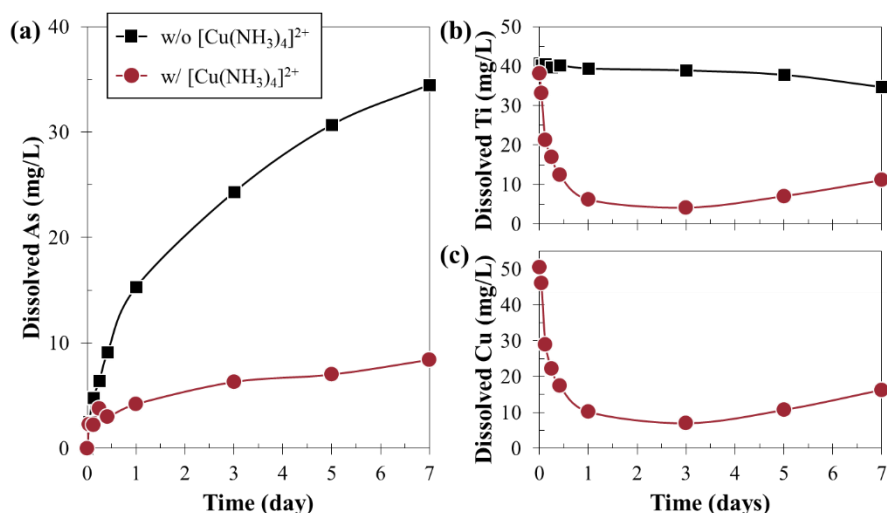


Figure 3-7. Leaching of arsenopyrite in Ti-catechol solution with and without $\text{Cu}^{2+}\text{-NH}_3$ complex: changes in the concentrations of (a) As, (b) Ti, and (c) Cu with time.

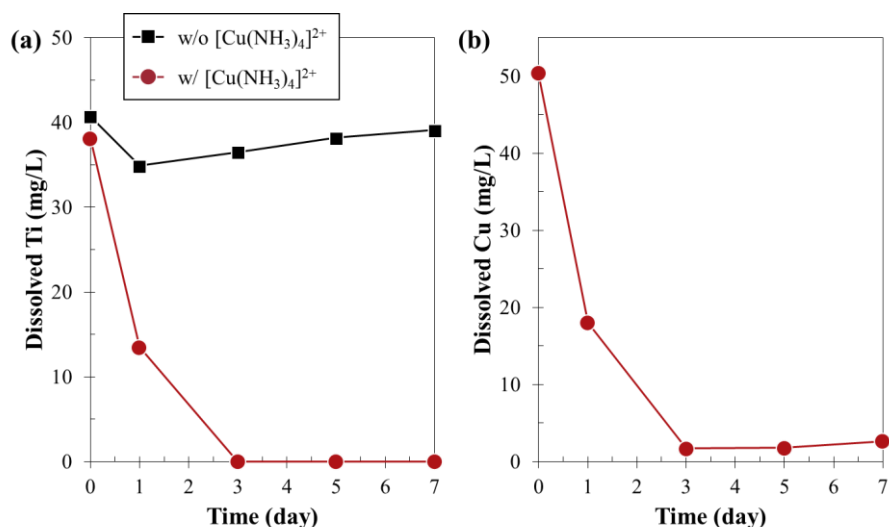


Figure 3-8. Stability of Ti-catecholate complex in the absence and presence of Cu^{2+} - NH_3 complex: changes in the concentrations of (a) Ti and (b) Cu with time.

3.3.3 Effects of Cu^{2+}

The effect of Cu^{2+} , a common co-existing ion in the wastes produced after mineral processing and/or extractive metallurgy, on Ti-based CME for arsenopyrite was examined (Figure 3-9). Figure 3-9a compares the release of As from arsenopyrite with and without Cu^{2+} addition. The concentrations of As released from arsenopyrite was lower with Cu^{2+} than that without Cu^{2+} , which means that the addition of Cu^{2+} is effective to suppress arsenopyrite oxidation. This suppressive effect was most likely achieved by faster precipitation of Ti^{4+} with Cu^{2+} (Figure 3-9b). Because the concentration of Cu^{2+} also decreased with time (Figure 3-9b), there is a possibility that co-precipitation of Ti-catecholate complex and Cu^{2+} occurs.

To confirm this, the stability of Ti-catecholate complex in the presence of various concentrations of Cu^{2+} was examined by mixing Ti-catecholate complex and Cu^{2+} in the absence of arsenopyrite, and the results indicated that the concentration of Ti was not changed drastically even though around 75 mg/L Cu^{2+} was added (Figure 3-10). Another possibility of the precipitation of Cu^{2+} is likely due to the interaction between Cu^{2+} and arsenopyrite, so a shaking flask experiment was carried out by mixing 1 g of arsenopyrite and 50 mL of the solution containing 1 mM Cu^{2+} . Figure 3-11 shows that substantial amounts of Cu^{2+} , approximately 90%, were precipitated after 1 day of shaking although the pH of leachate was around 3.8 at which the solubility of Cu^{2+} was very high as shown in the solubility diagram of Cu^{2+} (Figure 3-12). According to Guongming and Hongen (1989) and Chandraprabha et al. (2005), Cu^{2+} was reported to be adsorbed onto the As and/or S sites

of arsenopyrite, so leaching residue was analyzed using SEM-EDX to check whether Cu^{2+} was adsorbed on the surface of arsenopyrite or not. SEM-EDX results show that on the surface of arsenopyrite, there were particulates mainly composed of Cu and S with low signals of Fe and As, which supported the adsorption of Cu^{2+} onto the surface of arsenopyrite as a CuS-like compound (Figure 3-13). When copper sulfide (e.g., chalcocite (Cu_2S) and covellite (CuS)) and arsenopyrite are in contact, a galvanic cell would be formed, where copper sulfide with a lower rest potential acts as an anode and is preferentially dissolved while the arsenopyrite with a higher rest potential behaves like a cathode and is galvanically protected (Allison et al., 1972). According to Walker et al. (2006), anodic half-cell reaction of arsenopyrite oxidation is the rate-determining step. The anode property of arsenopyrite was changed in the presence of Cu^{2+} due to the formation of CuS-like compounds on arsenopyrite surface, and thereby the rate of Ti-catechol complex decomposition was most likely accelerated (Figure 3-9b).

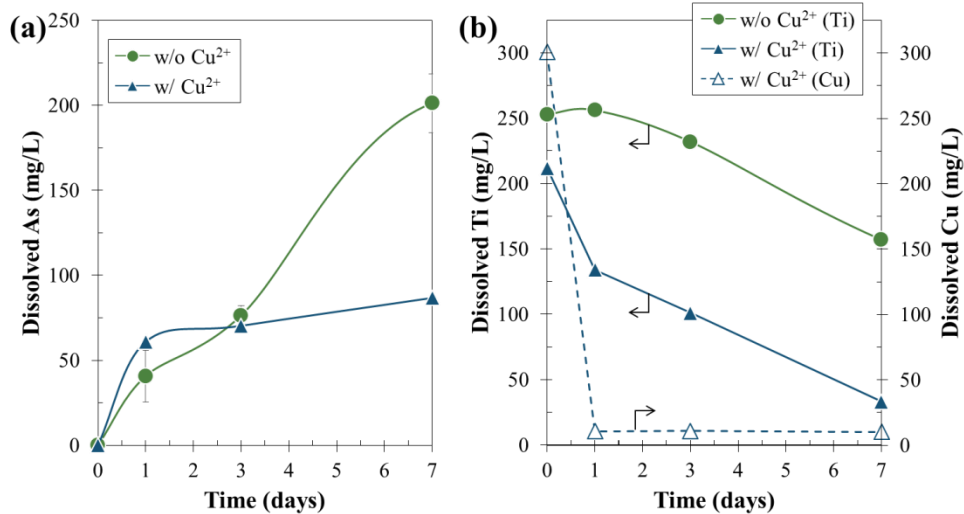


Figure 3-9. Leaching of arsenopyrite in Ti-catechol solution with and without Cu^{2+} : changes in the concentrations of (a) As and (b) Ti & Cu with time.

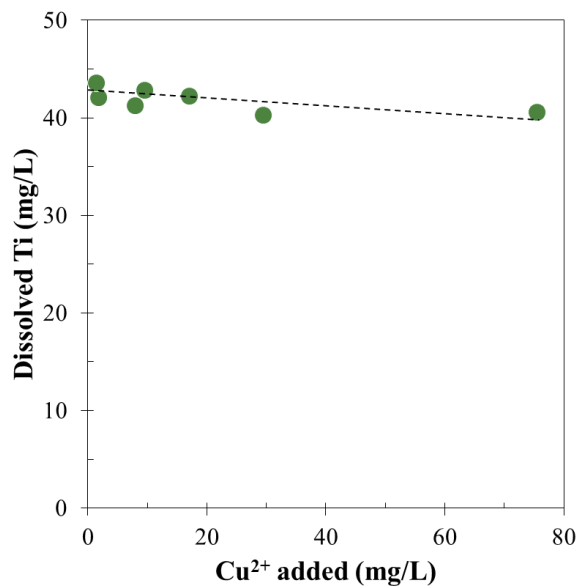


Figure 3-10. Stability of Ti-catecholate complex with varying the concentration of Cu²⁺ added.

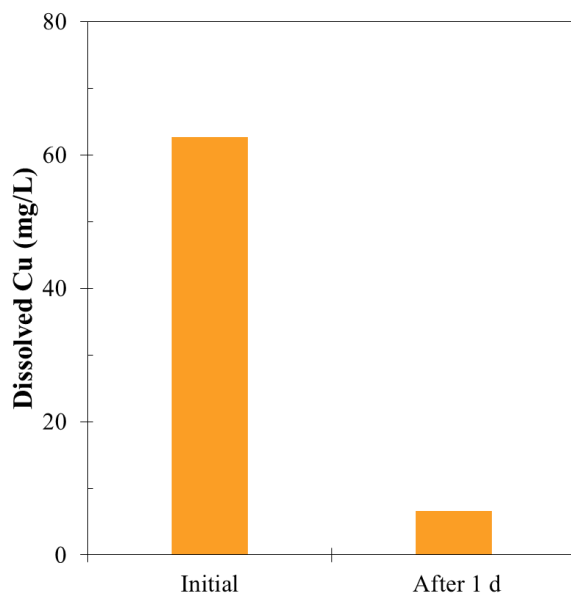


Figure 3-11. Interaction between Cu²⁺ and arsenopyrite.

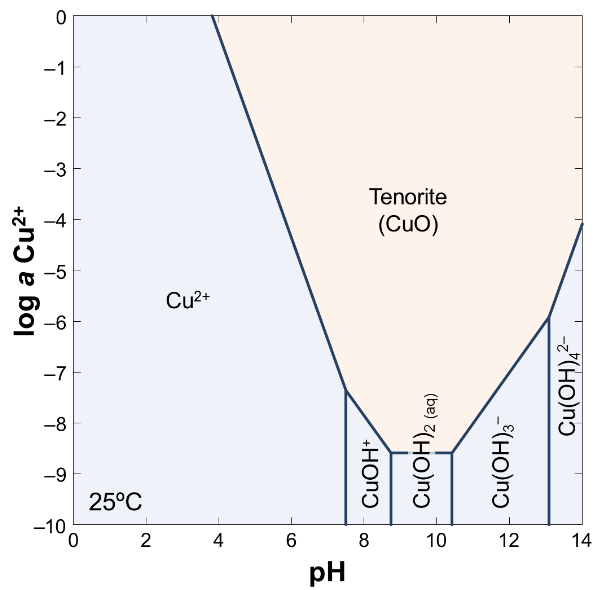


Figure 3-12. Log activity–pH predominance diagram of Cu^{2+} - H_2O system at 25 °C and 1.013 bar created using the Geochemist's Workbench with the MINTEQA database (Bethke, 1992; Gustafsson, 2010).

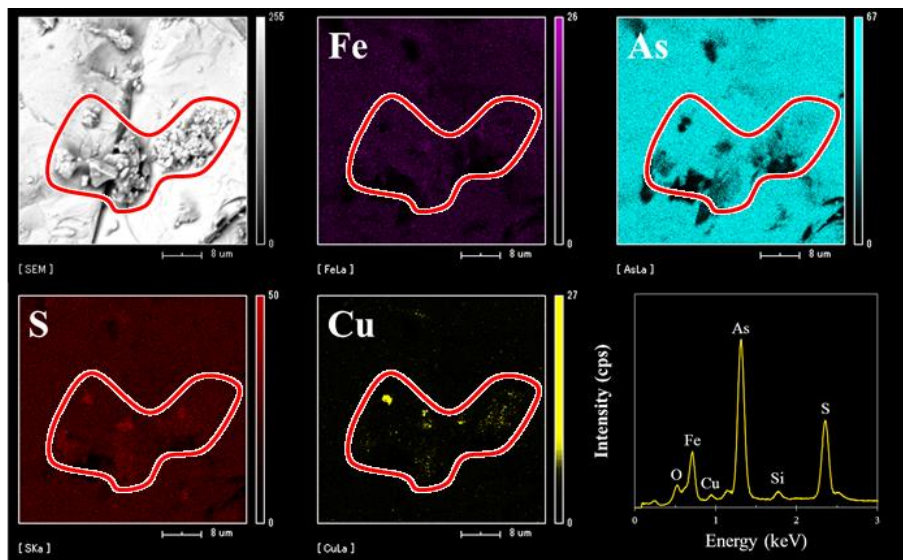


Figure 3-13. SEM-EDX results of arsenopyrite treated with the solution containing Cu^{2+} for 1 day.

3.4 Conclusions

In this chapter, the temperature dependency as well as the effects of additives on Ti-catecholate complex decomposition were investigated. The decomposition of $[\text{Ti}(\text{cat})_3]^{2-}$ was strongly dependent on the temperature; that is, its decomposition was significantly accelerated at a higher temperature. Moreover, these results were well fitted with pseudo-first-order kinetic model. The rate constants of complex decompositions at 30, 50, and 70 °C were estimated at around 0.009, 0.021, and 0.051 h^{-1} , respectively, and its activation energy was calculated to be 37.4 kJ/mol.

Cu^{2+} - NH_3 complex showed a negative effect on Ti-based CME because it lowered the stability of Ti-catecholate complex by co-precipitation, resulting in the loss of ability to specifically target the problematic minerals (e.g., arsenopyrite and pyrite) in complex system. However, by adding Cu^{2+} into Ti-based CME system, the rate of Ti-catecholate complex decomposition could be accelerated due most likely to the formation of CuS -like compounds that changed the anode property of arsenopyrite. Although copper is a valuable material, its application to Ti-based CME is available because it is commonly found in wastewaters produced from mineral processing and hydrometallurgical plants for copper ores.

References

- Allison, S.A., Goold, L.A., Nichol, M.J., Granville, A., 1972. A determination of the products of reaction between various sulfide minerals and aqueous xanthate solution, and a correlation of the products with electrode rest potentials. *Metall. Trans.* 3 (10), 2613–2618.
- Bethke, C.M., 1992. *The Geochemist's Workbench – A User's Guide to Rxn, Act2, Tact, React and Gtplot*. University of Illinois, Urbana, Illinois.
- Chandraprabha, M.N., Natarajan, K.A., Somasundaran, P., 2005. Selective separation of pyrite from chalcopyrite and arsenopyrite by biomodulation using *Acidithiobacillus ferrooxidans*. *Int. J. Miner. Proc.* 75 (1–6), 113–122.
- Guongming, L. and Hongen, Z., 1989. The chemical principles of flotation, activation and depression of arsenopyrite. In: *Proceedings of the international symposium on processing of complex ores*, Halifax, 61–70.
- Gustafsson, J.P., 2010. Visual MINTEQ thermodynamic databases in GWB format. <http://vminteq.lwr.kth.se> (accessed 08 April 2017).
- Klocke, D.J. and Hixson, A.N., 1972. Solubility of ferrous iron in aqueous ammoniacal solutions.

- Ind. Eng. Chem. Process Des. Develop. 11 (1), 141–146.
- Koyama, K., Tanaka, M. and Lee, J.-C., 2006. Copper leaching behavior from waste printed circuit board in ammoniacal alkaline solution. *Mater. Trans.* 47 (7), 1788–1792.
- McKibben, M.A., Tallant, B.A., del Angel, J.K., 2008. Kinetics of inorganic arsenopyrite oxidation in acidic aqueous solutions. *Appl. Geochem.* 23, 121–135.
- Oishi, T., Koyama, K., Alam, S., Tanaka, M., Lee, J.-C., 2007. Recovery of high purity copper cathode from printed circuit boards using ammoniacal sulfate or chloride solutions. *Hydrometallurgy* 89, 82–88.
- Schweigert, N., Acero, J.L., Von Gunten, U., Canonica, S., Zehnder, A.J.B. and Eggen, R.I.L., 2000. DNA degradation by the mixture of copper and catechol is caused by DNA-copper-hydroperoxo complexes, probably DNA-Cu(II)OOH. *Environ. Mol. Mutagen.* 36, 5–12.
- Schweigert, N., Zehnder, A.J.B. and Eggen, R.I.L., 2001. Chemical properties of catechols and their molecular modes of toxic action in cells, from microorganisms to mammals. *Environ. Microbiol.* 3 (2), 81–91.
- Speier, G., 1986. Copper-catalysed oxidation of catechols by dioxygen. *J. Mol. Catal.* 37, 259–267.
- Walker, F.P., Schreiber, M.E., Rimstidt, J.D., 2006. Kinetics of arsenopyrite oxidative dissolution by oxygen. *Geochim. Cosmochim. Acta* 70 (7), 1668–1676.
- Yu, Y., Zhu, Y., Williams-Jones, A.E., Gao, Z. and Li, D., 2004. A kinetic study of the oxidation of arsenopyrite in acidic solutions: implications for the environment. *Appl. Geochem.* 19, 435–444.
- Yu, Y., Zhu, Y., Gao, Z., Gammons, C.H. and Li, D., 2007. Rates of arsenopyrite oxidation by oxygen and Fe(III) at pH 1.8–12.6 and 15–45 °C. *Environ. Sci. Technol.* 41, 6460–6464.

**CHAPTER 4 – A NEW COMPLEX-BASED
CARRIER-MICROENCAPSULATION: THE DECOMPOSITION
MECHANISM OF ALUMINUM-CATECHOLATE COMPLEX, AND ITS
APPLICATION TO SUPPRESS ARSENOPYRITE OXIDATION**

4.1 Introduction

Previous CME studies using $[\text{Si}(\text{cat})_3]^{2-}$ and $[\text{Ti}(\text{cat})_3]^{2-}$ showed promising results but the use of these complexes have some drawbacks. Formation of $[\text{Si}(\text{cat})_3]^{2-}$ requires very high concentration of catechol (Bai et al., 2011; Öhman et al., 1991) while the decomposition of $[\text{Ti}(\text{cat})_3]^{2-}$ was sluggish and took at least 14 days of treatment to generate a coating thick enough to be effective (Park et al., 2018a). The high stability of $[\text{Ti}(\text{cat})_3]^{2-}$ could explain why its decomposition kinetics was slow, which delayed the formation of Ti-oxide coating. Although the coating formation by Ti-based CME could be accelerated at high temperature as described in the previous chapter, it has less practicality. To accelerate coating formation and improve the practicality of CME, thus, a new metal-catecholate complex that is easily synthesized and more readily decomposed is required as an alternative.

Al-catecholate complexes are promising candidates because according to Xu (2013), the cross-linking strength between metal and catechol weakens as oxidation state of the metal atom decreases. In other words, Al^{3+} -catecholate complexes are theoretically easier to decompose oxidatively compared with Ti^{4+} -catecholate complex, which could accelerate coating formation. Furthermore, AMD contains Al^{3+} at relatively high concentrations (100–500 mg/L) (Pozo et al., 2017; Wei et al., 2005), which makes it a good candidate material for the synthesis of Al-catecholate complexes. Although several studies on Al-catecholate complex formation, stability and speciation have been conducted (Cornard et al., 2010; Nurchi et al., 2009; Sikora and McBride, 1989), very few have been done to understand the electrochemical properties of these complexes. To date, only the study of Downard et al. (1996) on the voltammetry of Al-catecholate complexes in buffered solutions has been reported, so the electrochemical behaviors of these complexes remain unclear. Furthermore, the interactions between arsenopyrite and Al-catecholate complexes have not yet been reported.

In this chapter, Al-catecholate complexes were synthesized and their redox properties were investigated. Specifically, this chapter aims to: (1) elucidate the electrochemical properties of Al-catecholate complexes, (2) evaluate the effects of each complex species, leaching time, and complex concentration on the oxidation of arsenopyrite, (3) characterize changes in the surface of

mineral and the kind of coating formed after leaching, and (4) examine the short- and long-term stability of CME-treated arsenopyrite.

4.2 Materials and methods

4.2.1 Characterization of arsenopyrite

Arsenopyrite sample used in this study was obtained from Toroku mine, Miyazaki, Japan. It was crushed by a jaw crusher (BB 51, Retsch Inc., Germany) and then ground by a disk mill (RS 100, Retsch Inc., Germany) to obtain a size fraction between 106 and 150 μm in diameter. Details of arsenopyrite sample were addressed in section 2.2.1.

4.2.2 Synthesis of Al-catecholate complexes

Formation of Al-catecholate complexes were examined by titration. In this experiment, 1 mM Al^{3+} solutions were prepared from aluminum chloride hexahydrate ($\text{AlCl}_3 \cdot 6\text{H}_2\text{O}$, Wako Pure Chemical Industries, Ltd., Japan) with or without 3 mM catechol (1,2-dihydroxybenzene, Wako Pure Chemical Industries, Ltd., Japan). These solutions were magnetically stirred at 200 rpm for 10 min, and then titrated from pH 1 to 12 by adding dilute NaOH solution. Once the predetermined pH was reached, the solution was allowed to stabilize for 10 min before a 2 ml aliquot was collected. pH adjustment and aliquot collection were continued until pH 12. Each aliquot was filtered through 0.2 μm syringe-driven membrane filters (LMS Co., Ltd., Japan) to remove precipitates and polymerized organic molecules, and analyzed using an inductively coupled plasma atomic emission spectrometer (ICP-AES, ICPE-9820, Shimadzu Corporation, Japan) (detection limit of $\text{Al}^{3+} = 1 \mu\text{g/L}$, margin of error = $\pm 2\%$).

4.2.3 Ultraviolet-visible light spectrophotometric measurements

Speciation of Al-catecholate complexes is strongly pH dependent (Nurchi et al., 2009), so to identify the dominant species formed after synthesis, three types of solutions containing Al^{3+} and catechol were prepared: (1) 2 mM of Al^{3+} and 2 mM of catechol at pH 5, (2) 2 mM of Al^{3+} and 4 mM of catechol at pH 7, and (3) 2 mM of Al^{3+} and 6 mM of catechol at pH 10, all of which contain 0.1 M NaCl (Wako Pure Chemical Industries, Ltd., Japan) to maintain a constant ionic strength. These solutions were immediately measured by UV-vis light spectrophotometry (V-630, Jasco Analytical Instruments, Japan) in a single-crystal quartz cell between 250 and 500 nm. In addition, catechol

solutions (2 mM at pH 5, 4 mM at pH 7 and 6 mM at pH 10 with 0.1 M NaCl) were measured by UV-vis light spectrophotometry to identify background signals of “free” catechol in the spectra.

4.2.4 Electrochemical studies

To investigate the electrochemical behaviors of each Al-catecholate complex species, cyclic voltammetry (CV) measurements were carried out using solutions prepared in an identical way as those measured by UV-vis spectrophotometry. For CV measurements, an SI 1280B electrochemical measurement unit (Solartron Instruments, UK) with a conventional three-electrode system was used. Platinum (Pt) electrode, Pt wire, and Ag/AgCl electrode filled with 3.3 M NaCl were used as working, counter, and reference electrodes, respectively. Likewise, CV measurements of solutions containing only catechol at pH 5, 7 and 10 were conducted. All solutions were prepared with 0.1 M NaCl as supporting electrolyte, equilibrated at 25 °C and deoxygenated by N₂ purging. All CV measurements started after equilibration at the open circuit potential (OCP), and the sweep direction was towards increasingly positive potentials first. The voltammograms were recorded between 0.0 and +1.0 V vs. SHE at a scan rate of 5 mV/s for 5 cycles.

4.2.5 Batch leaching experiments

Before the leaching experiments, arsenopyrite sample was washed to remove slime coating and any oxidized layer formed during sample preparation and storage. The washing procedures are as follows: ultrasonic cleaning in methanol, acid washing (1.8 M HNO₃), triple rinsing with DI water (18.2 MΩ·cm), dewatering with acetone, and drying in a vacuum desiccator (McKibben et al., 2008).

For the batch leaching experiments, 1 g of washed sample and 10 ml of prepared solution (i.e., control, Al³⁺ only, catechol only, and Al-catechol solution) were put in a 50 ml Erlenmeyer flask and then shaken in a constant temperature water bath (25°C) at 120 strokes/min under oxic conditions. It is important to note that control in this study refers to solutions containing equivalent amounts of Cl⁻ as the other cases. The effects of Al-catechol complexes on the oxidation of arsenopyrite were investigated under various pH, treatment time and concentrations of Al-catecholate complexes. Total chloride concentration, [Cl⁻]_{tot}, was maintained in all experiments by adding NaCl to normalize the effects of Cl⁻ ion on sulfide oxidation. Some experiments were done in triplicates to ascertain that the differences observed were statistically significant. At predetermined time intervals, suspensions were collected and their pH as well as redox potential (Eh) were measured. After this, the suspensions were filtered through 0.2 μm membrane filters and the filtrates were analyzed by

ICP-AES. Meanwhile, the residues were collected, thoroughly washed with DI water, dried in a vacuum oven at 40 °C for 24 h and analyzed by SEM-EDX, DRIFTS, and X-ray photoelectron spectroscopy (XPS, Axis-His, Shimadzu/Kratos Corporation, Japan). XPS analysis was conducted using a monochromatic Al K α X-ray (1486.7 eV) and operated at 140 W (14 kV, 10 mA) under ultrahigh vacuum condition (8.0×10^{-8} torr). The binding energies of photoelectrons were calibrated using C 1s (285.0 eV) as a reference.

4.2.6 Acidic oxalate extraction

Acidic oxalate extraction was conducted to estimate the relative amounts of Al-oxyhydroxide phases in coatings formed on arsenopyrite after Al-based CME treatment (McKeague and Day, 1965). For this, 0.1 g of leaching residues were mixed with 10 ml of extractant, a 1:0.75 mixture of 0.23 M ammonium oxalate monohydrate (C₂H₁₀N₂O₅, Junsei Chemical Co., Ltd., Japan) and 0.28 M oxalic acid (C₂H₂O₄, Junsei Chemical Co., Ltd., Japan), and shaken in a constant temperature water bath (25°C) at 150 strokes/min for 6 h. The suspensions were then centrifuged at 3500 rpm for 20 min to collect the supernatant, which was filtered through 0.2 μ m membrane filter and analyzed by ICP-AES.

4.2.7 Chronoamperometry

The working electrode and protocols used for the chronoamperometry measurements are identical to those described in section 2.2.8, but the pretreatments used for the arsenopyrite electrode were different. For the pretreatment, polished mineral electrode was immersed in solution containing either 45 mM NaCl (control) or 15 mM [Al(cat)]⁺ and magnetically stirred at 200 rpm for 3 days. After this, the pretreated electrode was thoroughly washed with DI water, dried under ambient conditions for 1 h and used for chronoamperometric measurements that apply the potential at 0.0 V vs. SHE for cathodic polarization and at +0.7 V vs. SHE for anodic polarization.

4.2.8 Weathering cell test

The weathering cell test method was based on the procedure used by Bouzahzah et al. (2014); that is, the samples treated with control and Al-based CME were placed on 50-mm diameter Büchner funnels with a 0.2 μ m membrane filter connected to a centrifuge tube (Figure 4-1), and a 7-day leaching cycle was followed consisting of leaching with DI water on the 1st day, followed by 2 days of exposure to ambient conditions, then leaching again on the 4th day followed by an additional 3

days of exposure to the air. The amount of sample placed in the weathering cells and the volume of DI water poured were 3 g and 10 ml, respectively. The samples were leached for 3 h at a fixed time of the day. After this, the leachates were collected using a vacuum pump and then analyzed by ICP-AES.

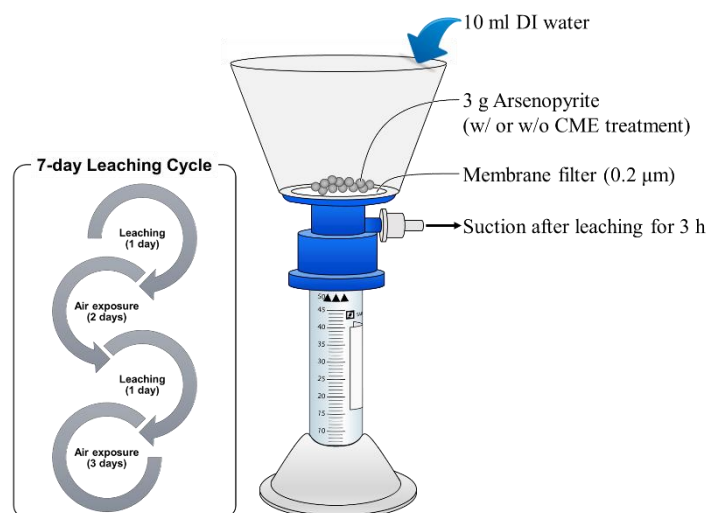


Figure 4-1. The schematic diagram of the setup for weathering cell tests.

4.2.9 Regeneration of used organic carrier

Catechol was pre-oxidized under ambient conditions to generate quinone, an oxidation product of catechol. One hundred milliliters of 1 mM catechol solution was prepared at pH 10 and magnetically stirred at 200 rpm because under alkaline conditions, the oxidation rate of catechol by O_2 is known to be accelerated (Yang et al., 2014). At pre-determined time intervals, 20 ml of aliquots were collected and used for linear sweep voltammetry (LSV) and UV-vis spectroscopic measurements. The LSVs were measured from OCP to 1.0 V vs. SHE under N_2 atmosphere. For the regeneration of oxidized catechol prepared by pre-oxidation of catechol solution for 3 days, electrolysis was applied by applying a fixed potential at 0.0 V vs. SHE where quinone could be reduced back to catechol. After electrolysis for 1 h, LSV was again measured to identify the changes in the amounts of reduced products.

4.3 Results and discussion

4.3.1 Speciation of Al-catecholate complexes with pH

As shown in Figures 4-2a and b, solubility of Al in the absence and presence of catechol were significantly different. Without catechol, dissolved Al could only exist at $\text{pH} < 4.5$ and $\text{pH} > 8.0$ (Figure 4-2c), which are in good agreement with predictions of the equilibrium log activity-pH diagram (Figure 4-3). With catechol, however, the solubility of Al increased especially between pH 4.5 and 8.0. Thermodynamic calculations suggest that catechol limited the precipitation of Al^{3+} by forming two Al-catecholate complexes: mono-catecholate ($[\text{Al}(\text{cat})(\text{H}_2\text{O})_4]^+$) and bis-catecholate ($[\text{Al}(\text{cat})_2(\text{H}_2\text{O})_2]^-$) (Figure 4-2b). For simplification, $[\text{Al}(\text{cat})(\text{H}_2\text{O})_4]^+$ and $[\text{Al}(\text{cat})_2(\text{H}_2\text{O})_2]^-$ will be denoted as $[\text{Al}(\text{cat})]^+$ and $[\text{Al}(\text{cat})_2]^-$, respectively, through the remainder of the paper. Theoretical curves calculated by the speciation diagrams were also in good agreement with experimental data (Figure 4-2c), indicating that speciation diagrams could reliably predict the pH of formation of each complex. As illustrated in Figure 4-2b, there are three Al-catecholate complexes formed in aqueous solution depending on the pH: (1) $[\text{Al}(\text{cat})]^+$ between 4.7 and 5.5, (2) $[\text{Al}(\text{cat})_2]^-$ between 5.5 and 8.5, and (3) tris-catecholate ($[\text{Al}(\text{cat})_3]^{3-}$) between 8.5 and 14.0. To validate the formation of these complexes, Al-catechol solutions at pH 5, 7 and 10 were prepared and analyzed by UV-vis spectrophotometer (Figure 4-2d). The spectra of Al-catechol solutions show three distinct peaks around 282 nm at pH 5, 289 nm at pH 7 and 297 nm at pH 10. Absorbance and Al concentration as functions of molar ratio of Al^{3+} and catechol (Figure 4-4) suggest that the complex formed at pH 5, 7 and 10 were $[\text{Al}(\text{cat})]^+$, $[\text{Al}(\text{cat})_2]^-$ and $[\text{Al}(\text{cat})_3]^{3-}$, respectively, which are in good agreement with the speciation diagram (Figure 4-2b). Based on these results, Al-catechol solutions were prepared at pH 5, 7 and 10 to synthesize each complex separately.

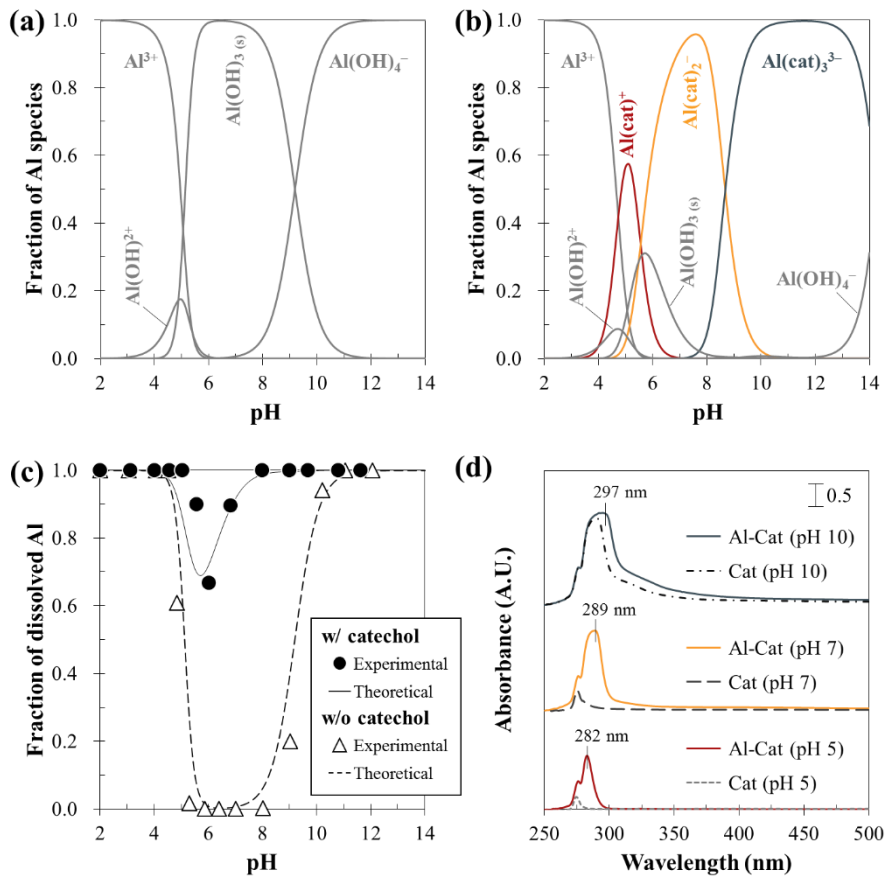


Figure 4-2. Characterization of Al-catecholate complexes: speciation diagram of (a) Al³⁺ only ([Al³⁺]: 1 mM) and (b) Al³⁺-catechol system ([Al³⁺]: 1 mM, [H₂Cat]: 3 mM) (Nurchi et al., 2009), (c) solubility of Al³⁺ with pH in the absence and presence of catechol, and (d) UV-vis spectra of catechol only and Al-catechol solution at pH 5, 7 and 10.

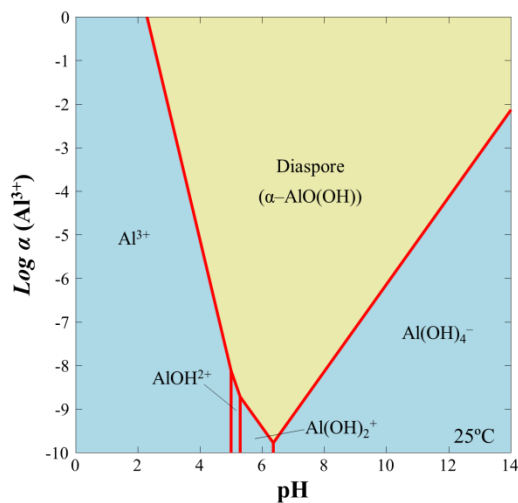


Figure 4-3. Log activity-pH predominance diagram of Al³⁺ at 25 °C and 1.013 bar created using the Geochemist's Workbench[®] with MINTEQA2 database (Bethke, 1992; Gustafsson, 2010).

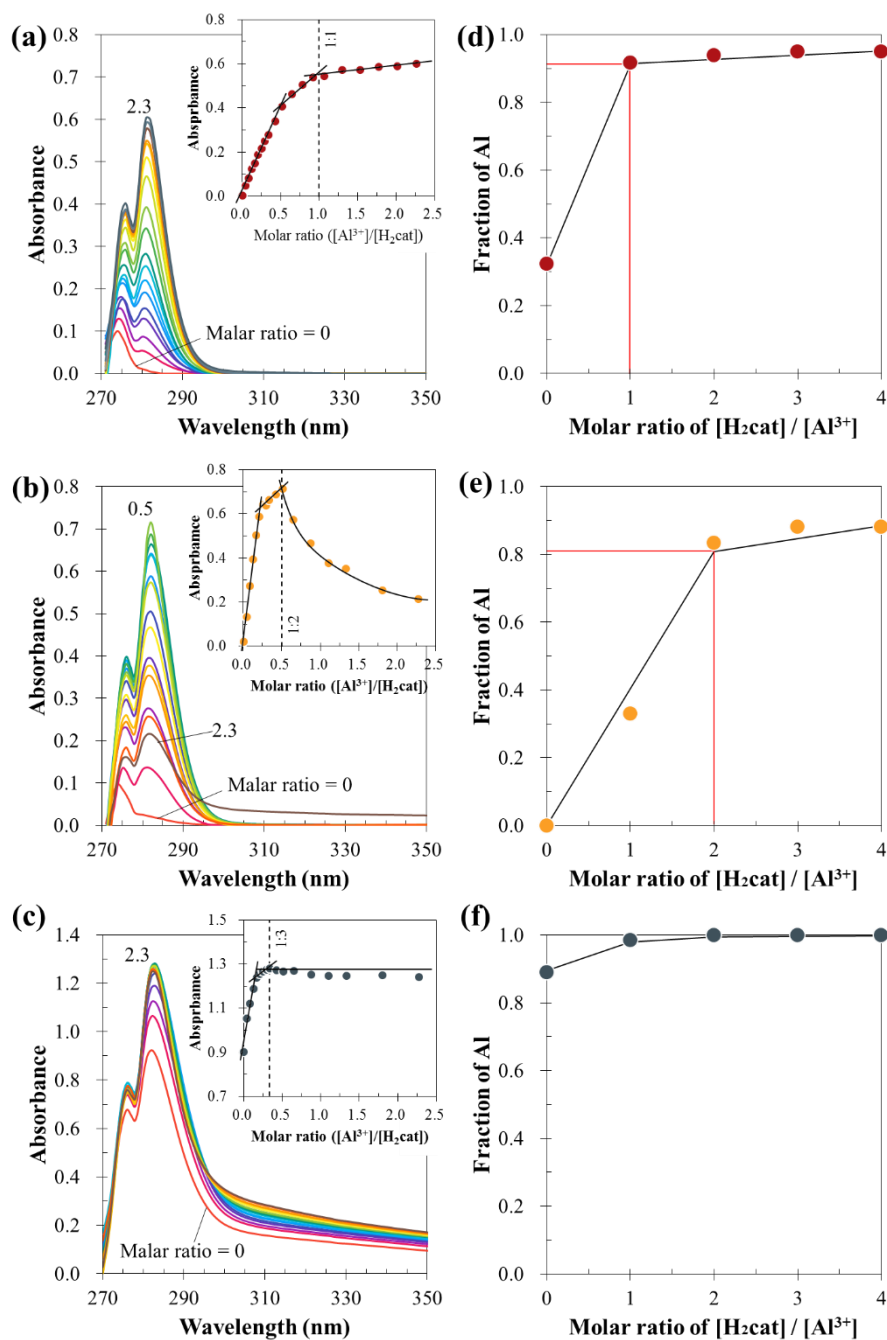


Figure 4-4. Characterization of Al-catechol complexes: UV-vis spectra of catechol solutions with varying Al^{3+} molar ratio (0.0 to 2.3) at pH 5 (a), at pH 7 (b) and at pH 10 (c), and Al concentration as a function of molar ratio of $[\text{H}_2\text{cat}]/[\text{Al}^{3+}]$ at pH 5 (d), at pH 7 (e) and at pH 10 (f). Note that the insets in Figures 4-4a–c are plots of maximum absorbance vs. $[\text{Al}^{3+}]/[\text{H}_2\text{cat}]$ molar ratio.

4.3.2 Electrochemical properties of Al-catecholate complexes

Cyclic voltammetry was carried out in solutions containing either “free” catechol or Al-catecholate complexes at pH 5, 7 and 10 to elucidate the decomposition behaviors of the three complex species. As illustrated in Figure 4-5c, “free” catechol at pH 5 and 7 only exhibited one anodic peak at ca. 0.78 V (A_1^*), the potential at which catechol (1,2-dihydroxybenzene, $C_6H_4(OH)_2$) is oxidized to orthoquinone (1,2-benzoquinone, $C_6H_4O_2$) (Eq. (4-1); Danilewicz, 2012). At pH 10, the additional peak (A_2^*) at 0.23 V could be attributed to the oxidation of semiquinone radical generated during sample preparation (Eq (4-2)), the enhanced formation and stability of which have been documented by other authors especially under alkaline conditions (Kalyanaraman et al., 1985; Yang et al., 2014).



The cyclic voltammogram of Al-catechol solution at pH 5 shows one broad anodic peak (A_1) centered at ca. 0.73 V in the first cycle (Figures 4-5a and b). Compared with “free” catechol at the same pH, A_1 is shifted to a slightly lower potential, suggesting that this peak could be attributed to the oxidative decomposition of $[Al(cat)]^+$ to Al^{3+} and orthoquinone (Eq. (4-3)). In the succeeding cathodic sweep, one peak appeared at around 0.4 V, indicating that orthoquinone, the oxidation product from the previous anodic sweep, was reduced back to catechol as illustrated in Eq. (4-1) (Danilewicz, 2012; Park et al., 2018a; Yang et al., 2014). Moreover, this cathodic reaction was also observed in the voltammograms of Al-catechol solutions at pH 7 and 10. For Al-catechol solution at pH 7, two anodic peaks were clearly observed: (1) A_2 due to the oxidation of $[Al(cat)_2]^-$ to $[Al(cat)]^+$ and orthoquinone (Eq. (4-4)), and (2) A_1 that is assigned earlier to the oxidation of $[Al(cat)]^+$. At pH 10, three distinct peaks appeared in sequence at around 0.30, 0.45 and 0.73 V during the first cycle. These consecutive peaks (i.e., A_1 , A_2 and A_3) could be attributed to the 3-step sequential decomposition of $[Al(cat)_3]^{3-}$ complex; that is, $[Al(cat)_3]^{3-} \rightarrow [Al(cat)_2]^- \rightarrow [Al(cat)]^+ \rightarrow Al^{3+}$ (Eqs. (4-3) – (4-5)). It is interesting to note that all anodic peaks observed during the first cycle gradually decreased in the succeeding cycles regardless of the pH, which means that the oxidative decomposition of Al-catecholate complexes is irreversible.

Our results are considerably different from those reported by Downard et al. (1996). According to this earlier work, $[Al(cat)]^+$ was not electroactive while $[Al(cat)_2]^-$ and $[Al(cat)_3]^{3-}$ underwent oxidative decomposition but only one of the coordinated catechol molecules was electroactive.

These differences could be explained by the use of buffers containing ammonium (NH_4^+) and acetate (CH_3COO^-) ions by these authors in their experiments. Both of these ions could interfere during electrochemical measurements and complex formation; that is, NH_4^+ promotes catechol precipitation (Saiz-Poseu et al., 2013) while CH_3COO^- forms several complexes with Al^{3+} (de Noronha and Guimarães, 2007).

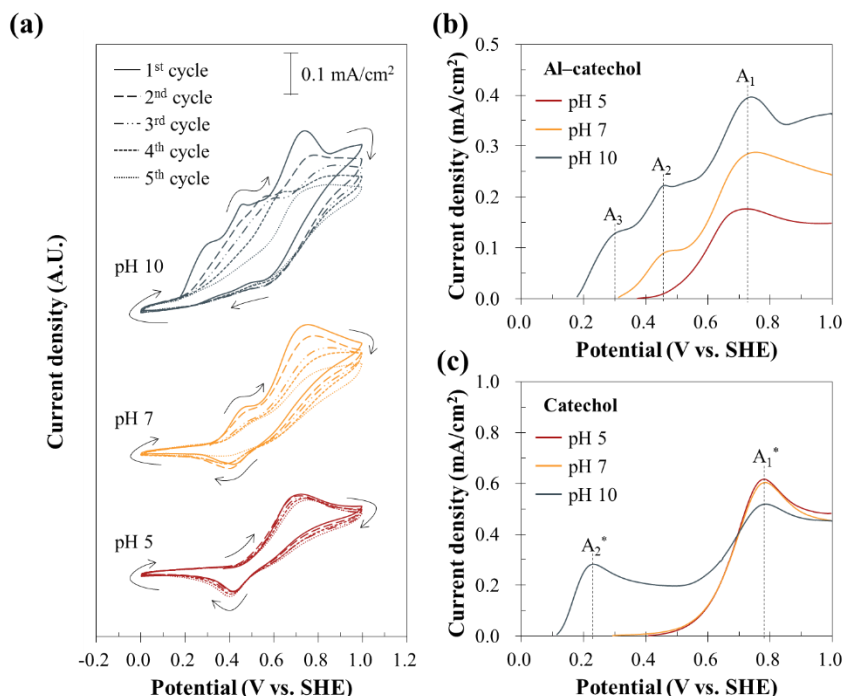
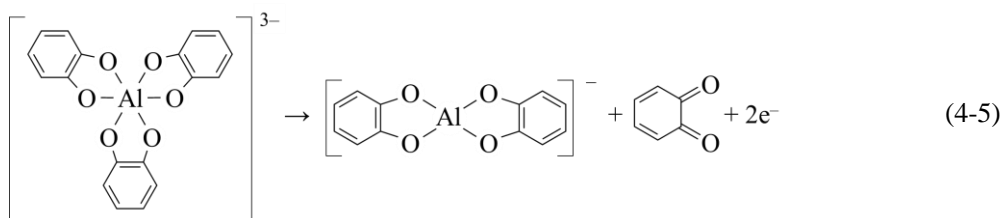
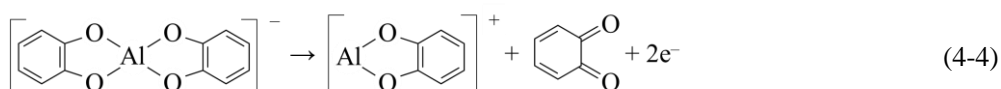


Figure 4-5. (a) Cyclic voltammograms of Al-catechol solutions at pH 5, 7 and 10, and first anodic sweeps of (b) Al-catecholate complexes and (c) catechol at pH 5, 7 and 10. Note that arrows denote the sweep direction.

4.3.3 Al-based CME to suppress the oxidations of pyrite and arsenopyrite

4.3.3.1 Effects of Al-catecholate complexes species

Effects of the three Al-catecholate complexes on arsenopyrite oxidation are illustrated in Figure 4-6. Substantial changes in pH and Eh in arsenopyrite suspensions were apparent after 7 days, regardless of the complex species used. Previous studies have shown that the oxidations of sulfide minerals like arsenopyrite and pyrite are strongly pH dependent (Bonnissel-Gissing et al., 1998; Williamson and Rimstidt, 1994), so experiments using NaCl solutions with identical ionic strengths at pH 5, 7 and 10 were performed. As shown in Figure 4-6c (open bars), similar concentrations of oxidation products regardless of the pH were observed, which suggest that the effects of pH on the leaching of arsenopyrite were negligible under the conditions of this study. In other words, differences in concentrations of oxidation products in the leaching experiment could be attributed to the effects of complex species and not the pH.

The concentrations of dissolved Fe, As and S released from arsenopyrite were lower in the presence of $[\text{Al}(\text{cat})]^+$ compared with those of $[\text{Al}(\text{cat})_2]^-$ and $[\text{Al}(\text{cat})_3]^{3-}$ (Figure 4-6c). Dissolved S concentration, an indicator of the extent of sulfide oxidation (Bonnissel-Gissing et al., 1998), was

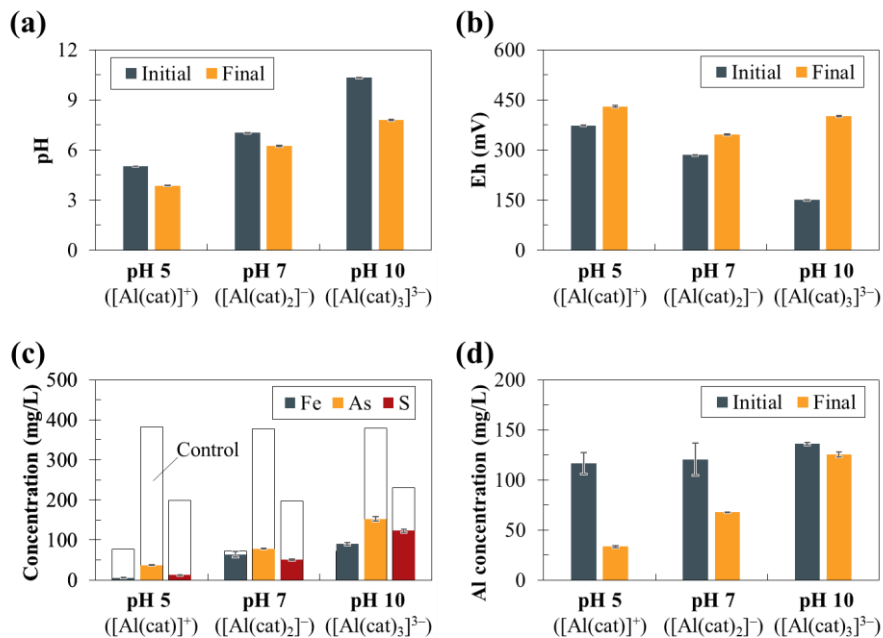


Figure 4-6. Effects of Al-catecholate complexes on the oxidation of arsenopyrite: evolution of (a) pH and (b) Eh, and changes in (c) dissolved Fe, As and S concentrations, (d) dissolved Al concentration. Note: $[\text{Al}^{3+}] = 5 \text{ mM}$; $[\text{H}_2\text{Cat}] = 15 \text{ mM}$; $[\text{Cl}^-]_{\text{tot}} = 15 \text{ mM}$; leaching time = 7 days; pH = 5, 7 and 10 for $[\text{Al}(\text{cat})]^+$, $[\text{Al}(\text{cat})_2]^-$ and $[\text{Al}(\text{cat})_3]^{3-}$, respectively.

13 mg/L in $[\text{Al}(\text{cat})]^+$, which was around four- and nine-fold lower than those in $[\text{Al}(\text{cat})_2]^-$ and $[\text{Al}(\text{cat})_3]^{3-}$, respectively. The more extensive oxidation of arsenopyrite in $[\text{Al}(\text{cat})_3]^{3-}$ was consistent with the higher Eh in this case compared with the other cases (Figure 4-6b). These results also coincided well with the order of decline in dissolved Al: $[\text{Al}(\text{cat})]^+ > [\text{Al}(\text{cat})_2]^- > [\text{Al}(\text{cat})_3]^{3-}$ (Figure 4-6d). This indicates that Al-catecholate complex becomes more difficult to decompose as the number of ligands coordinated with Al^{3+} increases.

4.3.3.2 Effects of coexisting components and $[\text{Al}(\text{cat})]^+$ with time

Although $[\text{Al}(\text{cat})]^+$ is the dominant species in Al-catechol solution at pH 5, “free” Al^{3+} and “free” catechol still coexisted with $[\text{Al}(\text{cat})]^+$ as shown in the speciation diagram (Figure 4-2b). To better understand the suppressive effects of $[\text{Al}(\text{cat})]^+$, leaching tests of arsenopyrite in control (DI water with 15 mM NaCl), Al^{3+} only, catechol only and Al-catechol solution at pH 5 were carried out as a function of time.

The effects of “free” Al^{3+} and catechol on the oxidation of arsenopyrite were significant as illustrated in Figure 4-7. In the control, arsenopyrite was rapidly oxidized and after 10 days, the pH dramatically dropped down to 2.5 (Figure 4-7a) that was accompanied by the release of 138 mg/L of Fe, 527 mg/L of As, and 346 mg/L of S (Figures 4-7c–e). However, the decrease in pH and release of Fe, As and S were limited for the first 3 days in Al^{3+} only solution (Figures 4-7a, c–e). This initial suppressive effect was most likely related to the rapid decrease of dissolved Al from 44 mg/L to 4.3 mg/L after just 1 day (Figure 4-7f). SEM-EDX analysis of arsenopyrite leached in Al^{3+} only solution showed that precipitates composed of Fe, As, Al and O were formed, which means that a portion of dissolved Fe and As were most likely coprecipitated with Al^{3+} ions (Figure 4-8). Coprecipitation of As with Fe or Al is thermodynamically favorable as illustrated by the equilibrium log activity-pH diagram of Fe^{3+} - AsO_4^{3-} - SO_4^{2-} - Al^{3+} - H_2O system based on actual solute concentrations (Figure 4-9). This deduction is also consistent with several studies, reporting that arsenic species (i.e., As^{3+} and As^{5+}) could be immobilized in the presence of Fe and Al via coprecipitation and/or adsorption reactions (Jia et al., 2012; Violante et al., 2009).

The suppressive effect of catechol on the oxidation of arsenopyrite were stronger than that of Al^{3+} (Figure 4-7). This effect could be explained by three possible mechanisms: (1) adsorption of catechol on mineral surface that limited contact with oxidants (Belzile et al., 1997; Lalvani and Deneve, 1990), (2) consumption of DO by catechol and its complexation reactions with Fe^{3+} that lowered the availability of oxidants (Ačai et al., 2009; Pracht et al., 2001), and (3) oxidative decomposition of catechol that directly donated electrons to mineral (Figure 4-5c). Although catechol could suppress the oxidation of arsenopyrite, this suppressive effect was only temporary as

previously elucidated in Chapter 2.

[Al(cat)]⁺ effectively suppressed the oxidation of arsenopyrite as illustrated by the considerably lower leaching of Fe, As, and S than those of the control, Al³⁺ and catechol only solutions (Figure 4-7). It is interesting to note that concentrations of Fe, As, and S did not change after 1 day, which indicates that the suppressive effect of [Al(cat)]⁺ was quite rapid. Moreover, the pH was highest in [Al(cat)]⁺ solution while Eh was lowest, which further support the suppression of arsenopyrite oxidation by this complex (Figure 4-7). During the treatment of arsenopyrite with [Al(cat)]⁺, Al³⁺ concentration rapidly decreased from around 130 to 53 mg/L after just 1 day and reached apparent equilibrium in 3 days. In comparison with Ti-based CME (Chapter 2), Al mono-catecholate complex could dramatically accelerate the formation of protective coatings on arsenopyrite surface. SEM-EDX analysis of leaching residue after 10 days detected signals of Al and O on the surface of arsenopyrite, which indicate that it was probably covered with Al–O containing coatings (Figures 4-10). To characterize the nature of this coating, the leaching residues were analyzed by DRIFTS, a surface sensitive technique able to identify molecular coordination of ions and molecules in the structure of minerals including very thin oxidation products (Carlson et al., 2002; Evangelou, 1995; Tabelin et al., 2017). As illustrated in Figures 4-11, arsenopyrite leached in [Al(cat)]⁺ showed new absorption peaks representing vibrations of Al=O bending, angle bending/deformation of O–Al=O and AlO₆ octahedral group in Al-oxyhydroxide, indicating that the coating formed on this mineral is composed predominantly of Al-oxyhydroxide phases (Table 4-1). The samples treated with control and [Al(cat)]⁺ were further analyzed by XPS. As shown in Figure 4-12a, XPS spectrum (Al 2p) of the control has no distinct peak while the spectrum of CME-treated arsenopyrite shows a broad peak centered at ca. 75 eV. Deconvolution of this peak using a Gaussian-Lorentzian function indicates that it has two Al 2p transitions at 74.6 and 75.3 eV, respectively. According to Kloprogge et al. (2006), the former is associated with bayerite (γ -Al(OH)₃) and the latter is most likely its amorphous phase. XPS spectrum (O 1s) of CME-treated arsenopyrite (Figure 4-12b) shows two O 1s transitions at ca. 532.1 and 533.1 eV, respectively, most likely attributed to the hydroxyl groups in the crystal structure of bayerite (i.e., Al–O–H) and absorbed water on the surface (H–O–H) (Kloprogge et al., 2006). In contrast, XPS spectrum (O 1s) of the control shows an additional peak of O(–II), indicating that arsenopyrite oxidation has proceeded to much greater extent compared with CME-treated arsenopyrite (Nesbitt et al., 1995). This means that the suppression of arsenopyrite oxidation by [Al(cat)]⁺ occurred via two pathways: (1) electron donating effect of this complex as discussed previously, and (2) formation of protective coatings. The former dominated in the short-term but was likely temporary similar to catechol whereas the latter resulted in the prolonged passivation of arsenopyrite.

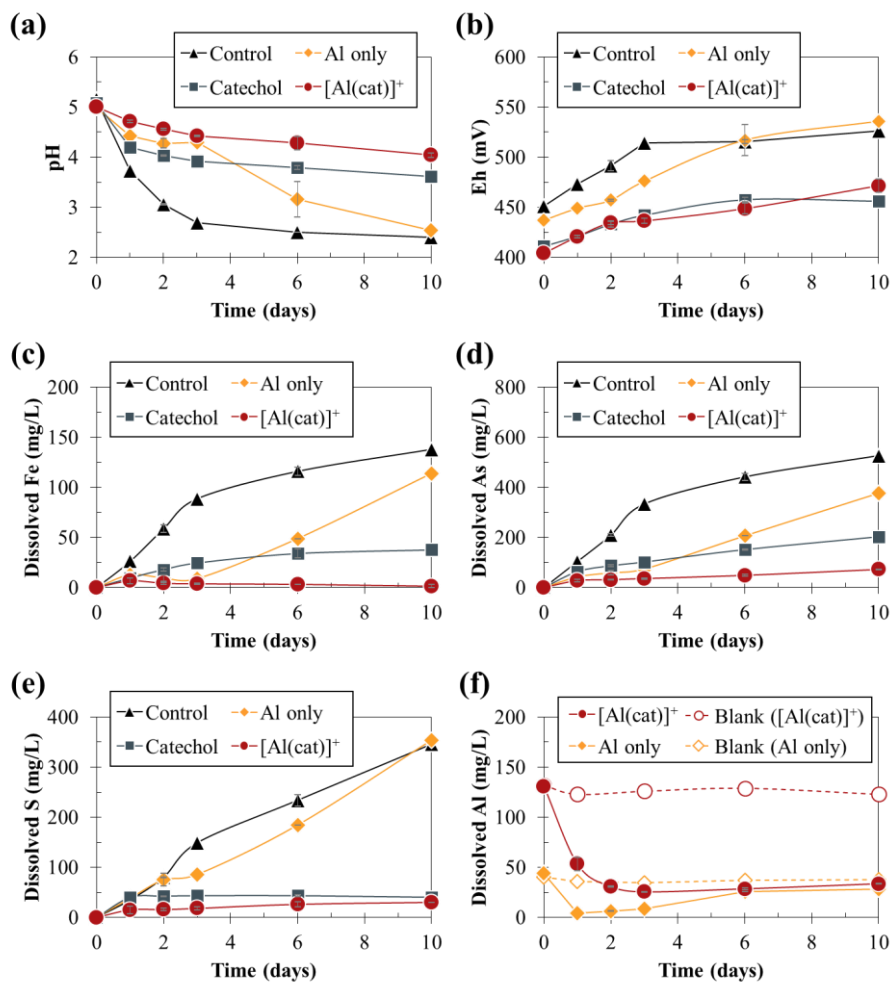


Figure 4-7. Effects of time on the oxidation of arsenopyrite: evolution of leachate (a) pH and (b) Eh, and changes in the concentrations of (c) Fe, (d) As, (e) S and (f) Al. Note: Control, Al only ($[Al^{3+}] = 5 \text{ mM}$), Catechol ($[H_2Cat] = 5 \text{ mM}$), $[Al(cat)]^+$ ($[Al^{3+}] = 5 \text{ mM}$ and $[H_2Cat] = 5 \text{ mM}$); $[Cl^-]_{tot} = 15 \text{ mM}$; pH = 5.

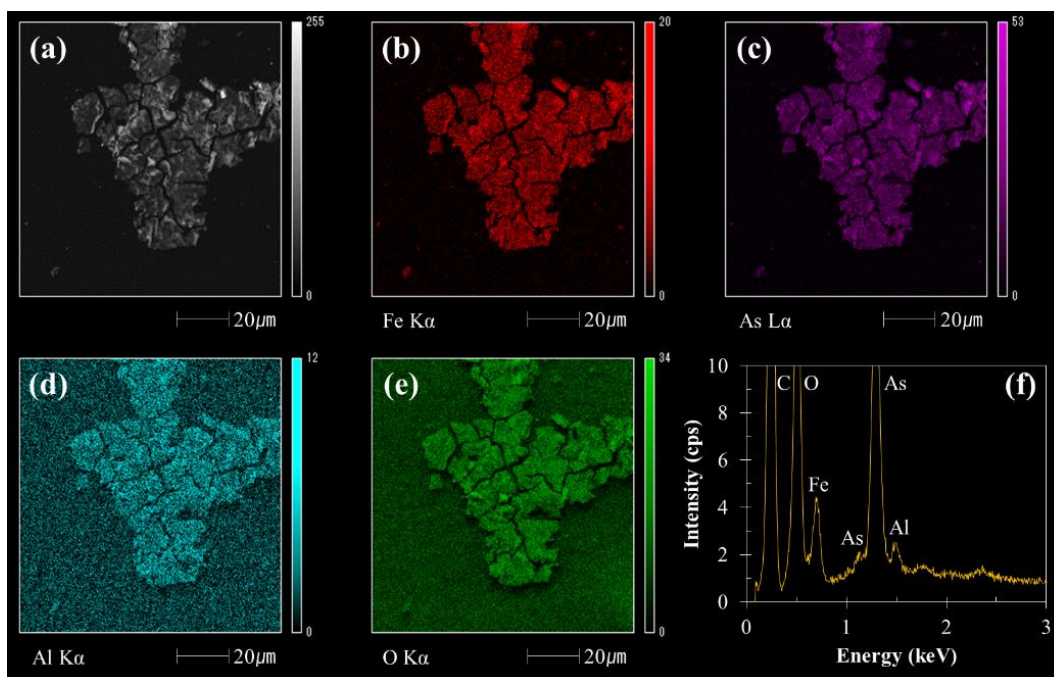


Figure 4-8. SEM-EDX analysis of precipitates from the leaching of arsenopyrite in Al^{3+} only solution for 10 day: (a) SEM photomicrograph, elemental maps of (b) Fe, (c) As, (d) Al and (e) O, and (f) energy dispersive X-ray spectrum of the scanned area.

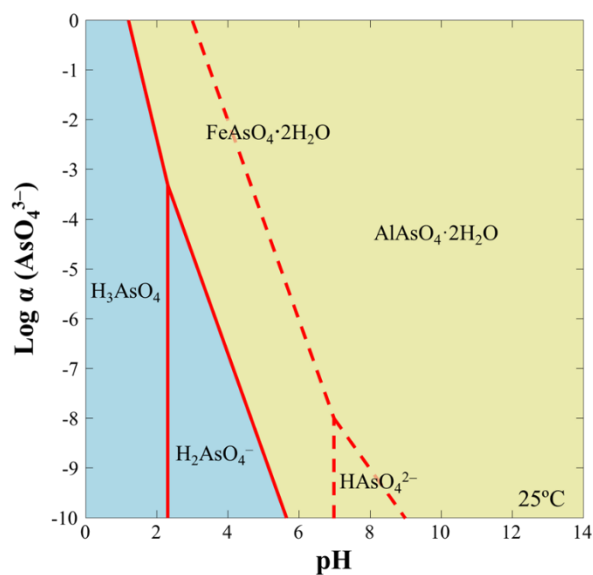


Figure 4-9. Log activity-pH predominance diagram of AsO_4^{3-} at 25 °C and 1.013 bar in the presence of Fe^{3+} ($a = 10^{-2.7}$), Al^{3+} ($a = 10^{-3.0}$) and SO_4^{2-} ($a = 10^{-2.5}$) created using the Geochemist's Workbench® with MINTEQA2 database (Bethke, 1992; Gustafsson, 2010).

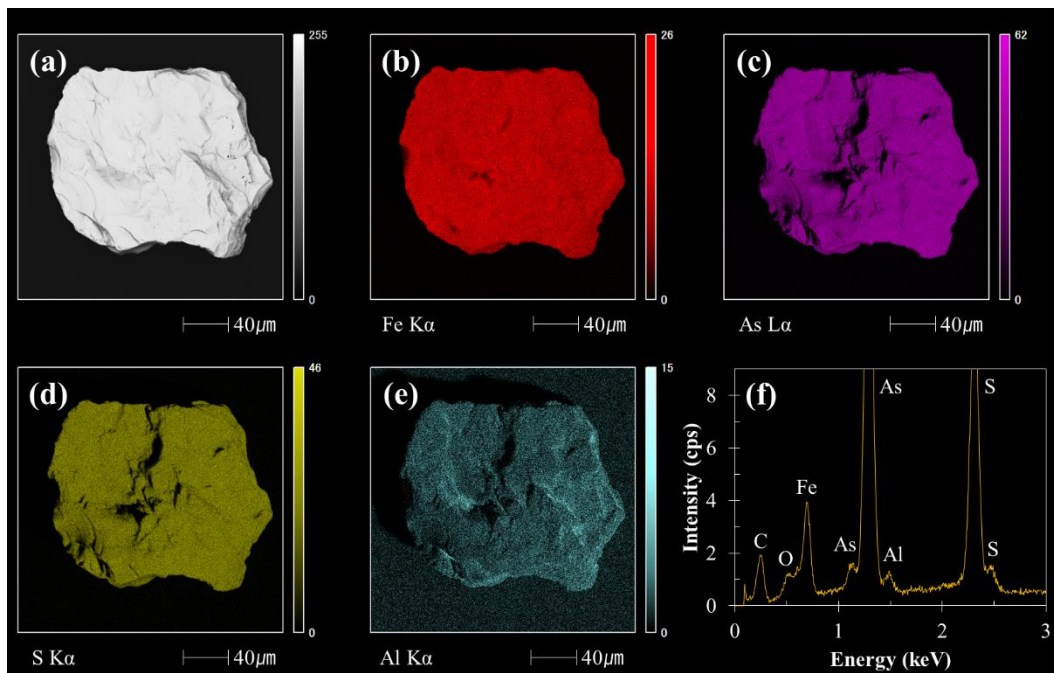


Figure 4-10. Characterization of arsenopyrite after treatment in $[\text{Al}(\text{cat})]^+$ solution for 10 day: (a) SEM photomicrograph, elemental maps of (b) Fe, (c) As, (d) S and (e) Al, (f) energy dispersive X-ray spectrum of the scanned area.

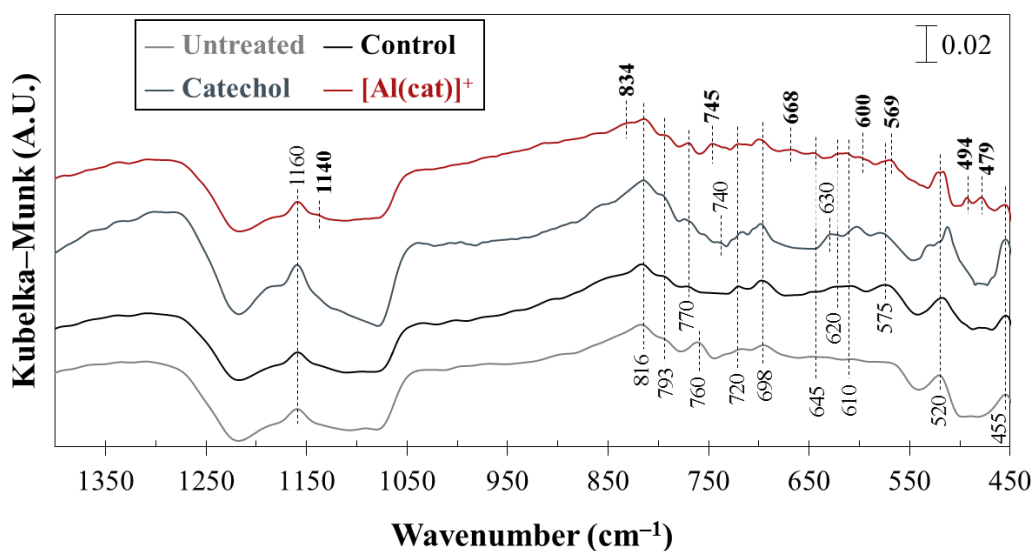


Figure 4-11. DRIFT spectra of arsenopyrite before and after leaching.

Table 4-1. Assignments of absorption peaks in DRIFTS spectra of untreated arsenopyrite, and those leached in DI water, catechol and [Al(cat)]⁺ for 10 days.

Wavenumber (cm ⁻¹)	Assignment	References
1160	Sulfate coordinated with Fe ³⁺	Carlson et al., 2002; Tabelin et al., 2017
1140	O–H bending	Ram, 2001; Musić, 1999
834, 745	Al=O bending vibrations	Ram, 2001; Musić, 1999
816	Si stretching (Si–O–Si)	Lippincott et al., 1958
793	Vibration of arsenate (O–As–O)	Achimovičová and Baláž, 2005; Monte et al., 2002
770, 760	O–H in-plane bending vibrations	Raade et al., 1984
740	C–H out-of-plane bending vibration	McBride and Wesselink, 1988
720	Stretching band of O–H coordinated with Fe ³⁺	Carlson et al., 2002; Tabelin et al., 2017
698	O–H stretching	Carlson et al., 2002
668, 600	Angle bending vibrations of AlO(OH)	Ram, 2001; Musić, 1999
645, 620, 610	Vibrations of sulfoxy anion	Evangelou, 1995; Tabelin et al. 2017
630	Benzene ring bending vibration (in-plane)	McBride and Wesselink, 1988
575, 520	Fe–O bending vibrations	Tabelin et al. 2017
569, 494, 479	Angle deformations of AlO(OH)	Ram, 2001; Musić, 1999
455	Vibration of Fe–As	Achimovičová and Baláž, 2005; Monte et al., 2002

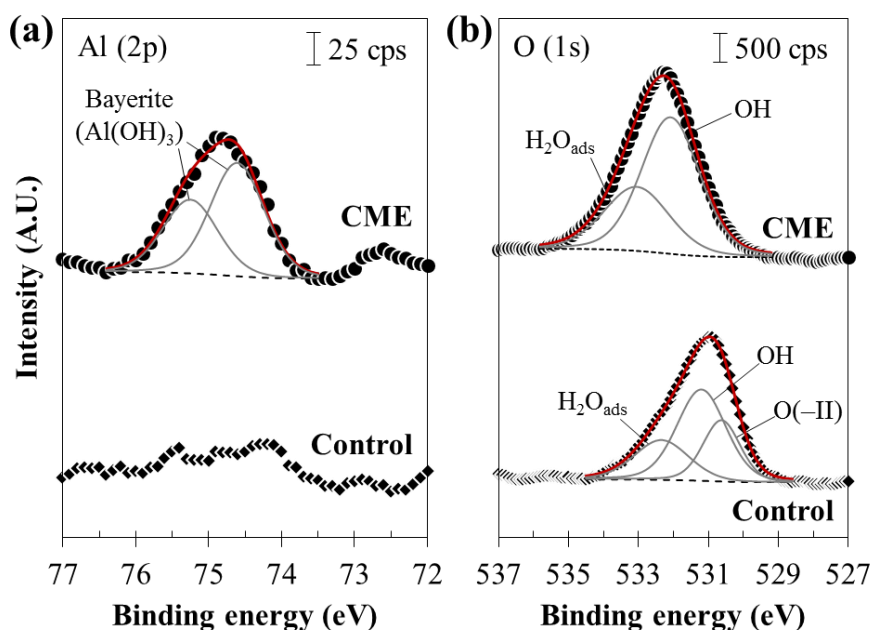


Figure 4-12. XPS spectra of arsenopyrite treated with control and CME for (a) Al 2p and (b) O 1s.

4.3.3.3 Effects of $[Al(cat)]^+$ concentrations

Figure 4-13a shows the evolution of leachate pH before and after leaching with various concentrations of $[Al(cat)]^+$ (0–15 mM). In the absence of $[Al(cat)]^+$, leachate pH substantially decreased to 2.3 while it was maintained at around pH 4.0 with $[Al(cat)]^+$, indirectly indicating that $[Al(cat)]^+$ limited the extent of arsenopyrite oxidation. The leaching of Fe, As, and S decreased as the concentration of $[Al(cat)]^+$ increased (Figure 4-13b), which means that suppression of arsenopyrite oxidation becomes stronger at higher concentrations of $[Al(cat)]^+$. Precipitation of dissolved Al was also more substantial as the concentration of $[Al(cat)]^+$ increased (Figure 4-13c), implying that the formation of Al-oxyhydroxide coating was probably improved and became more extensive at higher $[Al(cat)]^+$ concentration. To verify this deduction, acidic oxalate extractions of arsenopyrite treated with various $[Al(cat)]^+$ concentrations (0–15 mM) were carried out. As illustrated in Figure 4-13d, the relative abundance of Al-oxyhydroxide phases formed on arsenopyrite were proportional to the $[Al(cat)]^+$ concentration. These results are in good agreement with the leaching trend of arsenopyrite shown in Figure 4-13b, which further supported our deduction of improved coating formation at higher $[Al(cat)]^+$ concentration.

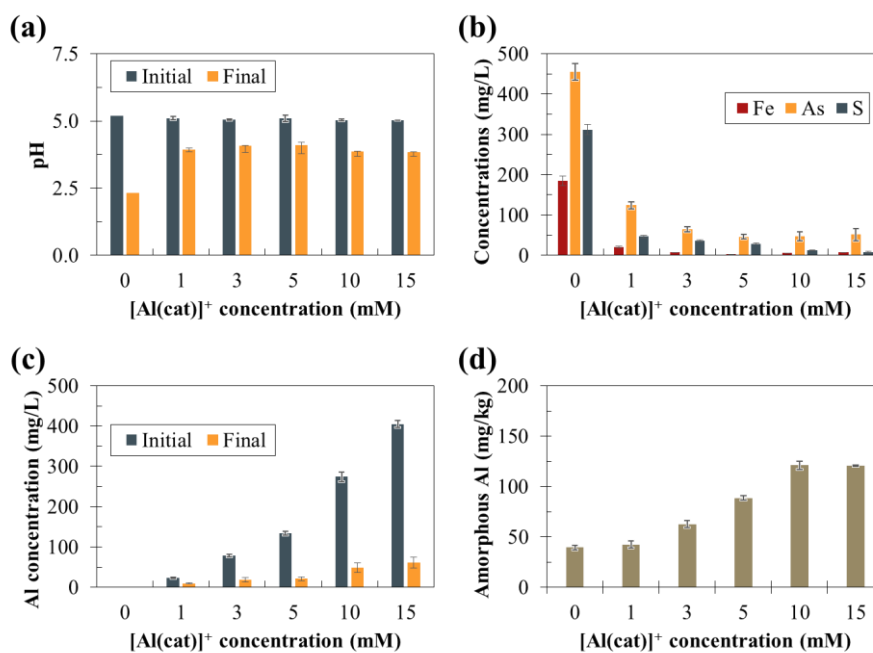


Figure 4-13. Effects of [Al(cat)]⁺ concentrations on the oxidation of arsenopyrite: (a) pH, (b) dissolved Fe, As, and S concentrations leached from arsenopyrite, (c) dissolved Al concentration before and after leaching of arsenopyrite, and (d) the amounts of extracted Al from the coating formed on arsenopyrite. Note: ratio of Al³⁺ to catechol = 1:1; [Cl⁻]_{tot} = 45 mM; leaching time = 7 days; pH = 5.

4.3.4 Anodic and cathodic half-cell reactions of arsenopyrite oxidation

Figure 4-14 shows the anodic and cathodic polarization curves of arsenopyrite electrode pretreated with DI water (control) and Al(III) mono-catechol complex (CME). Current density profile of arsenopyrite pretreated with [Al(cat)]⁺ measured during anodic polarization (Figure 4-14a) was substantially lower than that of control, which means that [Al(cat)]⁺ could suppress anodic half-cell reaction of arsenopyrite oxidation. This suppression could be explained by two possibilities: (1) the coating formed on arsenopyrite (1) blocked the contact of water and/or (2) inhibited the release of reaction products of arsenopyrite oxidation to outside. In the case of cathodic polarization (Figure 4-14b), CME-treated arsenopyrite also showed lower current density than the control, indicating that [Al(cat)]⁺ suppressed cathodic half-cell reaction of arsenopyrite oxidation. It is most likely achieved by preventing O₂ reduction on the cathodic site of arsenopyrite. The amount of electric charge transferred during polarization, measured by calculating the areas below current density curves ($Q [C] = I [A] \times t [s]$), is listed in Table 4-2. As it can be seen, the amounts of electric charge transferred through CME-treated arsenopyrite during both anodic and cathodic polarizations were lower than that of control, which are in good agreement with leaching results (Figure 13a).

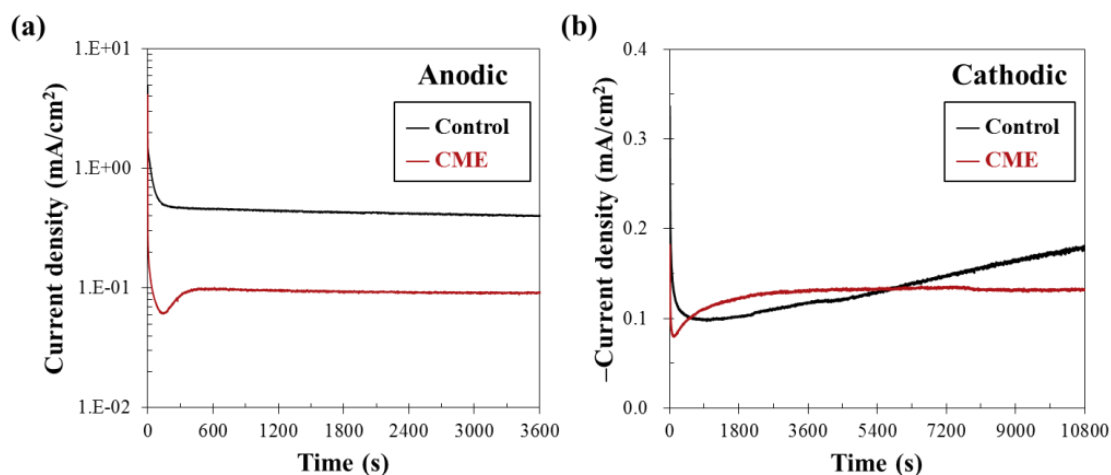


Figure 4-14. Chronoamperometric response of arsenopyrite pretreated with DI water (control) and Al-catecholates complex (CME): (a) anodic polarization of arsenopyrite at +0.7 V vs. SHE and (b) cathodic polarization of arsenopyrite at 0.0 V vs. SHE. Note that y-axes of Figure 4-14b is “-Current density.”

Table 4-2. Electric charges generated during anodic and cathodic polarizations of arsenopyrite pretreated in DI water (control) and Al-catecholates complex (CME).

Pretreatment	Electric charge, Q (C/cm ²)	
	Anodic	Cathodic
Control	19.3	9.68
CME	7.28	7.14

4.3.5 The proposed mechanism of Al-based CME

Based on the findings obtained in this chapter, a detailed mechanism of Al-based CME was proposed as illustrated in Figure 4-15. Al-catecholates complexes are adsorbed on arsenopyrite surfaces where it is sequentially decomposed and releases “free” Al³⁺ that is precipitated and forms Al-oxyhydroxide coating. In addition, this surface coating suppressed both anodic and cathodic half-cell reactions of arsenopyrite oxidation.

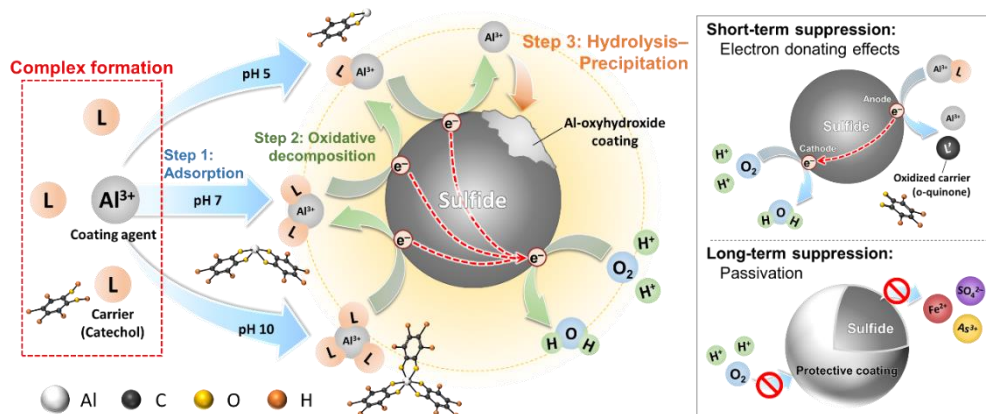


Figure 4-15. The schematic diagram of a proposed mechanism of Al-based CME.

4.3.6 Long-term stability of CME-treated arsenopyrite

Figures 4-16a–c illustrate the cumulative amounts of Fe, As, and S released from arsenopyrite during the weathering cell tests, and the results showed that the oxidation of CME-treated arsenopyrite was less extensive compared with that of the control. However, the cumulative concentrations of Fe, As, and S in Al-based CME increased gradually, which suggest that the Al-oxyhydroxide coatings formed by Al-based CME treatment did not completely cover the surface of arsenopyrite. Because of this, arsenopyrite oxidation is most likely progressed through the exposed surface, resulting in the acidification of leachate (Figure 4-16d). Based on thermodynamic considerations (Figure 4-3), the Al-oxyhydroxide coating formed during Al-based CME treatment was most likely boehmite ($\gamma\text{-AlO}(\text{OH})$), which could be dissolved under acidic conditions (i.e., below pH 4.5). At the beginning of the weathering cell tests, the leachate pH of Al-based CME treated sample was around pH 4.5 (Figure 4-16d), so the coating might have dissolved as pH decreased with time. This deduction is further supported by the non-existent signal of Al from the SEM-EDX analysis of the sample treated with Al-based CME after the weathering cell test (Figures 4-17c and d). Nevertheless, Al-based CME treatment still effectively suppressed arsenopyrite oxidation for up to 50 days (Figure. 4-16). The surface of arsenopyrite treated by Al-based CME was also less oxidized than the untreated sample. As shown in the SEM photomicrographs of the control (Figure 4-17a), secondary minerals, most likely Fe-oxyhydroxide and/or ferric arsenate, were substantially formed on the surface of arsenopyrite, and its EDX spectrum (Figure 4-17b) shows strong signal of O. This means that the stability of the coating formed by Al-based CME could be improved if it is co-disposed with minerals (e.g., limestone (CaCO_3), dolomite ($\text{CaMg}(\text{CO}_3)_2$), and apatite ($\text{Ca}_{10}(\text{PO}_4)_6(\text{OH})_2$)) and industrial by-products (e.g., cement kiln dust (CKD) and pulp/paper residue) that have appropriate neutralization potential to maintain the pH at around 5 to 8 where Al-oxyhydroxide is stable.

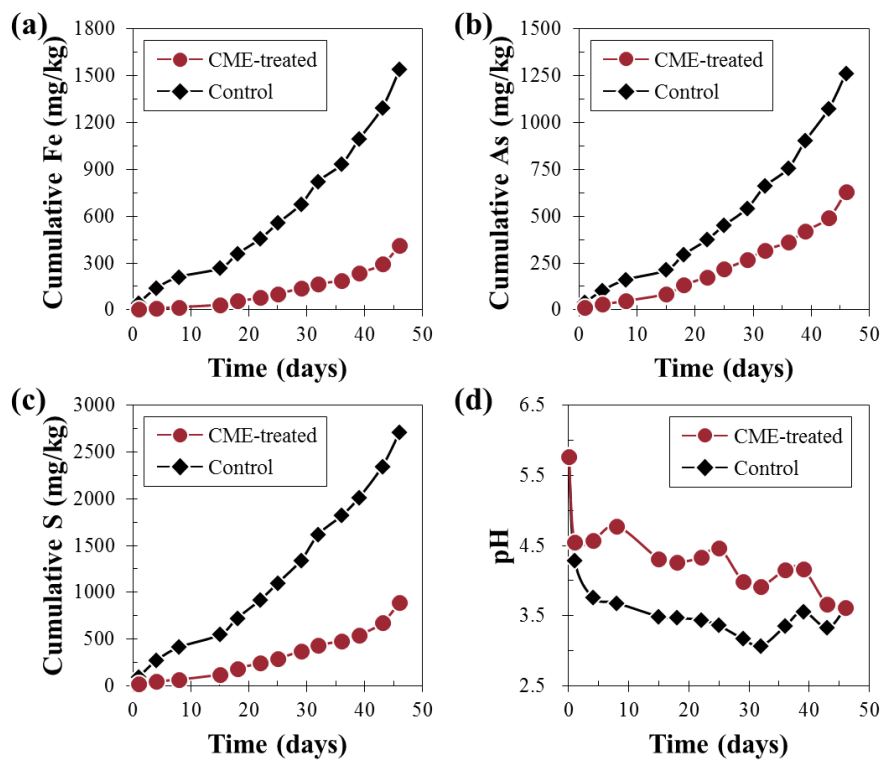


Figure 4-16. Weathering cell tests of control and CME-treated arsenopyrite: changes in the concentrations of (a) Fe, (b) As, and (c) S, and evolution of leachate (d) pH.

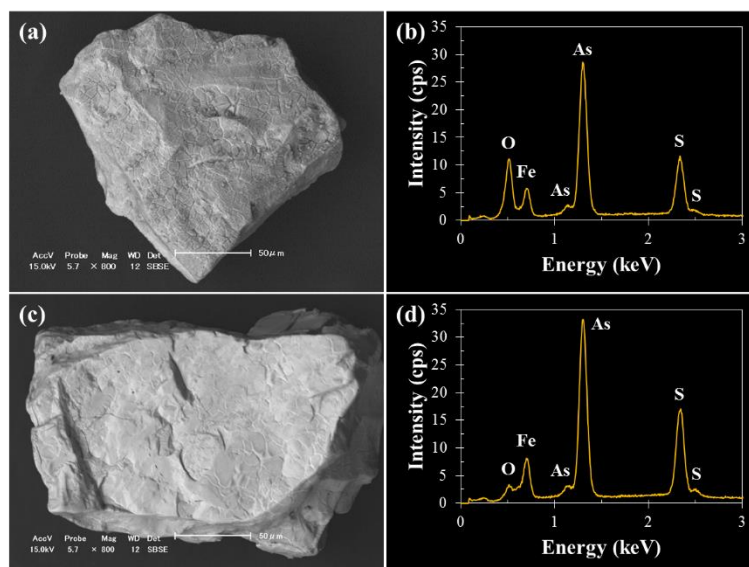


Figure 4-17. SEM-EDX results of residues after weathering cell tests: (a) SEM photomicrograph and (b) EDX spectrum of control, and (c) SEM photomicrograph and (d) EDX spectrum of CME-treated sample.

4.3.7 Regeneration of used organic carrier by electrolysis

After CME treatment, the wastewater that contains organic compounds is generated. If organic compounds can be regenerated and used for CME treatment again, which would make a process more cost-effective and sustainable. Before starting regeneration experiments, quinone-containing solution was prepared by exposing catechol solution to air and then LSV measurements were carried out to estimate the changes in catechol concentrations remained. As shown in Figure 4-18a, LSV of fresh catechol (i.e., without pre-oxidation referred to “0 day”) shows OCP at around 0.15 V while it increased to over 0.3 V after pre-oxidation. According to the Nernst equation (eq. (4-6)), the increase in OCP indicated that the amounts of oxidized products (i.e., quinone) increased.

$$E = E^0 + \frac{RT}{nF} \ln \frac{[Ox]}{[Red]} \quad (4-6)$$

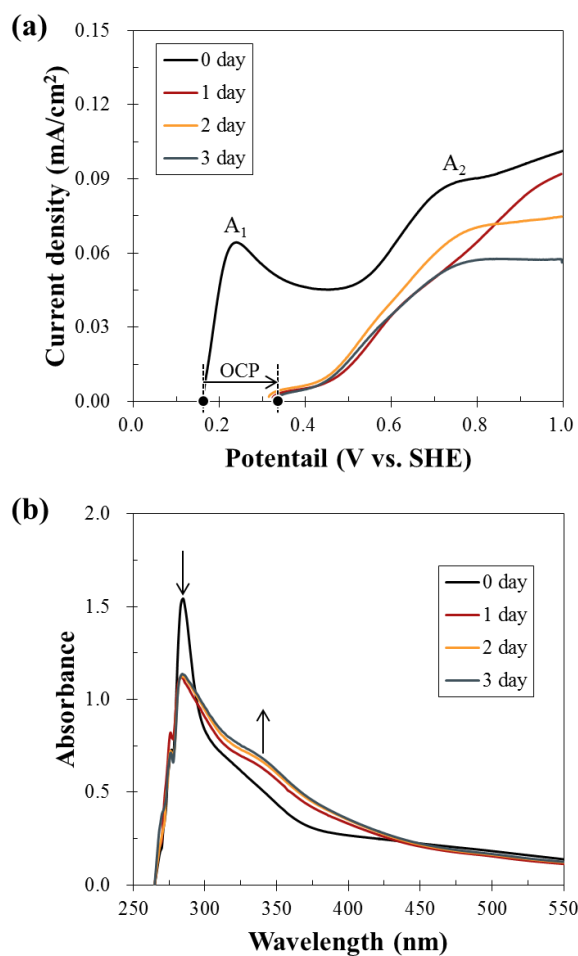


Figure 4-18. (a) Linear sweep voltammograms and (b) UV-vis spectra of catechol solutions with various air-exposure times.

In addition, LSV of fresh catechol shows two distinct anodic peaks (A_1 and A_2) but after pre-oxidation, peak A_1 disappeared and the peak current of A_2 decreased (Figure 4-18a), also indicating that the amounts of catechol and semi-quinone were reduced due most likely to the formation of quinone. It is interesting to note that UV-vis spectra also indicated that an absorption peak of catechol (285 nm) decreased whilst a broad peak centered at around 340 nm, attributed to the absorption of quinone (NIST, 2018), increased as pre-oxidation proceeded (Figure 4-18b).

The regeneration of quinone-containing solution, prepared using 1 mM catechol solution by air-exposure for 3 days, was examined using electrolysis wherein a fixed potential at 0.0 V vs. SHE was applied. At this potential, quinone could be favorably reduced back to catechol as described in section 2.3.2. After electrolysis of quinone-containing solution for 1 day, LSV shows that OCP slightly decreased and anodic current increased compared with that after pre-oxidation, both of which indicated the amounts of oxidized phase (i.e., catechol) increased (Figure 4-19). This result implies that after CME treatment, used organic carrier in wastewater could be regenerated and afterward it would be reused for the treatment.

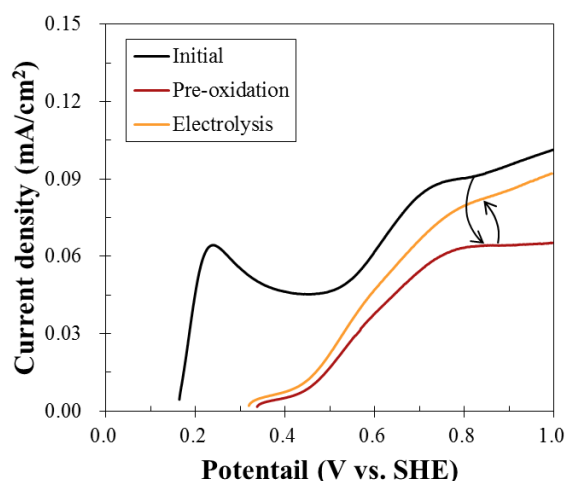


Figure 4-19. Linear sweep voltammograms of non-treated and pre-oxidized catechol solutions, and regenerated catechol solution using electrolysis.

4.4 Conclusions

The potential of Al-catecholate complexes as an alternative to Ti-catecholate complex for CME was investigated. Al^{3+} and catechol form three types of complexes depending on the pH: $[Al(cat)]^+$, $[Al(cat)_2]^-$ and $[Al(cat)_3]^{3-}$, which are dominant in the pH ranges of 4.4–5.3, 5.3–8.3 and 8.3–14.0, respectively. $[Al(cat)]^+$ was decomposed via a one-step oxidation reaction while $[Al(cat)_2]^-$ and

$[\text{Al}(\text{cat})_3]^{3-}$ were sequentially decomposed in two steps and three steps, respectively, all of which occurred irreversibly. Among the three complexes, $[\text{Al}(\text{cat})]^+$ was the most effective in suppressing arsenopyrite oxidation because it needed less step for complete decomposition. The suppressive effects of $[\text{Al}(\text{cat})]^+$ on arsenopyrite oxidation were relatively rapid compared with $[\text{Ti}(\text{cat})_3]^{2-}$, and at higher $[\text{Al}(\text{cat})]^+$ concentrations, better coating formations were observed. SEM-EDX, DRIFTS, and XPS analyses indicated that the coating formed on arsenopyrite was mainly composed of Al-oxyhydroxide. Moreover, this surface protective coating could suppress both anodic and cathodic half-cell reactions of arsenopyrite oxidation, indicating that it was passivated by Al-based CME treatment. Finally, the results of weathering cell tests of CME-treated arsenopyrite indicated that its oxidation could be successfully suppressed up to 50 days although the coating formed by CME dissolved with time. To improve the stability of Al-coating, it is recommended to co-dispose CME-treated arsenopyrite with basic materials that have appropriate neutralization potential to provide a suitable environment where Al-oxyhydroxide is stable. Moreover, used organic carrier produced after CME treatment could be regenerated by applying electrolysis (0.0 V vs. SHE) and it would be used again for the treatment.

This chapter is edited from “Park et al., 2018b. Simultaneous suppression of acid mine drainage formation and arsenic release by Carrier-microencapsulation using aluminum-catecholate complexes. *Chemosphere* 205, 414–425.”

References

- Ačai, P., Sorrenti, E., Gorner, T., Polakovič, M., Kongolo, M., de Donato, P., 2009. Pyrite passivation by humic acid investigated by inverse liquid chromatography. *Colloids Surf. A: Physicochem. Eng. Asp.* 337 (1–3), 39–46.
- Achimovičová, M., Baláž, P., 2005. Influence of mechanical activation on selectivity of acid leaching of arsenopyrite. *Hydrometallurgy* 77 (1–2), 3–7.
- Bai, S., Tsuji, Y., Okaue, Y., Yokoyama, T., 2011. Complexation of silicic acid with tiron in aqueous solution under near natural condition. *J. Solution Chem.* 40 (2), 348–356.
- Belzile, N., Maki, S., Chen, Y.W., Goldsack, D., 1997. Inhibition of pyrite oxidation by surface treatment. *Sci. Total Environ.* 196 (2), 177–186.
- Bethke, C.M., 1992. *The Geochemist's Workbench – A User's Guide to Rxn, Act2, Tact, React and Gtplot*, University of Illinois, Urbana Illinois.
- Bonnissel-Gissing, P., Alnot, M., Ehrhardt, J.J., Behra, P., 1998. Surface oxidation of pyrite as a

- function of pH. *Environ. Sci. Technol.* 32 (19), 2839–2845.
- Bouzahzah, H., Benzaazoua, M., Bussiere, B., Plante, B., 2014. Prediction of acid mine drainage: Importance of mineralogy and the test protocols for static and kinetic tests. *Mine Water Environ.* 33, 54–65.
- Carlson, L., Bigham, J.M., Schwertmann, U., Kyek, A., Wagner, F., 2002. Scavenging of As from acid mine drainage by schwertmannite and ferrihydrite: a comparison with synthetic analogues. *Environ. Sci. Technol.* 36 (8), 1712–1719.
- Cornard, J.-P., Lapouge, C., Allet-Bodelot, C., 2010. Study of S₀ and S₁ states of catechol and catechol–Al(III) systems in aqueous solution by TD-DFT methods and electronic spectroscopies. *Chem. Phys. Lett.* 489 (4–6), 164–168.
- Danilewicz, J.C., 2012. Review of Oxidative Processes in Wine and Value of Reduction Potentials in Enology. *Am. J. Enol. Vitic.* 63 (1), 1–10.
- de Noronha, A.L.O., Guimarães, L., Duarte, H.A., 2007. Structural and thermodynamic analysis of the first mononuclear aqueous aluminum citrate complex using DFT calculations. *J. Chem. Theory Comput.* 3 (3), 930–937.
- Downard, A.J., O’Sullivan, B., Powell, K.J., 1996. A voltammetric study of the aluminum complexes of catechol and 1,2-dihydroxyanthraquinone-3-sulfonic acid. *Polyhedron* 15 (20), 3469–3479.
- Evangelou, V.P., 1995. *Pyrite Oxidation and Its control*. CRC Press, Boca Raton, FL.
- Gustafsson, J.P., 2010. Visual MINTEQ Thermodynamic Database in GWB Format. <http://vminteq.lwr.kth.se> (Accessed 08 April 2017).
- Jia, Y., Zhang, D., Pan, R., Xu, L., Demopoulos, G.P., 2012. A novel two-step coprecipitation process using Fe(III) and Al(III) for the removal and immobilization of arsenate from acidic aqueous solution. *Water Res.* 46 (2), 500–508.
- Kalyanaraman, B., Felix, C.C., Sealy, R.C., 1985. Semiquinone anion radicals of catechol(amine)s, catechol estrogens, and their metal ion complexes. *Environ. Health Perspect.* 64, 185–198.
- Kloprogge, J.T., Duong, L.V., Wood, B.J., Frost, R., 2006. XPS study of the major minerals in bauxite: Gibbsite, bayerite and (pseudo-)boehmite, *J. Colloid Interface Sci.* 296 (2), 572–576.
- Lalvani, S.B., Deneve, B.A., 1990. Passivation of pyrite due to surface treatment. *Fuel* 69 (12), 1567–1569.
- Lippincott, E.R., Valkenburg, A.V., Weir, C.E., Bunting, E.N., 1958. Infrared studies on polymorphs

- of silicon dioxide and germanium dioxide. *J. Res. Natl. Bur. Stand.* 61 (1), 61–70.
- McBride, M.B., Wesselink, L.G., 1988. Chemisorption of catechol on gibbsite, boehmite, and noncrystalline alumina surfaces. *Environ. Sci. Technol.* 22, 703–708.
- McKeague, J.A., Day, J.H., 1965. Dithionite- and oxalate-extractable Fe and Al as aids in differentiating various classes of soils. *Can. J. Soil Sci.* 46 (1), 13–22.
- McKibben, M.A., Tallant, B.A., del Angel, J.K., 2008. Kinetics of inorganic arsenopyrite oxidation in acidic aqueous solutions. *Appl. Geochem.* 23 (2), 121–135.
- Monte, M.B.M., Butra, A.J.B., Albuquerque, C.R.F., Tondo, L.A., Lins, F.F., 2002. The influence of the oxidation state of pyrite and arsenopyrite on the flotation of an auriferous sulphide ore. *Miner. Eng.* 15 (12), 1113–1120.
- Musić, S., Dragčević, Đ., Popović, S., 1999. Hydrothermal crystallization of boehmite from freshly pre-cipitated aluminium hydroxide. *Mater. Lett.* 40 (6), 269–274.
- National Institute of Standards and Technology (NIST), 2018. NIST Chemistry WebBook, SRD 69. <https://webbook.nist.gov/cgi/cbook.cgi?ID=C583631&Mask=400> (Accessed 03 November 2018).
- Nesbitt, H.W., Muir, I.J., Pratt, A.R. 1995. Oxidation of arsenopyrite by air and air-saturated, distilled water, and implications for mechanism of oxidation, *Geochim. Cosmochim. Acta* 59 (9), 1773–1786.
- Nurchi, V.M., Pivetta, T., Lachowicz, J.I., Crisponi, G., 2009. Effect of substituents on complex stability aimed at designing new iron(III) and aluminum(III) chelators. *J. Inorg. Biochem.* 103 (2), 227–236.
- Öhman, L.-O., Nordin, A., Sedeh, I.F., Sjöberg, S., 1991. Equilibrium and structural studies of silicon(IV) and aluminum(III) in aqueous solution. 28. Formation of soluble silicic acid-ligand complexes as studied by potentiometric and solubility measurements. *Acta Chem. Scand.* 45, 335–341.
- Park, I., Tabelin, C.B., Magaribuchi, K., Seno, K., Ito, M., Hiroyoshi, N., 2018a. Suppression of the release of arsenic from arsenopyrite by carrier-microencapsulation using Ti-catechol complex. *J. Hazard. Mater.* 344, 322–332.
- Park, I., Tabelin, C.B., Seno, K., Jeon, S., Ito, M., Hiroyoshi, N., 2018b. Simultaneous suppression of acid mine drainage formation and arsenic release by Carrier-microencapsulation using aluminum-catecholate complexes. *Chemosphere* 205, 414–425.

- Pozo, G., Pongy, S., Keller, J., Ledezma, P., Freguia, S., 2017. A novel bioelectrochemical system for chemical-free permanent treatment of acid mine drainage. *Water Res.* 126, 411–420.
- Pracht, J., Boenigk, J., Isenbeck-Schröter, M., Keppler, F., Schöler, H.F., 2001. Abiotic Fe(III) induced mineralization of phenolic substances. *Chemosphere* 44 (4), 613–619.
- Raade, G., Mladeck, M.H., Kristiansen, R., Din, V.K., 1984. Kaatialaite, a new ferric arsenate mineral from Finland. *Am. Mineral.* 69, 383–387.
- Ram, S., 2001. Infrared spectral study of molecular vibrations in amorphous, nanocrystalline and $\text{AlO}(\text{OH}) \cdot n\text{H}_2\text{O}$ bulk crystals. *Infrared Phys. Technol.* 42 (6), 547–560.
- Saiz-Poseu, J., Sedó, J., García, B., Benaiges, C., Parella, T., Alibés, R., Hernando, J., Busqué, F., Ruiz-Molina, D., 2013. Versatile nanostructured materials via direct reaction of functionalized catechols. *Adv. Mater.* 25 (14), 2066–2070.
- Sikora, F.J., McBride, M.B., 1989. Aluminum complexation by catechol as determined by ultraviolet spectrophotometry. *Environ. Sci. Technol.* 23, 349–356.
- Tabelin, C.B., Veerawattananun, S., Ito, M., Hiroyoshi, N., Igarashi, T., 2017. Pyrite oxidation in the presence of hematite and alumina: I. Batch leaching experiments and kinetic modeling calculations. *Sci. Total Environ.* 580, 687–698.
- Violante, A., Pigna, M., Gaudio, S.D., Cozzolino, V., Banerjee, D., 2009. Coprecipitation of arsenate with metal oxides. 3. Nature, mineralogy, and reactivity of iron(III)-aluminum precipitates. *Environ. Sci. Technol.* 43 (5), 1515–1521.
- Wei, X., Viadero, R.C., Buzby, K.M., 2005. Recovery of Iron and Aluminum from Acid Mine Drainage by Selective Precipitation. *Environ. Eng. Sci.* 22 (6), 745–755.
- Williamson, M.A., Rimstidt, J.D., 1994. The kinetics and electrochemical rate-determining step of aqueous pyrite oxidation. *Geochim. Cosmochim. Acta* 58 (24), 5443–5454.
- Xu, Z., 2013. Mechanics of metal-catecholate complexes: The roles of coordination state and metal types. *Sci. Rep.* 3, 2914.
- Yang, J., Stuart, M.A.C., Kamperman, M., 2014. Jack of all trades: versatile catechol crosslinking mechanisms. *Chem. Soc. Rev.* 43, 8271–8298.

CHAPTER 5 – GENERAL CONCLUSION

This dissertation is comprised of five chapters which detail the different methodologies used in the experiments and their outcomes. Chapter 1 describes the statement of the problem, objectives of this study, background and a literature review of the formation of AMD and its control. The oxidations of sulfide minerals result in the formation of acid mine drainage (AMD), one of the most serious environmental problems associated with the mining industries because of its extremely low pH (less than pH 3) and elevated concentrations of toxic heavy metals (e.g., Cu, Fe, Pb, and Zn). Of all the sulfide minerals, the oxidation of arsenopyrite (FeAsS) is of importance because it causes not only the formation of AMD but also the release of toxic arsenic (As) into the environment. Arsenic is a highly toxic and strictly regulated element known to increase the risks of developing numerous disease like hyperpigmentation, keratosis, anemia, neuropathy, and several types of cancers even at minute amounts. Neutralization is the most commonly used technique to mitigate the negative environmental impacts of As-containing AMD on ecological systems and human health. Although effective, this technique is very costly and unsustainable because of the continuous treatment and supply of chemicals and energy, expensive maintenance and labor cost, and long-term monitoring of affected ecosystems until AMD generation stops. To overcome the limitations of conventional remediation techniques, carrier-microencapsulation (CME) has been proposed as a new technique to suppress AMD formation by forming a protective coating on sulfide minerals using metal-catecholate complexes. However, the mechanisms involved in this process remain unclear due to the lack of understanding of how the metal-organic complex is oxidatively decomposed. Moreover, the applicability of CME for arsenopyrite has not yet been studied. Thus, the objectives of this study are four-fold: (1) to elucidate in detail the mechanisms involved in CME, (2) to apply CME for treating arsenopyrite, (3) to improve the practicality of CME, and (4) to develop a sustainable process to prevent As release and AMD formation based on CME.

In Chapter 2, the effects of CME using Ti-catecholate complex (Ti-based CME) on arsenopyrite oxidation were investigated by leaching and electrochemical experiments. The results of leaching experiments showed that the release of As from arsenopyrite was substantially suppressed by Ti-based CME, and SEM-EDX and DRIFT analyses of CME-treated residue indicated that arsenopyrite was covered with a Ti-oxyhydroxide coating. The results of cyclic voltammetry and SEM-EDX analysis of a platinum electrode in Ti-catecholate complex solution showed that $[\text{Ti}(\text{cat})_3]^{2-}$ was oxidized to form an intermediate phase at 680 mV vs. SHE via partial oxidation of either one or two of the catechol molecules with distorted Ti–O bonds. This was then followed by the chemical decomposition of the intermediate finally releasing Ti^{4+} that is precipitated as Ti-oxyhydroxide coating. Chronoamperometric measurements using an arsenopyrite electrode

treated with Ti-catecholate complex confirmed that the coating formed by Ti-catecholate complex suppressed both anodic and cathodic half-cell reactions of arsenopyrite oxidation.

In Chapter 3, the kinetic aspects of Ti-based CME for suppressing arsenopyrite oxidation were investigated. Ti-based CME could successfully suppress arsenopyrite oxidation by forming a surface protective coating, but it required at least 14 days of treatment to generate a coating thick enough to be effective under ambient conditions. To improve the kinetics of Ti-based CME, elevated temperature and the addition of chemical promoters like Cu^{2+} or $\text{Cu}^{2+}\text{-NH}_3$ complex were examined. As temperature increased, the decomposition rate of Ti-catecholate complex became faster, resulting in the suppression of arsenopyrite oxidation achieved early. The results of Ti-catecholate complex decomposition fitted well with a pseudo-first-order kinetic model. The rate constants of complex decompositions at 30, 50, and 70 °C were estimated at around 0.009, 0.021, and 0.051 h^{-1} , respectively, and its activation energy was calculated to be 37.4 kJ/mol. As another option to accelerate the decomposition of Ti-catecholate complex under ambient conditions, the effects of Cu^{2+} addition on Ti-based CME treatment for arsenopyrite were investigated. The addition of Cu^{2+} transformed the anode property of arsenopyrite by forming CuS-like compounds, thereby accelerating the decomposition of Ti-catechol complex.

In Chapter 4, Al^{3+} -catechol complex was evaluated as a candidate of the metal-organic complex used for CME to suppress arsenopyrite oxidation. Al(III) ion and catechol formed three complex species depending on the pH: (1) $[\text{Al}(\text{cat})]^+$ between 4.7 and 5.5, (2) $[\text{Al}(\text{cat})_2]^-$ between 5.5 and 8.5, and (3) $[\text{Al}(\text{cat})_3]^{3-}$ between 8.5 and 14.0. Electrochemical study confirmed that the decomposition of Al-catecholate complexes occurs sequentially: $[\text{Al}(\text{cat})_3]^{3-} \rightarrow [\text{Al}(\text{cat})_2]^- \rightarrow [\text{Al}(\text{cat})]^+ \rightarrow \text{Al}^{3+}$. Leaching experiments and surface characterizations of the residue by SEM-EDX, DRIFT, and XPS showed that in the presence of Al-catecholate complexes, arsenopyrite was covered with an Al-oxyhydroxide coating and As release from arsenopyrite was suppressed. The decomposition rate of Al-catecholate complex was faster than that of Ti-catecholate complex, and the suppression of As release from arsenopyrite was substantial with Al-based CME. The electrical charge of Al^{3+} is smaller than that of Ti^{4+} , and thus this may cause the weaker bond and faster decomposition rate with Al-catecholate complex than Ti-catecholate complex. Among the three Al-catecholate complexes, $[\text{Al}(\text{cat})]^+$ suppressed As release most effectively because it had the fastest complex decomposition/coating formation rate. Chronoamperometric measurements of arsenopyrite electrode treated with $[\text{Al}(\text{cat})]^+$ indicated that both anodic and cathodic half-cell reactions of arsenopyrite oxidation were suppressed by the surface protective coating formed on it. Long-term stability of CME-treated arsenopyrite was evaluated using weathering cell tests for ca. two months and the results showed that arsenopyrite oxidation was successfully suppressed by treating it with Al-based CME. Finally, the regeneration of used organic carrier (i.e., quinone) to catechol was confirmed to

be possible by electrolysis at an applied potential of 0.0 V vs. SHE. Taking all of these results into consideration, we proposed a more sustainable process based on CME that would prevent As-containing AMD formation from mine wastes as illustrated in Figure 5-1.

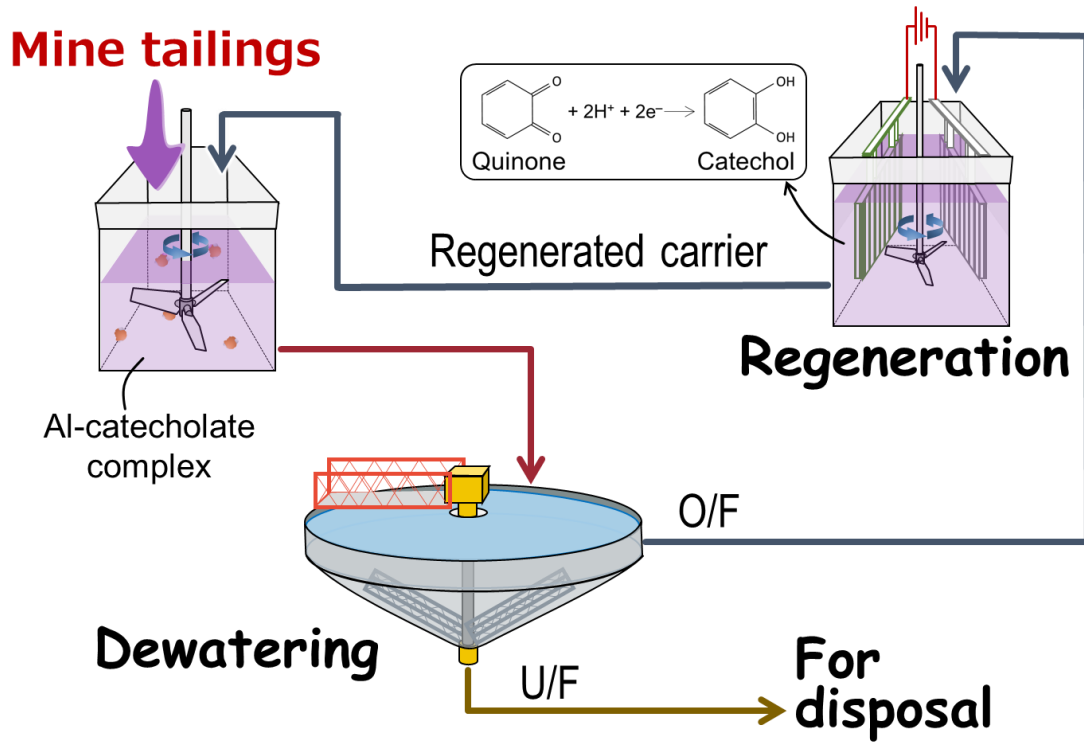


Figure 5-1. The proposed process based on CME for treating mine wastes.

ACKNOWLEDGEMENT

This dissertation could be successfully completed thanks to many people, so I wish to express my sincere appreciation to each of them.

I would like to acknowledge to my supervisor, Professor Naoki Hiroyoshi, who gave me a lot of constructive advice to succeed in my research. He also guided me to walk through the path of a researcher. I will never forget your enthusiasm to do your best to inspire not only me but also all the students.

I am very grateful to Associate Professor Mayumi Ito, who encouraged me in the completion of this dissertation. Your valuable advice and critical comments for the improvements of my research are gratefully appreciated.

My sincere thanks are extended to my co-supervisor, Assistant Professor Carlito Baltazar Tabelin. He always strived to inspire me when I was in trouble with research works, rather than giving me a direct answer. His continual encouragement made my dissertation successful. I am looking forward to meeting you somewhere in the world and hope everything goes well with you at the University of New South Wales, Australia.

Special appreciation goes to Professor Tsutomu Sato (Division of Sustainable Resources Engineering, Faculty of Engineering, Hokkaido University) and Associate Professor Masatoshi Sakairi (Division of Materials Science and Engineering, Faculty of Hokkaido University), who served as co-examiners of my dissertation. Thanks to their efforts and advice, this dissertation could have improved considerably.

I am particularly grateful for the assistance given by my former supervisor, Professor Kyoungkeun Yoo from Korea Maritime and Ocean University, who guided me to grow up as a researcher during my bachelor's and master's courses. If I had not met him, I would not be here now. Even after graduating from his laboratory, he has always encouraged me and gave me valuable advice. I am forever in your debt.

To my colleagues from the Laboratory of Mineral Processing and Resources Recycling, thank you very much for being warm during my Ph.D. course. Before I came to Japan, I was a bit nervous because it's my first time that I have ever lived away from home. Thanks to your kind support and companionship, I think I was able to complete a 3-year journey. Special thanks are extended to my junior students, Kagehiro Magaribuchi, Kensuke Seno, and Kazuki Higuchi. I would like to say thank you for putting your trust in me and for always helping me in academic and university matters.

Finally, I would like to thank heartily my family for their continual support and encouragement.